*Università degli Studi di Firenze*
*Scuola di Ingegneria*
*DIEF* - Department of Industrial Engineering of Florence

PhD School: *Energetica e Tecnologie Industriali ed Ambientali Innovative*
Scientific Area: ING-IND/08 - *Macchine a Fluido*

# Analysis of gas turbine leading edge cooling systems in static and rotating conditions

**PhD Candidate**: Ing. Lorenzo Cocchi

**Tutor**: Prof. Ing. Bruno Facchini

**CoTutor**: Ing. Alessio Picchi

**PhD School Coordinator**: Prof. Ing. Maurizio De Lucia

XXXI PhD School Cycle - 2015-2018

*To my father,*
*because I hope you're proud of me,*
*wherever you are.*

*To my mother,*
*because you always trusted me,*
*your love only allowed me to reach this goal.*

*To my sweetheart,*
*because you've always been beside me,*
*every day you make me a better man.*

# Acknowledgements

*Having reached the end of this travel, I have the occasion to express my gratitude to all of the people whose support made me able to reach this goal.*

*First of all, the most sincere and heartfelt thanks go to Prof. Bruno Facchini, non only for having given me the opportunity to grow all along this study experience, but also for the support and the precious suggestions during the activity, as well as for having trusted me even in the hardest moments.*

*I also have to acknowledge Ing. Alessio Picchi, for his invaluable advices and continuous help during the whole work: your practical sense actually routed the work in the right direction, and I really can't remember how many times your experience helped me to solve even the most hopeless issues. Thank you so much!*

*I feel to extend my gratitude to all the members of HTC group, which after these years spent together I feel much more like friends than like colleagues. In particular, I want to thank Prof. Carlo Carcasci, for his help and suggestions, as well as for all the funny moments spent together. I also owe much to Ing. Antonio Andreini, a real reference for many of the activities I carried out in these years. A special thanks goes to Lorenzo Mazzei, for his precious support during the numerical part of the activity and for his experience, as well as for his sympathy and cutting irony: I can't stop smiling thinking at many of your jokes! I also feel particularly in debt with Simone Paccati: a relevant part of this thesis would not have been possible without your advices and your work. Thank you so much!*

*I also want to thank all the other colleagues which made every day of these years pleasant both inside and outside the University: the students of my PhD cycle Daniele (for our hiking adventures both near and far from home) and Davide, the lab guys Giulio, Daniele, Asif, Riccardo, Tommaso B., Tommaso L. and Valter, the other past and present colleagues Lorenzo W., Sabrina, Tommaso F., Alessandro, Emanuele, Andrea, Dominique, Matteo N. (a master in mushroom hunting!), Lorenzo P. and the newcomers Matteo P. (the real computer guru), Carlo (best* laureando *ever!), Leonardo, Tommaso D. and Piercarlo. These few lines are not sufficient to express not even a part of my gratitude to all of you!*
*Finally, I want to express my deepest gratitude to the most beautiful gifts any man could desire: my lovely mother and my wonderful girlfirend. You supported me along all of these years, giving me the strength to endure any difficulty and comforting me during the most difficult times. I really owe you everything, and without you I would never have reached this goal. Thank you with all of my heart!*

# Abstract

A driving trend in gas turbine development is the increase of turbine inlet temperature, aimed at improving the engine performance, which is however limited by the resistance of the most thermally solicited components. As a consequence, more and more effective cooling systems are required in order to allow further engine development. A particularly critical region from this point of view is the blades leading edge, given the presence of the hot gases stagnation point. Moreover, inherent forces of rotation may strongly alter the flow field and thus the heat transfer pattern. This requires the adoption of highly complex cooling schemes for this region, based on the combination of different techniques, which make their analysis particularly challenging and also require the full system to be replicated in order to reliably determine the cooling performance.
This work is focused on the study of a "cold bridge" cooling system, applied to the leading edge of a gas turbine blade. The aim of the research is to obtain a full comprehension of the phenomena and interactions occurring in this kind of devices, including the effect of rotation and of different impingement arrangements. The investigated geometry replicates a radial section of the leading edge, and includes a radial supply channel, providing coolant air to a series of impingement holes. Such holes generate impingement jets which cool down the inner side of the leading edge. A series of film cooling and showerhead holes extract the spent coolant flow from the leading edge cavity. A part of the coolant flow leaves the supply channel at its outer radial extremity, allowing to set an upstream crossflow for the jets.

Three different impingement geometries were analysed in this work: the first one presents seven square-edged, round holes aligned in the radial direction, the second one is identical to the first but has staggered holes along two parallel radial directions, while the third one has twice the number of holes, with a lower diameter but still with a staggered arrangement. The three geometries present the same overall passage area, thus allowing to highlight the effects of different coolant distributions for a given average velocity and coolant consumption. Four equally spaced Reynolds number values were investigated, and each test was performed both in static and rotating conditions. Different supply conditions were also investigated, replicating hub, midspan and tip radial sections of the blade by varying the crossflow mass flow rate. Finally, the effect of coolant extraction was also stressed by evaluating different mass flow splits across the extraction rows.

Tests were carried out on a dedicated test rig exploiting the transient heat transfer technique with thermochromic liquid crystals. A novel implementation of such method was developed, in order to apply it to rotating conditions and to replicate the correct sign of buoyancy forces. The test article is uniformly heated up before the test using a small amount of mass flow rate, and when its temperature is uniform and steady the whole nominal mass flow rate at ambient temperature is flown, thus obtaining a cold temperature step.

In order to allow a complete interpretation of thermal and fluid phenomena, the experimental campaign was supported by a numerical analysis, which was carried out using a scale resolving SAS approach due to the relevant flow unsteadiness.

The obtained results show that heat transfer pattern is strongly influenced both by the target surface curvature and by the extraction holes layout and flow distribution, with the latter being able to attract and deflect the turbulent shear layer structures but not the jet core. Supply conditions have an impact on jet lateral spreading, altering jet-wall interaction especially for the staggered geometries. Rotation acts both on the supply channel and on the jets, and its main outcome is to counterbalance the

crossflow effect and thus to reduce jet lateral spreading, with a slight heat transfer reduction. Finally, the direct comparison of the three geometries reveals that the cooling performance is maximized by employing a larger number of smaller impingement holes with a staggered arrangement.

# Contents

# Nomenclature

**Acronyms**

| | |
|---|---|
| $DES$ | Detached Eddy Simulation |
| $DNS$ | Direct Numerical Simulation |
| $DR$ | Density Ratio |
| $FC$ | Film Cooling |
| $HTC$ | Heat Transfer Coefficient |
| $IR$ | Infrared |
| $LE$ | Leading Edge |
| $LES$ | Large Eddy Simulation |
| $PS$ | Pressure Side |
| $PMMA$ | Polymethyl Methacrylate |
| $PTFE$ | Polytetrafluoroethylene |
| $RANS$ | Reynolds Averaged Navier Stokes |
| $SAS$ | Scale Adaptive Simulation |
| $SH$ | Showerhead |
| $SRS$ | Scale Resolving Simulation |
| $SS$ | Suction Side |
| $TLC$ | Thermochromic Liquid Crystals |
| $TSP$ | Temperature Sensitive Paints |
| $URANS$ | Unsteady RANS |

**Greeks**

| | | |
|---|---|---|
| $\beta$ | Pressure ratio | $[-]$ |

| | | |
|---|---|---|
| $\gamma$ | Specific heat capacity ratio | $[-]$ |
| $\Theta$ | Space dependent dimensionless temperature ratio | $[-]$ |
| $\theta$ | Time dependent dimensionless temperature ratio | $[-]$ |
| $\kappa$ | Wavenumber | $[1/m]$ |
| $\lambda$ | Thermal conductivity | $[W/mK]$ |
| $\mu$ | Dynamic viscosity | $[kg/ms]$ |
| $\nu$ | Kinematic viscosity | $[m^2/s]$ |
| $\rho$ | Density | $[kg/m^3]$ |
| $\omega$ | Rotational speed | $[rad/s]$ |

**Letters**

| | | |
|---|---|---|
| $A$ | Area | $[m^2]$ |
| $a$ | Thermal diffusivity | $[m^2/s]$ |
| $Bo$ | Buoyancy parameter | $[-]$ |
| $b$ | Equivalent 2D slot width | $[m]$ |
| $Cd$ | Discharge coefficient | $[-]$ |
| $Cr$ | Crossflow ratio | $[-]$ |
| $c$ | Specific heat capacity | $[J/kgK]$ |
| $D$ | Diameter | $[m]$ |
| $E$ | Turbulent kinetic energy amplitude | $[m^2/s^2]$ |
| $H$ | Jet-to-target plate spacing | $[m]$ |
| $h$ | Convective heat transfer coefficient | $[W/m^2K]$ |
| $k$ | Turbulent kinetic energy | $[m^2/s^2]$ |
| $L$ | Hole length | $[m]$ |
| $M$ | Ratio of modelled and resolved $k$ | $[-]$ |
| $\dot{m}$ | Mass flow rate | $[kg]$ |
| $N$ | Number | $[-]$ |
| $Nu$ | Nusselt number | $[-]$ |
| $n$ | Normal coordinate | $[m]$ |
| $P$ | Pitch | $[m]$ |
| $p$ | Pressure | $[Pa]$ |

| | | |
|---|---|---|
| $\dot{q}$ | Specific heat flux | $[W/m^2]$ |
| $R$ | Specific gas constant | $[J/kgK]$ |
| $Re$ | Reynolds number | $[-]$ |
| $Ro$ | Rotation number | $[-]$ |
| $r$ | Radius | $[m]$ |
| $S$ | Tangential spacing (target surface) | $[m]$ |
| $s$ | Tangential spacing (impingement plate) | $[m]$ |
| $T$ | Temperature | $[K]$ |
| $U$ | Velocity | $[m/s]$ |
| $V$ | Volume | $[m^3]$ |
| $W$ | Pumping power | $[W]$ |
| $Z$ | Radial extension | $[m]$ |

**Subscripts**

| | |
|---|---|
| $Cr$ | Crossflow |
| $conv$ | Convective |
| $corr$ | Corrected |
| $down$ | Downstream |
| $ext$ | Extraction |
| $f$ | fluid |
| $feed$ | Blade inlet section |
| $h$ | Hydraulic |
| $IMP$ | Impingement |
| $i$ | Initial |
| $in$ | Inlet |
| $j$ | Jet |
| $max$ | Maximum |
| $n$ | Normal |
| $o$ | Orifice |
| $ref$ | Reference |
| $s$ | Solid |
| $up$ | Upstream |
| $w$ | Wall |

| | |
|---|---|
| $z$ | Radial direction |

# Chapter 1

# Problem overview

The present work fits within the context of gas turbine cooling, which is one of the main design branches involved by past, contemporary and future development of such engines. In this chapter the context of this research will be presented, as well as a focus on its main objectives and scopes in relation to the current available knowledge.

## 1.1 Background of present research

At the present day, gas turbine engines are one of the most widely employed devices both for power generation and propulsion. The success of this solution is mainly due to the combination of different favourable features, namely the large power-to-weight ratio, the high reliability and lifespan and the short start up time. These characteristics lead the gas turbine to be an almost universal solution for aircraft propulsion and to an increasingly extensive use for electricity production. Driven by both these environments, the global gas turbine market size is expected to register an average annual growth rate of 4.8% in the period 2018-2025 [1]. The reasons of such expansion are different and related to the particular application field. If power generation is considered, high growth prospects for gas turbine engines are driven by the combination of the increasing global energy demand and the growing environmental

consciousness, which pushes towards a reduction of pollutant emissions and greenhouse gases. In particular, the growth in power generation from renewable energy sources, which provide a non programmable output even in a very limited time frame, requires a higher operational flexibility for the other power plants. This requirement can be adequately satisfied by gas turbine engines, which can be started within minutes and ramped up and down quickly [2]. Moreover, in comparison with other combustion-based power generation applications (e.g. coal-fired plants), gas turbines exhibit lower carbon emissions thanks to both the employed fuel (natural gas in most of the cases) and higher efficiency (if employed in combined cycle configurations). Both these facts are expected to increase the employment of gas turbines over the next several years [1]. On the other hand, as regards the propulsion employment in aviation, ICAO estimates that global passenger traffic will grow at 4.6% annually to 2032, and that freight traffic will grow at 4.4% annually over the same period [3]. Nowadays, aviation produces around 2% of the overall human carbon emissions [4], but the expansion of this sector will dramatically increase this percentage if no countermeasurements are taken [5]: as a consequence, the demand for more energy efficient and sustainable aero engines is increasingly growing. The expanding gas turbine employment pushes the development of this kind of engine: increasing the performance of such devices is positive both from an economic and an environmental point of view. In this case the engine performance, both in terms of efficiency and specific power output, is directly bound to the overall pressure ratio of the thermodynamic cycle and thus to the temperature of the gases entering the turbine. The ideal relation between specific power output and the turbine inlet temperature (TIT) is shown in the chart of Figure 1.1 as a solid line, which represents the output of an ideal machine with 100% turbine efficiency and no leakage or cooling flows. The same chart also reports the corresponding values for some notables machines which show that, starting from the very first aero engines developed by Whittle and Von Ohain [6], the trend in gas turbine development leads towards ever increasing values of TIT in order to obtain higher efficiencies end power outputs.

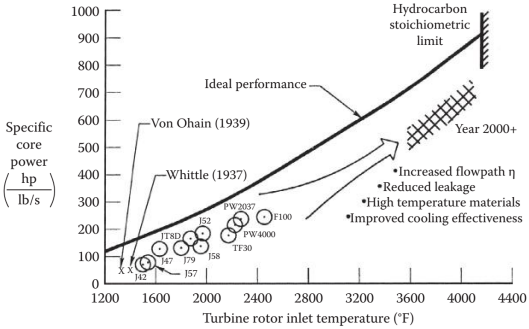


*Figure 1.1: Improvement of specific power output with TIT [7].*

As flow temperature grows, however, an increasingly severe environment is created for the engine components: the resulting thermal stresses add to the existing mechanical and chemical ones, and may lead to lifespan reduction and eventually to component failure. In order to address this issue, a main research topic focused on the development high temperature resistant materials (namely nickel and cobalt-based superalloys), ceramic coatings and innovative casting techniques, such as single-crystal solidification. Even so, present day temperature level have only been achieved thanks to the parallel development of cooling techniques for the most thermally stressed components, which made it possible to operate such devices at temperatures largely exceeding the material melting point, as shown by Figure 1.2
Given the importance of gas turbine cooling systems in the framework of the present research, a more detailed discussion on such topic, and on the blade cooling systems in particular, will be presented in Section 1.2.

## 1.2 Gas turbine cooling systems

The most thermally stressed components of a gas turbine engine include vanes and blades of the first stages: as a consequence, various cooling systems are applied to such devices in order to keep the material temperature at an acceptable level. According to the side of the blade wall

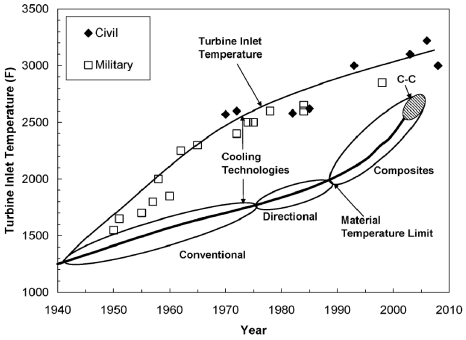


*Figure 1.2: TIT and material limit temperatures during the years [8].*

to which the cooling systems are applied, they can be classified either as *internal* or *external*. Such systems usually employ the working fluid itself (air) as coolant, which is extracted from the compressor at several axial locations. This solution leads to a reduction in engine specific power, since a part of the working fluid does not evolve in the combustion chamber and into a part of the turbine. Moreover, the spent coolant is ejected into the main flow, and the consequent mixing causes both a decrease in main flow enthalpy and the birth of secondary flows. It must also be considered that air presents poor heat transfer properties if used as a cooling fluid. Even so, these disadvantages are broadly counterbalanced by the small dimensions and weight requirements of this kind of systems (which is especially appreciable in aerospace applications) and by the easy coolant procurement.

Since the air evolving in the cooling systems is not employed to produce work, the use of cooling system actually leads to a penalty in the thermodynamic cycle performance, which grows as the amount of air used as coolant grows. As a consequence, it is not suitable to face the increasing heat loads bound to the growing TIT trend by simply increasing the amount of coolant. This requires the development of more and more effective cooling schemes, which are able to provide higher performance while containing the coolant mass flow rate. Moreover, cooling systems are also subject to different constraints, which further enhance the complexity

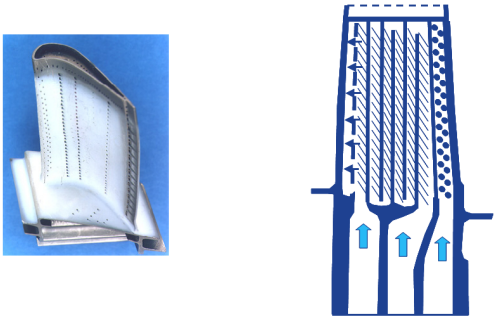

(a) (b)

*Figure 1.3: Example of cooled gas turbine blade (a) and corresponding internal cooling system (b) [13].*

of the design. First of all, air is provided to the cooled devices by means of a complex feeding system, the so-called secondary air system (SAS), whose design is particularly difficult given the spatial constraints and the relevant influence of thermal displacements on the passage sections [9]. Relevant constraints are also provided by the shape of blades and vanes, which results from the aerodynamic design of the main flow path, and by the size of such components (high pressure foils span can be as small as a few centimetres). Finally, also the available manufacturing techniques need to be considered. As of today, turbine blade and vanes are realized by casting through the lost wax process [10]: as a consequence, the achievable complexity of the internal cooling structures is limited by the constraints of such technique. From this point of view, a promising trend is embodied by the recent development of additive manufacturing techniques, which would theoretically allow to realize much more complex geometries [11]: even if at the present day no blades or vanes realized through this technique are operational, other components are already employed both in power generation and aeronautic environments [12], and the development of new thermal treatments for increasing component strength and resilience is aimed at extending the application of this technique to cooled airfoils.

Taking the aforementioned constraints into account, several blade and vanes cooling systems were developed in order to maximize the heat removed by the coolant flow. In this sense, cooled turbine components can be seen as highly specialized and complex heat exchangers [14]. The heat transfer process needs to be considered together with the associated pressure losses: as so, the design of the internal cooling systems requires an accurate knowledge of both fluid-dynamic and thermal phenomena in order to promote heat pickup while limiting pressure losses. Moreover, since present day cooling systems are based upon the combination of different techniques (see Figure 1.3), the performance of the single cooling features may be compounded by their interaction, which requires that the whole cooling system is considered during the design phase. Finally, if the cooling of rotating equipment is considered, the effect of the intense centrifugal field on the internal flow also needs to be taken into account. In order to understand the different features of the system investigated in the present work, a quick overview of internal cooling systems for gas turbine airfoils will be provided in the followings.

### 1.2.1 Internal cooling systems

Internal cooling systems are refrigeration techniques in which heat transfer occurs inside the thermally loaded component. This kind of systems, despite being very different the one from the other, present some commonalities. Almost all highly cooled regions of high pressure turbine components involve the use of turbulent convective flows: heat transfer enhancement techniques make full use of the turbulent flow nature, with the aim to generate mixing mechanisms in the coolant flow that actively exchange cooler fluid for the heated fluid near the walls. According to the different systems, these mechanisms can include shear layers, boundary layer disruption and vortex generation [14]. Unlike convectional heat exchangers, usually gas turbine cooling systems do not rely upon an increase of the cooling surface area: even if this effect may actually be present and beneficial for heat transfer, this is not the primary goal of the systems.

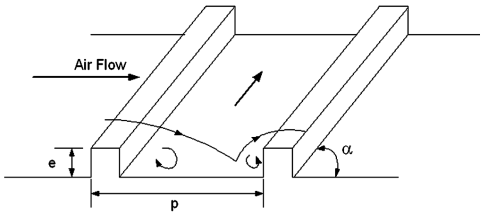


*Figure 1.4: Scheme of flow field induced by ribs [15].*

The main basic cooling system is represented by radial ducts: in their simplest form, they consist in a series of straight smooth channels running parallel to the blade span direction. Such channels can be either single pass or multi pass: in this last case, radial straight sections are connected by U-bends, thus obtaining a serpentine passage. Coolant flow is circulated inside the ducts, in order to remove heat from the blade material by means of solid conduction and internal convection. Spent coolant is finally discharged from the blade tip. Internal smooth ducts are easy to design and manufacture, but present poor cooling effectiveness because of the development of thick dynamic and thermal boundary layers.
In order to enhance heat transfer of the internal ducts, turbulence promoters are employed. One of the most widely employed forms of such devices is the use of ribs (also known as turbulators), which consist of trip strips placed transverse to the bulk flow direction. Their role is to simply trip the boundary layer, thus increasing heat transfer by means of both increased turbulence and flow field alteration. In fact, the main flow separates after the rib and then reattaches after a recirculation vortex: this generates a local impingement zone, and thus a relatively high heat transfer region (see Figure 1.4). The separation, recirculation and reattachment pattern is repeated for each rib, leading to a continuous heat transfer enhancement along the channel if multiple ribs are employed. Thanks to this system, surface averaged heat transfer coefficients within stationary, turbulated passages may be enhanced by factors from 1.8 to 2.8, while the friction factors or required pumping power are increased by factors from 3 to 10 [14].

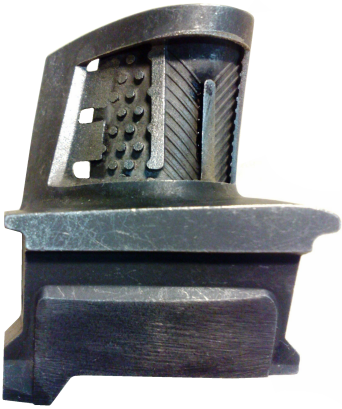

*Figure 1.5: Section of a cooled blade housing pin fins at the trailing edge.*

Another way of improving internal ducts heat transfer is to use pin fins, consisting of cylindrical or prismatic elements having their axes normal to the bulk flow direction and connecting two opposite channel walls. The aim of these elements is to improve heat transfer by means on an increase in turbulence, thanks to the disturbance of channel boundary layer induced by the downstream wake shedding. Pins also conduct thermal energy, so they can even increase heat transfer surface if their lateral area is greater than the base area. Pin fins are usually employed to cool down the airfoil trailing edge, as their application strengthens the structure and improves heat transfer without thickening the cooling channel (see Figure 1.5).

A different cooling approach is exploited by the dimples (also known as concavities), which consist in an array of indentations along the internal surfaces. Such recesses are often spherical in shape. As shown in the scheme of Figure 1.6, if the boundary layer thickness of the flow approaching the dimple is lower than the dimple diameter, the flow enters the dimple forming a separated region on the upstream side, while on the downstream side a flow reattachement region is created, thus enhancing heat transfer [16]. Moreover, the spherical shape creates a vortex struc-

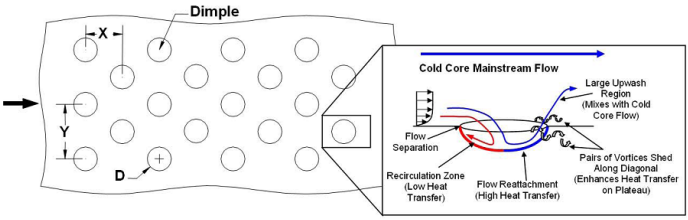


*Figure 1.6: Scheme of flow field induced by dimples [16].*

ture, which is then expelled from the dimple and penetrates into the main flow, increasing the downstream turbulence and thus the heat transfer. The main advantage of dimples is the low pressure drop they produce, despite not being able to provide as much heat transfer increase as the protrusions (ribs or pin fins): in particular, heat transfer enhancements ranging from 2 to 2.5 times over a smooth duct are possible with friction increases from 1.5 to 4 [14].

Both protrusions and concavities are effective ways to cool down the midchord and trailing edge regions of the airfoil, but may result insufficient when considering the leading edge (LE) region. In fact, leading edge cooling is critical for two main reasons: firstly, the strong surface curvature makes the internal area significantly smaller than the external one, and thus the surface available for cooling has a lower extension than the one exposed to the hot gases; secondly, the mainstream stagnation point is located into this region, leading to the highest static pressure and temperature values of the whole blade profile. The situation is further worsened by the impossibility to protect this region with film cooling, since the impingement of the hot gases would disperse any coolant film injected into the mainstream. In order to cool down this region, showerhead technique has been developed. Such system consists in the manufacturing of a hole array in the blade wall, through which cooling flow is expelled: in this way a heat sink effect is created, removing heat directly from the material thickness. The relative small length of these holes increases this effect, preventing a complete development of the boundary layer and taking advantage of the high heat transfer typical of transitioning flows.

Showerhead holes are usually realized with their axes inclined with respect to the profile normal direction. thus preventing hot gas ingestion and increasing the heat transfer area.
Another widely employed and highly effective cooling technique is the jet impingement, which consists in the realization of a high velocity coolant mass flow, ejected from a hole or a slot and directed towards the heat transfer target surface. This allows both to increase the inner flow turbulence and especially to obtain a very thin thermal boundary layer in the surroundings of the jet stagnation point. Both of these phenomena greatly improve the heat transfer, which leads impingement cooling to show the highest potential heat transfer improvements amongst all the heat transfer enhancement techniques [7]. Furthermore, coolant jets reach the target surface having exchanged a negligible amount of heat with the blade itself, thus maximizing convective heat transfer. In order to realize an impingement cooling system, two separate cavities need to be realized inside the blade, separated by a baffle housing the impingement holes. This setup is obtained in gas turbine vanes by inserting thin perforated liners inside the vane cavities, which allows to use impingement cooling in both leading edge and midchord regions. On the other hand, this solution is difficult to apply to gas turbine blades, since it is not compatible with the strong centrifugal loads occurring in rotating conditions. As a consequence, impingement cooling is only applied to the most thermally stressed regions, such as the leading edge, and with different configurations. A typical setup employed for rotating blades consists in the creation of a series of impingement jets inside the leading edge inner cavity, which impact on the inner surface and thus perform an intense cooling action. Such jets are usually fed by a radial feeding channel, directly located downstream the leading edge cavity. Since coolant air temperature undergoes a relatively low increase along the supply channel, this design usually takes the name of *cold bridge*. This configuration is usually applied along with showerhead and, occasionally, with film cooling. An example of the different implementations of impingement cooling for vanes and blades is reported in Figure 1.7.

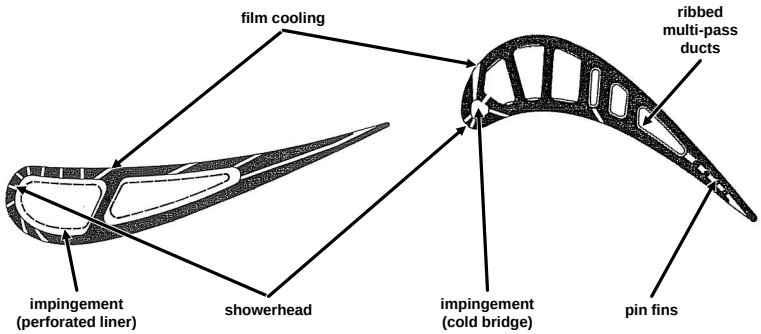


*Figure 1.7: First stage vane (left) and blade (right) of NASA $E^3$ engine [7].*

Given the importance of impingement cooling in the framework of the present work, a detailed discussion of the flow phenomena associated with jet impingement will be performed in Section 1.3.

### 1.2.2 Effect of rotation on internal cooling

The discussion presented in the previous sections made possible to understand the complexity of the flow field involved by airfoil cooling systems. This complexity is further increased if such systems are applied to gas turbine blades, since rotational forces add another dimension to the flow analysis. In fact, the coolant flow inside the internal ducts of a rotor airfoil is subject to inherent forces of rotation (namely Coriolis and rotational buoyancy forces), which may significantly alter mass flow distribution and thus heat transfer for the channel as well as for all the downstream connected cooling systems.
The main flow driving phenomenon related to rotation is the birth of the Coriolis force, which is a function only of the flow field and rotational condition and thus influences the flow field regardless of thermal conditions or heat transfer. For a flow particle of mass $m$ flowing with a velocity $\vec{U}$ relative to an environment spinning with a rotational speed $\vec{\omega}$, Coriolis

force can be expressed as:

$$\vec{F}_{Co} = -2m\vec{\omega} \times \vec{U} \tag{1.1}$$

If an internal duct is considered, the influence of such force on the internal flow field is given by the Rotation number [7], which represents the relative strength of the Coriolis force to the bulk inertia and can be expressed as:

$$Ro = \frac{\omega D}{U} \tag{1.2}$$

where $D$ is the characteristic length of the system (the hydraulic diameter in this case) and $U$ is the average flow velocity.
Given its definition, the effect of Coriolis force depends upon the relative direction of flow velocity and rotational speed, and is thus different in different locations of the cooling system. Considering a flow inside a channel with a radially outward motion, the fluid particles will be subject to a Coriolis force opposite to the tangential velocity: as a consequence, the flow will be driven along the channel trailing side, which for a turbine blade is the one closer to the pressure side. This asymmetric mass flow pattern also leads to an increase in heat transfer for the channel trailing side [17], since the coolant tends to impinge and flow along such surface. The opposite situation occurs on the leading surface, which for a gas turbine is the one closer to the suction side, where the flow velocity decreases and so does the heat transfer. For a radially inward flow the effect is reversed: flow tends to be driven along the leading side, which experiences a velocity and heat transfer enhancement, while the opposite occurs for the trailing surface.
The ideal two-dimensional situation described above becomes way more complex when the actual three dimensional extension of the channel is considered. In this case, the different axial velocities across the channel cross-section lead the magnitude of Coriolis force to be different in different points. With a simple square channel cross-section, this phenomenons generates two counter-rotating vortices, as illustrated in Figure 1.8, but much different flow arrangements are possible according to the

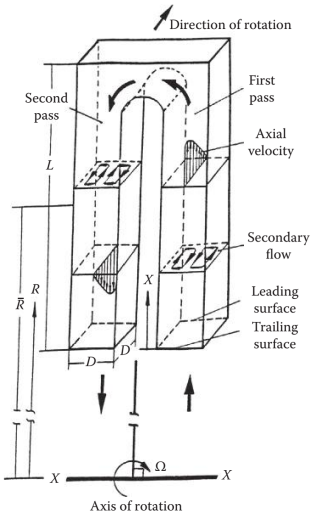


*Figure 1.8: Scheme of the secondary flows induced in a two-pass square channel by Coriolis force [18].*

cross-section shape and orientation [19].

The second relevant contribution of rotation to flow field and heat transfer is given by the rotational buoyancy forces. Due to heat transfer phenomena, the coolant temperature varies along the cooling system, and so does its density. In static components (e.g. vanes), the gravitational buoyancy induced by such differences is negligible with respect to the flow inertia [7]. However, considering gas turbine blades, the high rotational speeds create a strong centrifugal field for the coolant flowing inside the cooling system: in this case, density driven buoyancy forces may reach levels comparable with the flow inertia, and thus significantly alter the flow structure. The relative strength of the rotational buoyancy force to the bulk inertia is given by the density ratio [17], defined as:

$$DR = \frac{\rho_{in} - \rho_w}{\rho_{in}} \tag{1.3}$$

where $\rho_{in}$ is the inlet coolant density and $\rho_w$ is the coolant density at the wall temperature. The analysis of convective heat transfer inside a rotating duct allows to relate this parameter to the cooling performance, which is

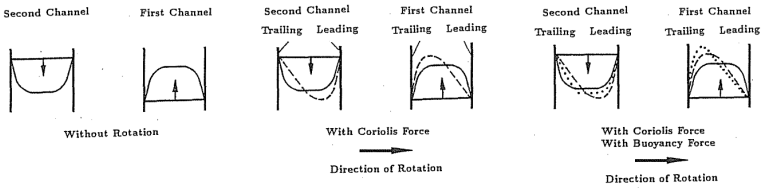


*Figure 1.9: Scheme of the effects of inertia, Coriolis and rotational buoyancy on the velocity profile of radially outward and inward flows [18].*

achieved by reformulating $DR$ as the so-called buoyancy parameter [20]:

$$Bo = \frac{\rho_{in} - \rho_w}{\rho_{in}} Ro^2 \frac{r}{D} \tag{1.4}$$

where $r$ is the local radius. Buoyancy effects are able to strongly affect the velocity profiles inside the cooling channel [21]. Considering the case presented in Figure 1.8, in the radial outward channel Coriolis forces drive the cooler flow close to the trailing side: as a consequence, denser fluid will be found in this region. The strong centrifugal force will drive such denser coolant towards the outer radii, thus increasing the flow velocity close to the trailing side. The opposite phenomenon occurs on the leading side, where Coriolis forces drive the hotter and less dense flow and thus buoyancy forces are directed towards the inner radii. As a consequence, in a radial outer channel buoyancy forces intensify the flow unbalance related to Coriolis effect: at a certain point, buoyancy effects can even be strong enough to cause flow separation on the leading side [17, 21]. In a radial inward duct, the effect is reversed: the denser coolant flows along the leading side towards the inner radii, while buoyancy pushes it in the opposite direction; meanwhile, the hotter fluid along the trailing side is forced towards the inner radii. The resulting outcome is a weakening of Coriolis effects and a more uniform velocity profile. Referring to the two-pass square channel of Figure 1.8, a scheme of the combined Coriolis and buoyancy effects on the duct velocity profile is reported in Figure 1.9.

## 1.3 Impingement flow field

Impingement cooling technique consists in the impact of a fluid jet on a solid surface: such phenomenon generates an array of complex flow structures, which interact with each other and with the surrounding fluid. Moreover, if cooling is applied to a rotating device, inherent forces of rotation may affect flow field. The importance of jet impingement for the present work requires a more detailed analysis of such phenomena and interaction, which will be presented in the followings.

### 1.3.1 Single jet impingement

An impingement jet can be defined as a high velocity coolant mass ejected from an orifice (either a hole or a slot) that impinges on the heat transfer surface [7]. The velocity and temperature profile and the turbulent characteristics at the orifice outlet depend upon the supply condition. For a pipe-shaped nozzle, the velocity profile will present a parabolic shape and moderate amounts of turbulence. On the other hand, if the jet is generated by a thin perforated baffle the outlet velocity profile will be flat and less turbulent than with a pipe orifice. In this case, a downstream jet contraction (*vena contracta*) will also more likely to occur [22].
Gas turbine cooling applications usually employ submerged (i.e. surrounded by the same kind of fluid) and confined (i.e. ejected form an opening on a wall) jets. A scheme of a similar flow situation is reported in Figure 1.10. In order to characterize the flow conditions for impinging jets, the corresponding Reynolds number is employed:

$$Re_j = \frac{UD_j}{\nu} \tag{1.5}$$

where $U$ is the average jet velocity, $D_j$ is the orifice hydraulic diameter and $\nu$ is the fluid kinematic viscosity. According to the value of $Re_j$, different flow regimes can be identified [23]:

- dissipated laminar jet ($Re_j < 3 \cdot 10^2$);

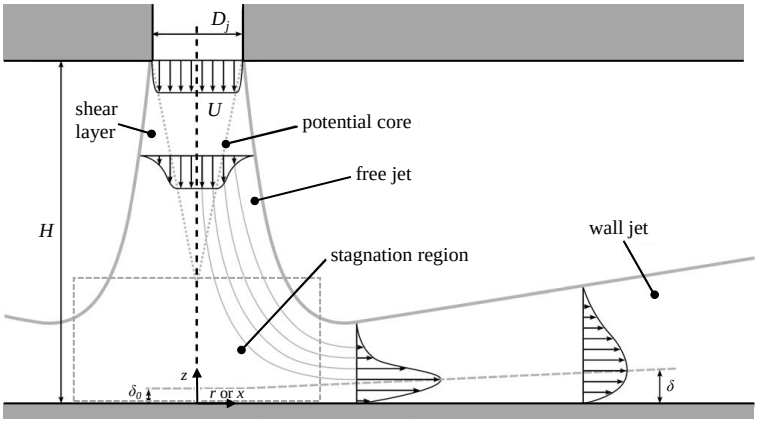


*Figure 1.10: Scheme of a submerged and confined impingement jet [23].*

- fully laminar jet ($3 \cdot 10^2 < Re_j < 1 \cdot 10^3$);
- transitional or semi-turbulent jet ($1 \cdot 10^3 < Re_j < 3 \cdot 10^3$);
- fully turbulent jet ($Re_j > 3 \cdot 10^3$).

Since in most engineering problems, and in gas turbine cooling in particular, only fully turbulent jets are encountered, the following analysis will consider this flow regime. In this condition, three zones can be identified within the flow field (see Figure 1.10): the free jet region, the stagnation region and the wall jet region.

The *free jet region* is directly located downstream the orifice: its name is due to the fact that in this region the jet is not influenced by the presence of the target surface and thus behaves like a free submerged jet. The velocity gradients between the jet and the surrounding fluid create a strong turbulent mixing region, named *shear layer*: as a consequence, jet entrains a part of the neighbouring fluid and its mass flow rate increases. The shear stresses also diminish the jet energy and widen the velocity profile, thus spreading and slowing down the jet. The shear layer expands both laterally and towards the jet axis. The jet central region, which is unaffected by the developing shear layer, is named *potential core*: in this region, the velocity is still equal to the bulk velocity. The shear

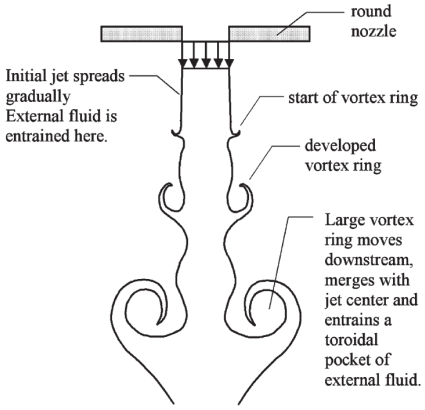


*Figure 1.11: Flow instabilities development in the free jet region [22].*

layer expansion progressively erodes the unaffected jet region and thus limits the downstream extension of the potential core to four to eight nozzle diameters [22]. The dispersion of the potential core marks the start of the jet decaying region: in the central part of the jet velocity decreases and turbulence increases (*developing zone*), up to the point where a Gaussian-shaped axial velocity profile is obtained (*fully developed zone*) [24]. Even so, in most cooling applications nozzle-to-target surface distance $H$ is too small to allow a complete development of the jet; moreover, if such distance is lower than two diameters the free jet region itself may actually not exist, due to the influence of the elevated static pressure of the stagnation region.

The free jet region is one of the main sources of turbulence and unstable flow structures for an impinging jet: the shear layer generates flow instabilities similar to the Kelvin-Helmholtz one, especially for high $Re_j$ values. Directly downstream the nozzle, velocity oscillations may occur inside the shear layer, which get carried downstream by the jet itself and grow to finally form large scale eddies (see Figure 1.11). The largest eddies have a length scale of the same magnitude of the jet diameter: as a consequence, if the nozzle-to-target distance is large enough they are able to completely disrupt the jet structure, leading to a strong reduction of heat transfer

performance. To avoid such occurrence, nozzle-to-target is limited in most applications: in particular, for gas turbine cooling systems it usually ranges from one to three nozzle diameters [7].
When the jet approaches the target surface it interacts with the solid wall, thus defining the *stagnation region*. In this zone, whic extends to a normal distance to approximately 1.2 $D_j$ from the wall [25], the turning of the flow takes place, transforming the axial velocity component into an accelerating radial component. The positive pressure gradient creates a laminar boundary layer surrounding the stagnation point, whose thickness is however kept small by the flow acceleration: as a consequence, in a cooling application strong temperature gradients are present at the stagnation point [26], which greatly enhance heat transfer despite the low flow velocities [7].
Surrounding the stagnation region, the flow moves radially outwards along the solid wall, thus defining the *wall jet region*. After having reached a maximum at around one jet diameter from the stagnation point [27], radial velocity progressively decreases in this region, due to the increase in passage area as the radial distance increases and to the interaction with both the wall and the surrounding fluid. This deceleration is usually accompanied by the transition to turbulent flow, since the stabilizing effect of acceleration is no more present [23]. The turbulent transition is also promoted by the impact of large scale eddies carried by the jet shear layer [26].
The flow field described in the previous paragraphs is directly related to the heat transfer pattern on the target surface. For a single impinging jet, heat transfer peaks can be observed both at the jet stagnation point (primary peak) and at a certain radial distance from it (secondary peak). While the primary peak is clearly related to the low boundary layer thickness in this zone, the secondary peak is usually attributed to the flow transition from laminar to turbulent [23]. Since this last phenomenon is also related to the impact of the shear layer vortices, a strongly unsteady heat transfer pattern can be expected in this region. The entity of the secondary peak seems to increase as Reynolds number increases and as

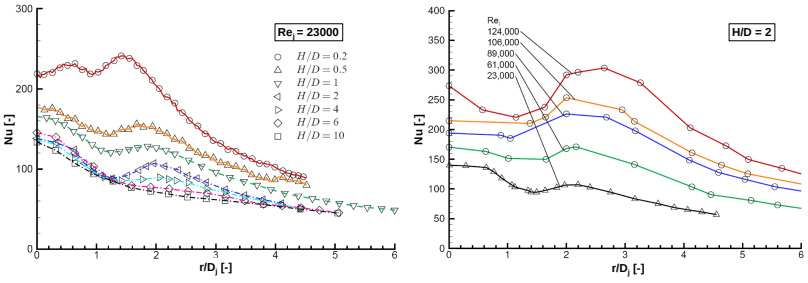


*(a)* *(b)*

*Figure 1.12: Effect of separation distance (a) and Reynolds number (b) on jet heat transfer [23].*

the nozzle-to-target surface distance decreases: examples of these dependencies are reported in Figure 1.12 where local heat transfer performance expressed as Nusselt number is plotted against different values of the aforementioned parameters.

### 1.3.2 Rotational effects on impingement

If impingement cooling is applied to a rotating environment, rotational effects can significantly alter the flow and thermal phenomena. In this case, the effects are mainly related to Coriolis force, and thus strongly depend upon the relative direction of the jet with respect to the rotation axis.

If the impingement jet is parallel to the rotation axis, no Coriolis force acts on the jet itself. Even so, this does not occur for the wall jet region, as illustrated in Figure 1.13: a turning motion is generated for the wall flow, which in turn causes a secondary swirling flow that enhances the jet mixing with the surrounding fluid. As a consequence, a decrease in jet momentum and a thickening of the boundary layer are obtained, which are both detrimental for cooling performance.

If the impingement jet direction is not parallel to the rotation axis, the jet itself is subject to the action of Coriolis force: the effect of such interaction is illustrated in Figure 1.14. If the jet axis lies in a tangential plane and

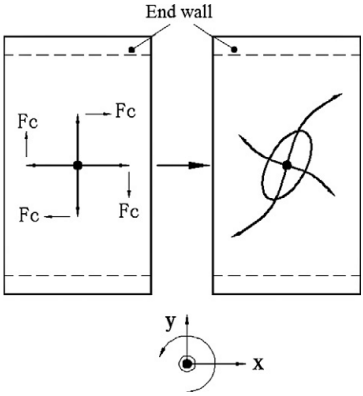


*Figure 1.13: Effect of Coriolis forces for a jet parallel to rotation axis [28].*

has a leading orientation, a radially outward Coriolis force is generated, which drives the flow in the corresponding direction. The opposite occurs if the jet has a trailing orientation, with Coriolis force driving the flow towards the inner radii. For turbine blade cooling applications, leading and trailing orientations occur if the jet is directed towards the suction and the pressure side respectively. The overall effect on heat transfer of such interaction is usually detrimental, since the velocity component normal to the target decreases.

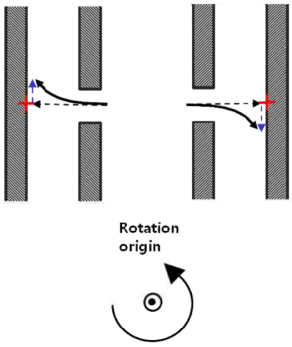


*Figure 1.14: Effect of Coriolis forces for leading (left) and trailing (right) jet orientations [29].*

The ideal rotational effects presented in this section can be strongly altered by the geometry of the cooling system (e.g. orifice or target surface shape). Moreover, jet flow field can be further influenced by the rotational effects on other features of the cooling system, both in terms of Coriolis and buoyancy driven secondary flows: as a consequence, a complete analysis of the whole cooling system is usually required to evaluate the overall rotational effect on impingement cooling performance.

## 1.4 Leading edge impingement cooling

Jet impingement cooling is a widely applied technique for the leading edge of gas turbine blades, since its outstanding cooling performance allows to manage the high thermal loads present in this region (see Section 1.2.1). However, when a real cooling system is considered the flow and heat transfer features of the jets can be much different from the ones presented in Section 1.3. In fact, in a leading edge impingement system the coolant is usually supplied by a feeding channel: the upstream radial flow velocity effect on the jet supply condition thus needs to be taken into account. This kind of systems also employ multiple jets, which may actually interact with each other both in the free jet region and on the target surface, and the strong curvature of the heat transfer surface may lead to a flow field significantly different from a flat wall. Finally, the coolant outlet condition is also different, due to the presence of film cooling and showerhead holes on the target surface. All of the aforementioned phenomena significantly part the cooling performance of a LE system from the ideal one: in particular, the parameters which can influence flow field and heat transfer include jet Reynolds number, shape, location and number of impingement holes, jet nozzle-to-target surface spacing, jet feeding condition, LE surface shape and sharpness, extraction holes size and arrangement and distribution of the cooling flow among the available flow paths. The effects of these and other parameters are compounded by their interaction. It is clear that the extent and the complexity of such problem require a detailed study of the many aspects

involved by jet impingement, which has been performed since the first implementations of such cooling technique. In particular, amongst the first studies concerning impingement cooling systems, the most relevant contributions were provided by Kercher and Tabakoff [30], Martin [25], Florschuetz et al [31, 32], Behbahani and Goldstein [33]: all of these works focus either on a single jet or on an array of jets impinging onto a flat target surface. The outcomes of these and many other works allow to identify the main flow and geometric parameters influencing impingement flow field and heat transfer performance, which will be separately discussed in this section.

**Effect of Reynolds number** All the investigations agree that impingement heat transfer performance, expressed as Nusselt number value, increases as jet Reynolds number grows, with the first being proportional to a power of the second. Even so, the value of $Re_j$ exponent is thought to depend upon the jet flow conditions: values of such parameter ranging from 0.5 to 0.8 are found in the open literature, according to the predominant laminar or turbulent nature of the flow. In fact, for an impingement jet the flow within the potential core can be considered inviscid and, therefore, laminar [34]: as a consequence, $Re_j$ exponent may vary according to the interaction of such flow structure with the target surface.

**Effect of jet-to-target wall spacing** Most of the literature also agree on the heat transfer dependency upon jet-to-target plate spacing $H$: cooling performance increases as $H$ decreases, but the relation between these parameters is not monotonic. For very small values of such parameter (below $H/D_j < 1$) heat transfer increases as $H/D_j$ decreases [24], which is mainly due to the increasing value of the secondary peak. However, such small $H/D_j$ values are of limited interest for engineering practice. For higher $H/D_j$ values, little effect of this parameter is recorded on cooling performance, until the spacing is large enough for the jet velocities to significantly drop. This phenomenon, which is associated with the

potential core dispersion, usually occurs for $H/D_j$ values around 6. In fact, as long as the potential core exists the jet velocity does not change significantly, and so does the cooling performance. Accordingly, above $H/D_j = 6$ heat transfer significantly decreases as $H$ increases.

**Effect of jet-to-jet spacing** As regards jet-to-jet spacing, it is a common finding that a decrease of this parameter leads to an increase in heat transfer. Even so, this increase is mainly bound to the higher number of jets impinging in the same area and thus to a higher coolant consumption, and not an actual increase in the stagnation point cooling performance. Moreover, when jet-to-jet distance decreases the jets may actually start interacting with each other. A commonly observed phenomenon, illustrated in Figure 1.15, occurs when the wall flows of two adjacent jets interact: in this case, a fountain like structure is generated [22], with the coolant perpendicularly leaving the target surface and forming two big counter rotating vortices with the impingement jets (*primary vortices*). Flow detachment decreases heat transfer, but in between the detachment locations a flow recirculation is created, generating two counter rotating small vortices (*secondary vortices*): this leads to a local impingement zone, where heat transfer can be as high as in the jet stagnation region [35, 36].
An additional phenomenon which needs to be taken into account when reducing jet-to-jet spacing is the internal crossflow: in fact, if an array of jets is considered and the spent coolant is extracted from a side of the array, the spent coolant flow tends to run over the impingement jets,

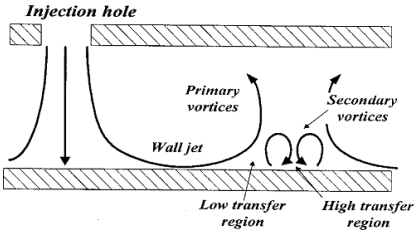


*Figure 1.15: Scheme of the fountain effect [35])*

deflecting them and thus significantly degrading heat transfer performance [31]. This negative effect is avoided if spent coolant is drawn instead by extraction holes located on the target surface [36].

**Effect of Mach number** Since high flow velocities are reached for impinging jets, the effect of jet Mach number also needs to be discussed. Most of the investigations are performed in low velocity conditions, thus a small amount of data is present in the open literature on this relation. However, dedicated studies on this subject (e.g. the ones of Brevet et al. [37] and Goodro et al. [38]) all agree that the influence of Mach number is negligible if the value of such parameter does not exceed 0.2. Above this value, a strong increasing dependence of heat transfer is recorded.

**Effect of wall-to-jet temperature ratio** Another parameter which is not usually considered when studying impingement heat transfer is the ratio of wall and jet temperatures. When this is done (e.g. by Goodro et al. [39] and Cocchi et al. [40]), the experimental outcomes show that increasing wall-to-jet temperature ratio is detrimental for heat transfer. However, this phenomenon is mainly attributed to the fluid properties being a function of jet temperature: as a consequence, care should be taken when choosing the reference temperature employed for the evaluation of such properties.

**Effect of target surface curvature** The general trends previously presented for a flat target surface can be observed also if the jets impinge on a concave surface, which better represents a blade leading edge. Even so, surface curvature can strongly modify the flow field, and thus the heat transfer pattern, of an impingement system: a sharp target surface can lead the jet to impinge first on the side walls, resulting in a significantly different heat transfer pattern with respect to a flat plate (Metzger et al. [41]). Moreover, the flow surrounding the stagnation point interacts with the curved surface, leading to a higher heat transfer with respect to a flat target plate namely due to the initiation of Taylor-Görtler vortices (Gau

and Chung [42]). As regards the effect of target surface sharpness, in a pioneering work Chupp et al. [43] studied the impingement of a row of round jets on a semi-cylindrical surface, and managed to correlate heat transfer to Reynolds number, jet-to-target and jet-to-jet spacings and target surface curvature. As regards this last dependency, it was found that cooling performance in the stagnation point slightly increases as target surface radius increases, while the average cooling performance on the whole profile slightly decreases. A similar conclusion for curvature effect on average Nusselt number value was also found by Hrycak [44]: a stronger curvature (i.e. smaller curvature radius) lead to a higher heat transfer. A more detailed analysis was performed in a study of Bunker and Metzger [45]: their results show that, as leading edge sharpness increases, heat transfer drops in the target surface center (i.e. at the jet stagnation point) and secondary heat transfer peaks are created on the sides of the surface. The same effect was also observed in a recent study by Facchini et al. [46], which observed an increase in side walls heat transfer with a narrower surface opening attributed it to the reduced jet-to-target surface distance and jet spreading. As a general conclusion of these works, it can be stated that a sharper target surface is positive for average heat transfer due to the larger contribution of the side walls, but care should be taken that such overall increase is not detrimental for stagnation region heat transfer.
Since target surface curvature significantly affects the flow development, it may also have an influence on the Nusselt number dependency upon the jet Reynolds number. In particular, Hrycak [44] observed that, for $H/D_j$ values between 2 and 8, target surface curvature and relatively small spacing provide minimal room for the wall jet to develop away from the stagnation region: this in turn may reduce the Reynolds number exponent of the $Nu$-$Re_j$ relation, which in this study was found to be around 0.63.

**Effect of coolant extraction** Leading edge impingement is made even more complex by the presence of showerhead and film cooling systems,

whose holes draw the spent coolant flow from the impingement cavity. The effect of such coolant extraction is mainly positive, since it prevents the formation of a detrimental crossflow inside the leading edge (Jordan et al, [47], Taslim et al. [48]). Even so, new flow paths are provided which can influence the cooling performance in either a positive or a negative way: according to Metzger and Bunker [49] if showerhead extraction is present heat transfer increases with aligned impingement and extraction holes, and slightly decreases with out of phase holes. This and other works also found that an asymmetric flow extraction between pressure and suction side has little effect on overall heat transfer (Taslim et al. [50]) but can significantly alter local values (Facchini et al. [51]).

**Effect of supply condition** Supply conditions can also have an impact on the system cooling performance. Due to the high flow velocities inside the radial feeding channel, a so-called upstream crossflow is present for the impingement jets: as a consequence, a residual component of radial momentum can be transported inside the holes and then into the cavity. Since this component is perpendicular to the impingement jet, it may cause the jet itself to bend in the outer radial direction. One of the first contributions on the effect of supply condition was provided by a series of works by Taslim et al. [48, 50, 52, 53, 54], which investigated a wide range of geometries with different inlet and outlet conditions. All of these works evidenced that providing coolant from one side or both sides of the feeding channel has a negligible effect on heat transfer. Even so, since all of the feeding flow is employed for jet supply, the effect of a large inlet crossflow is not investigated in these works. Higher upstream velocity magnitudes were investigated by Jordan et al. [47, 55] and Harmon et al. [56] for different impingement hole lengths, shapes and edge filleting conditions. These works show that high upstream crossflow velocities degrade heat transfer, mainly due to the jet being inclined with respect to the target surface. Sensibility to upstream crossflow grows as the hole length decreases and as the hole fillet radius increases. Even so, as observed by Andrei et al. [57] and Massini et al. [58] inlet crossflow effect

inside the impingement hole can also vary its apparent passage section, thus altering the jet shape and increasing its lateral spreading: this, in conjunction with a narrow leading edge opening angle, can compensate the heat transfer degradation, causing inlet conditions to have only local effects.

**Effect of holes shape and location** The main phenomenon driving the impingement heat transfer is the interaction between the jet flow field and the solid wall: as a consequence, it can be expected that different hole shapes and locations lead to a different cooling performance. This is particularly true for leading edge cooling, where the target surface curvature and the strong confinement further enhance the effects of different flow arrangements. A geometry of recent interest consists in racetrack-shaped holes: the rationale behind this geometry is the possibility to obtain a better coverage of the leading edge surface, allowing to direct the coolant flow where required. Coherently with such intent, dedicated investigations like the ones of Taslim et al. [52, 59] and Harmon et al. [60] found that racetrack shaped jets generally outperform the circular ones both in static and in rotating conditions.
As regards holes location, the effect was investigated by Facchini et al. [51] for a staggered array of round holes: their result show that, for a wedge-shaped LE surface, heat transfer is enhanced as jet-to-jet lateral spacing increases (i.e. as the holes move towards the side walls) due to the consequent jet-to-target wall reduction. In a related work by the same authors [46] the effect of different impingement holes diameters, shapes and arrangements was studied: even if a systematic comparison was not performed, the obtained results show that strongly different heat transfer patterns are obtained for different geometries.

**Effect of rotation** If impingement cooling is applied to a blade leading edge, rotational effects can significantly alter internal flow field and thus heat transfer pattern: as a consequence, it is of particular interest to evaluate the effects of rotation on jet impingement. The first significant

studies on this subject were performed by Epstein et al. [61] and Mattern and Hennecke [62], which investigated the effects of different Rotation numbers and stagger angles (i.e. angles between jet and rotation axis): both studies evidenced a decrease in heat transfer with an increase in rotational speed, with a noticeable influence of stagger angle. More recently, a wide range of contributions on this subject were provided by the works of Iacovides et al. [63], Hong et al. [64, 65, 66] and Deng et al. [28]. A common finding of these studies is that Coriolis force can influence jet impingement by acting either on the jet itself or on the wall flow surrounding the jet stagnation point, according to the mechanisms illustrated in Section 1.3.2. The result of such interaction is usually a decrease in heat transfer, due to a reduction of jet momentum normal to the surface or to a higher flow entrainment. On the other hand, Massini et al. [58] demonstrated that for a complete cold bridge type cooling system the main Coriolis effect can occur in the feeding channel, causing an impingement jet deflection towards the side walls but no significant effect on average heat transfer. Jung et al. [29] showed that rotation can even increase heat transfer, but only for small jet-to-target plate distances and if crossflow and Coriolis force induce opposite jet deflections. Finally, strong heat transfer enhancements (up to 3-4 times) with jet Rotation numbers exceeding 0.03 were measured by Harmon et al. [60] and Elston et al. [67], which justified their findings with the increased mixing due to rotation. As a general consideration, it is evident that rotational effect on leading edge impingement are strongly dependent upon the investigated geometry and conditions, and therefore are difficult to predict. As a consequence, in this case it seems particularly important to replicate all of the geometric and flow features in order to obtain meaningful result.

**Numerical approach to leading edge impingement cooling** In order to expand the comprehension of the underlying physical phenomena, as well as to develop reliable predictive tools for cooling systems design the experimental approach to the impingement problem was followed by analytical and numerical researches on the same subject. Numerical

studies on impingement heat transfer were performed using two-equation turbulence models by Polat et al. [68] and Ashforth-Frost and Jambunathan [69], while Coussirat et al. [70], Morris et al. [71] and Souris et al. [72] also compared two-equation models with more complex Reynolds stress models. As a general point, these works seem to indicate that the most suitable and accurate numerical setup strongly depends upon the particular test case. Even so, the review performed by Zuckerman and Lior [22] indicates that k-$\omega$ SST and $v^2$-$f$ models represent the best compromise between accuracy and computational cost for most of the jet impingement calculations. In agreement with such statement, Kumar and Prasad [73] simulated the experimental case of Bunker and Metzger [45], finding that k-$\omega$ SST model provides reliable results for impingement cooling investigation on concave surfaces, while Taslim et al. [53, 74] and Jordan et al. [55] obtained a good agreement with the experimental data employing $v^2$-$f$ model. In this last study, however, it is also shown that $v^2$-$f$ fails to accurately replicate heat transfer phenomena when a strong inlet crossflow is combined with jet impingement.

As regards the present work, similar leading edge geometry and flow conditions were investigated in a series of works by Bianchini et al. [75] and Andreini et al. [76], in which the good agreement between experimental and numerical data obtained using k-$\omega$ SST model allowed to develop an interpretation for the obtained heat transfer pattern. Even so, it was demonstrated in a subsequent work [77] that scale resolving hybrid RANS-LES model are able to provide much greater accuracy and detail, due to the strongly unsteady flow field involved by impingement jets, even if this improvement is obtained at the cost of a much higher computational effort. As a final consideration, it can be stated that RANS simulations employing k-$\omega$ SST or $v^2$-$f$ models are a viable tool for obtaining reliable information on leading edge impingement cooling systems, but also that scale resolving models can be considered when higher detail on particularly complex flows is required.

## 1.5 Thesis outline and motivations

The literature data presented in the previous section reveal that leading edge impingement is a complex phenomenon, and that both heat transfer and flow field are the result of many interacting features. Amongst the various effects driving the cooling performance, the interaction between the jets and the curved target surface is particularly relevant. For a given coolant mass flow rate, different jet locations and diameters lead to strongly different jet-wall interactions: therefore, the consequences of different impingement coolant distributions on the system performance embody a relevant matter of study. In order to highlight this effect, three different impingement geometries were investigated in this work. Such geometries were designed in order to have the same overall passage area, thus providing the same average jet velocity for a given coolant mass flow rate: in this way, the different phenomena which will be evidenced for the three geometries will only be related to the different coolant arrangement. Moreover, the effect on leading edge cooling of other features, even if well documented by various works, is still unclear: in particular, supply conditions, coolant extraction arrangement and rotation affect flow and thermal characteristics in a way which is both significant and difficult to predict. Starting from this consideration, one of the main goals of this work is to provide a deeper insight on the relations between such effects and impingement cooling performance. In particular, the effect of jet supply conditions was studied by replicating different blade radial sections, for which the supply channel velocities range between negligible to almost equal to jet velocity. The effect of coolant extraction was studied using a non uniform pattern of extraction holes with respect to the various impingement jets: in this way, each jet presents a different extraction pattern, thus allowing to evaluate the corresponding differences in heat transfer pattern; moreover, since in the actual hardware a periodic pattern between impingement and extraction holes is rarely present, a more realistic condition is also obtained. Extraction effect was further stressed by varying the mass flow split between the different rows of

extraction holes for selected test cases. Considering the rotational effects, all the geometries were investigated both in static and rotating conditions. Performing such investigation for a complete cooling system also allows to take into account the rotational influence on its different features, which can actually alter the flow field also for the other parts of the system and eventually modify the heat transfer pattern in a complex way.
A particular care has also been taken in replicating most of the features of a real cooling system, the only simplifications being imposed by the requirements in terms of measurement and rig manufacturing: in this way, a case which is more representative of a real gas turbine component is obtained, thus allowing to retrieve significant information on the phenomena actually occurring in the real case.
Finally, in order to obtain a full comprehension of the underlying physics, the experimental campaign has been supported by an extensive numerical investigation, which many literature works demonstrated to be a reliable tool for studying internal cooling systems. As so, in the present case not only the most suitable computational setup has been determined and validated, but its outcomes have been thoroughly exploited, in order to obtain a region by region relation between both steady and unsteady flow phenomena and the resulting heat transfer distribution. This combined numerical and experimental investigation overcomes the weaknesses of the two segregated approaches and is thus capable to provide a complete understanding of the investigated case.

# Chapter 2

# Heat transfer measurement

The analysis presented in Chapter 1 suggests that the definition and quantification of convective heat transfer parameters is essential in order to study gas turbine cooling systems and evaluate their performance. Even so, heat transfer phenomena play a fundamental role in a much wider range of applications, including thermal control of electronic devices, design of heat exchangers, air conditioning, refrigeration and many others [20].

With respect to other environments, heat transfer phenomena related to gas turbine cooling are considerably simplified, dealing with a single phase, single substance fluid in forced convection and with no chemical reactions. However, the geometrical situation is often highly complex, so that the flow is usually turbulent with highly three dimensional velocity and temperature fields: this leads to strong variations in the local heat transfer characteristics. Since the engine component walls are relatively thin with respect to other applications, these local variations lead to strongly non uniform temperature distributions, which significantly affect the thermal stresses and durability of the components. As a consequence, high accuracy and spatial resolution are required when studying the heat transfer characteristics of such devices. Moreover, when the cooling of rotating equipment (e.g. blades) is considered, the effect of Coriolis and

buoyancy forces on flow field and heat transfer needs to be taken into account. This situation makes the experimental study of such systems challenging, since it is necessary to derive local heat transfer information on the surfaces of all geometrical elements while replicating the actual operating conditions.
In order to provide reliable heat transfer data in gas turbine cooling systems, a wide range of measurement techniques has been developed. In this chapter, an overview about the fundamental principles and assumptions of some of these experimental approaches will be provided, with a particular focus on the technique employed in the present investigation.

## 2.1 Overview of heat transfer measurement techniques

During the years, a wide range of experimental methodologies has been developed to measure convective heat transfer, each suitable for different kinds of environments and applications. Such techniques differ for the employed experimental procedure (transient or steady-state) and for the physical quantities evaluated to determine heat transfer (temperature or heat flux). According to such differences a classification can be performed, a scheme of which is reported in Figure 2.1. For a deeper discussion on experimental techniques, the reader can refer to von Wolfersdorf and Weigand [20].
The choice of the most suitable technique for the analysis of the present case needs to take into account the advantages and the constraints of the different methods, which will be briefly explained in the followings.
Steady-state heat transfer measurement techniques are based upon the creation of a time independent heat transfer between wall and fluid, which allows to evaluate the convective heat transfer coefficient through a direct application of the energy balance. The heat exchange phenomenon is usually obtained by heating up the solid surface: in this way, different thermal boundary conditions (uniform temperature or uniform heat flux) can be obtained according to the employed technique. A particularly

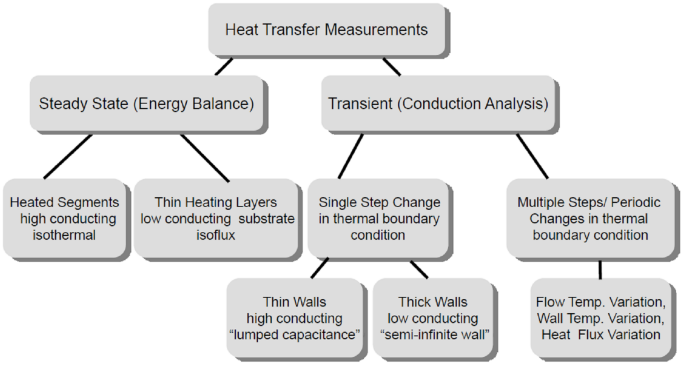


*Figure 2.1: Classification of heat transfer measurement techniques [20].*

desirable feature of steady-state methods is the capability of providing a well-controllable thermal condition, which in turn usually provides robust results. Even so, in order to heat up the investigated surface heating elements need to be employed, which impose constraints either on the complexity of the geometry or on the achievable spatial resolution. In fact, if the heating element is directly applied to the surface (as in the *thin heating foil* technique), only flat or single curvature surfaces can be studied; on the other hand, if more complex shapes need to be considered (which can be obtained with the *heated segments* method) the need of using high conductivity samples only allows to obtain area averaged values of the thermal variables.

In order to overcome the issues of steady-state methods, transient techniques were developed. Such techniques involve the study of an unsteady thermal phenomenon, and are usually based on the evaluation of the response of the investigated surface to a variation in thermal boundary conditions (e.g. variation in air temperature). Some experimental features are common to all transient techniques. To initiate a transient heat transfer process, at the beginning of the test a temperature difference is created between the test article (which in most cases is kept at a uniform initial temperature) and the flow. This can be done by using switching valves, which allow preheated or precooled air to enter the test article [78, 79],

or directly preheating or precooling the test article and flowing ambient temperature air into the rig at the beginning of the test [80]. However, by applying these methods a variation in the flow conditions occurs at the beginning of the test, whose effect often needs to be considered. To avoid this issue, a technique has been proposed by Wang at al. [81], which allows to quickly change the temperature of an already established flow. In this case, air passes through one or more electrically heated fine wire meshes installed at the rig inlet section, which are powered up in order to start the test. Moreover, the low thermal inertia of the heater allows to obtain a temperature variation close to an ideal step. The obtained temperature difference and subsequent transient phenomenon can be exploited using different techniques.

The most commonly employed transient heat transfer methods are the lumped capacitance and the semi-infinite wall techniques, which mainly differ for the thermal properties of the heat transfer surface. In particular, the *lumped capacitance* method is based upon the transient thermal response of high conductivity samples: as so, it can be employed for complex and hardly accessible surfaces but completely neglects the local variation of heat transfer over the investigated wall. As a consequence, one of the most common applications of the lumped technique is the investigation on the thermal performance of protrusions, which allows to combine it with other transient techniques in order to obtain a complete coverage of all heat transfer surfaces (see as an example Facchini et al. [82]). The local heat transfer features of complex geometries can be studied using the *semi-infinite wall* method, which was actually developed for this purpose. Given the importance of such technique for the present work, the next section will be entirely dedicated to presenting its underlying hypotheses, features and possible implementations.

## 2.2 Semi-infinite wall transient technique

In this work, the semi-infinite wall transient technique was employed for heat transfer evaluation. As a consequence, in the present section

the general principles of this technique will be presented, as well as the particular implementation developed for this study in order to deal with rotation related issues.

### 2.2.1 Technique theory and application

The semi-infinite wall transient technique is based upon the study of the response of a low conducting wall when one of its sides is exposed to a sudden temperature variation. The low thermal conduction often allows to neglect the lateral conduction effects, so that the thermal evolution can be approximated as one-dimensional across the material thickness. Moreover, if the thickness value is sufficient the temperature variation inside the solid does not reach the opposite side of the wall: as a consequence, the wall itself can be considered as *semi-infinite*. These useful assumptions allow to simplify the study of transient heat transfer inside the solid, a scheme of which is reported in Figure 2.2. If $z$ is the normal wall coordinate, the one-dimensional assumption allows to express the transient local energy balance as follows:

$$\frac{\partial T_s}{\partial t} = a_s \frac{\partial^2 T_s}{\partial z^2} \tag{2.1}$$

where $T_s$ is the local wall temperature and $a_s$ is the material thermal diffusivity. If also the semi-infinite wall hypothesis is valid, the material is at a initial uniform temperature $T_i$ and at time $t = 0$ a side of it is exposed

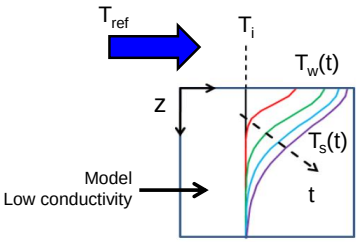


*Figure 2.2: Scheme of the transient temperature evolution inside a semi-infinite solid.*

to an air flow of temperature $T_{ref} \neq T_i$, the corresponding boundary conditions can be defined for Equation 2.1:

$$T_s(\infty, t) = T_i \tag{2.2}$$

$$T_s(z, 0) = T_i \tag{2.3}$$

$$-\lambda_s \left.\frac{\partial T_s}{\partial z}\right|_{z=0} = h\left(T_{ref} - T_s(0,t)\right) \tag{2.4}$$

If the local heat transfer coefficient $h$ can be considered as time independent, it can be demonstrated [83] that the analytical solution of Equation 2.1 with the previous boundary conditions is given by:

$$\frac{T_s(z,t) - T_i}{T_{ref} - T_i} = erfc\left(\frac{z}{2\sqrt{a_s t}}\right) - exp\left(\frac{a_s z}{\lambda_s} + \frac{h^2 a_s t}{\lambda_s^2}\right) erfc\left(\frac{z}{2\sqrt{a_s t}} + \frac{h\sqrt{a_s t}}{\lambda_s}\right) \tag{2.5}$$

where $erfc$ is the complementary error function, defined by:

$$erfc(x) = \frac{2}{\sqrt{\pi}} \int_x^\infty exp(-r^2) dr \tag{2.6}$$

At the wall location ($z = 0$, $T_s(0,t) = T_w(t)$) the previous expression reduces to:

$$\frac{T_w(t) - T_i}{T_{ref} - T_i} = 1 - exp\left(h^2 \frac{t}{\rho_s c_s \lambda_s}\right) erfc\left(h\sqrt{\frac{t}{\rho_s c_s \lambda_s}}\right) \tag{2.7}$$

The value of $h$ can be determined from the previous equation if a precise value of surface temperature $T_w$ (*event temperature*) is known at a given time $t$ (*event time*): as a consequence, it is possible to evaluate heat transfer from the occurrence of a single thermal event. Such feature makes this technique particularly suitable to the use of narrow band temperature sensitive coatings (e.g. thermochromic liquid crystals), which grant high accuracy in the determination of a small range of temperatures.
This technique can be employed to evaluate local heat transfer on every surface of a cooling system. However, in order to obtain reliable information, the assumptions and the hypothesis of the method need to be verified, and if they are not fully satisfied additional effects must be

considered. The first and most common condition is the non ideal shape of air temperature step. In this case, the approach firstly introduced by Metzger and Larson [84] can be employed: the actual temperature history is approximated as a series of $N$ ideal temperature steps, and Duhamel's superposition principle is employed in order to determine an approximated solution in the form:

$$T_w(t) - T_i = \sum_{i=1}^{N} \left[ 1 - exp\left( h^2 \frac{t - t_i}{\rho_s c_s \lambda_s} \right) erfc\left( h \sqrt{\frac{t - t_i}{\rho_s c_s \lambda_s}} \right) \right] \Delta T_{ref(i,i-1)} \tag{2.8}$$

where $t_i$ is the discrete time of each step and $\Delta T_{ref(i,i-1)}$ is the corresponding air temperature variation.

In order to apply such technique, the semi-infinite wall hypothesis needs to be verified. Intuitively, such condition deals with the finite thickness of the walls, which is a design parameter of the test article and is often limited by various constraints (e.g. model mass). The effect of finite wall thickness was firstly studied by Schultz and Jones [83]: they showed that temperature variation and heat flux at a depth $l$ are less than 1% of the corresponding surface values if the measurement time $t$ satisfies the condition:

$$\frac{t a_s}{l^2} \leq \frac{1}{16} \tag{2.9}$$

As a consequence, if the wall thickness $d$ is given this criterion provides a maximum allowable duration for the transient test. A more relaxed criterion was proposed by Vogel and Weigand [85] for a wall with adiabatic back side: they showed that as long as

$$\frac{t a_s}{l^2} \leq \frac{1}{4} \tag{2.10}$$

the error introduced by the use of solution for an ideal semi-infinite wall is lower than 3%.

Surface curvature is an additional aspect to be taken into account. The previous equations have all been determined for a flat wall, but many features of different gas turbine cooling geometries present surfaces with a strong curvature (e.g. leading edge cavity or U-bends between radial

ducts). In this case, different approaches can be applied: an approximate solution of the transient conduction problem for a cylindrical surface is provided by Buttsworth and Jones [86], which provides an accuracy within 5% in a wide range of conditions [87]. When complex geometries are involved, however, higher level numerical solutions are required in order to resolve the transient heat transfer inside the solid, e.g. finite difference methods [88].
Lateral conduction is usually neglected in this technique: thanks to the high temperature difference between wall and fluid, temperature gradients in lateral directions are often much smaller than in the wall normal direction. The relatively short measurement times are also positive in terms of reduction of lateral conduction influence. In order for these consideration to be valid, the test needs to be sufficiently quick, which can be obtained by employing an event temperature close to the initial one for data reduction. The tradeoff between this requirement and considerations on measurement accuracy suggests to choose an event temperature $T_w$ which provides values for the dimensionless temperature difference (first term of Equation 2.7) within the range [20]:

$$0.3 < \frac{T_w - T_i}{T_{ref} - T_i} < 0.7 \tag{2.11}$$

As a concluding remark, the main advantage of the semi-infinite wall method is essentially the possibility of studying complex geometries with a high attainable spatial resolution, which makes the choice of this technique almost unavoidable for a wide range of analyses, including the present one. On the other hand, a heavier postprocessing is required with respect to other techniques, and test conditions must be accurately controlled in order to verify the underlying hypotheses of the method.

### 2.2.2 Cold step technique

For the present study, in order to obtain detailed heat transfer information on the complex investigated geometries which will be described in Section 3.1 the semi-infinite wall transient technique was selected. How-

ever, performing measurements in rotating conditions requires that the same thermal boundary conditions of the real component are replicated, in order to obtain the correct sign of buoyancy forces: as a consequence, during the test the temperature of the test article walls needs to be higher than the air temperature [78, 79]. Moreover, in the present work a relevant part of the tests are performed in rotating conditions: as a consequence, an additional constraint to the implementation of the measurement technique is given by the need of installing all or a part of the required hardware on a rotating structure.

In order to suit transient technique to the present application, a novel implementation had to be developed, which is compliant with the aforementioned requirements and is aimed at the creation of a cold temperature step for the coolant air. A simplified scheme illustrating the principle of the measurement technique is reported in Figure 2.3. A model of the cooling geometry is installed onto a rotating chassis, and is connected to inlet and outlet pneumatic lines. In the present case, air circulation is obtained through a vacuum system located downstream the rig. Before the test, the correct flow conditions are set by circulating the whole nominal mass flow rate at ambient temperature. The model is then preheated, which is obtained by increasing the air temperature thanks to a heater located upstream the geometry. However, heating up the whole nominal mass flow rate, which can be as high as 340 $g/s$, would have required a heater whose dimensions and weight were not compatible with a rotating installation. In order to reduce the required thermal power, the air mass flow rate employed for the model heating is smaller than the design one, which is obtained by opening a fast actuation bypass valve located close to the rig outlet. When uniform and steady thermal conditions are reached for the model, the test is initiated by activating a trigger, which closes the bypass valve and simultaneously shuts down the heater: in this way, the whole nominal mass flow rate at ambient temperature enters the model, thus obtaining the desired cold temperature step.

The proposed technique allows to obtain the correct sign of buoyancy forces by using a compact and low power heater. In this particular case,

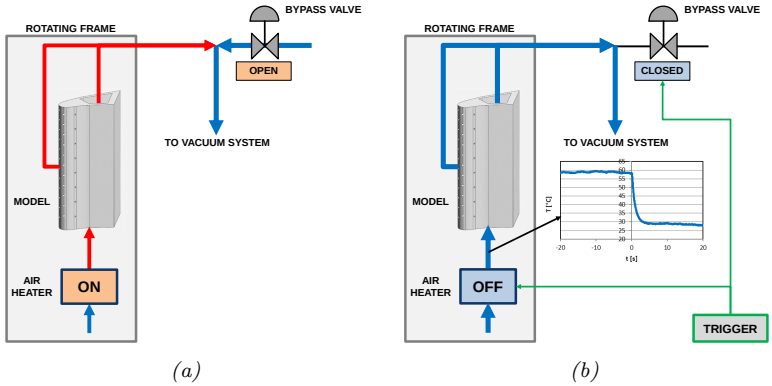


*Figure 2.3: Scheme of the cold step transient technique: heating (a) and test (b) phases.*

the technique allows to set test parameter values corresponding to a wall-to-coolant density ratio (defined by Equation 1.3) of around 0.10, which is compliant with the values employed in many works dealing with buoyancy effects on heat transfer [7, 17]. In this condition, a maximum value of Buoyancy parameter $Bo$ (defined by Equation 1.3) for the impingement jets of around 0.0003 is obtained: as a consequence, it can be expected that the direct buoyancy effect on impingement is negligible. This is also expected to be verified in the real engine system, given the high jet velocity and thus the small relative weight of buoyancy with respect to inertia. On the other hand, since in this case the whole cold bridge type system is replicated, it is worth evaluating the buoyancy parameter also for different features of the system. In particular the supply channel needs to be considered, since density driven effects may actually alter the jet supply condition. For the investigated test parameters, the maximum value of $Bo$ calculated for the supply channel is around 0.05 (corresponding to minimum Reynolds number, maximum Rotation number and minimum crossflow, i.e. tip conditions). A similar value fits within the ranges of this parameter investigated in dedicated studies on the buoyancy effects on flow field [21] and heat transfer [17], and is expected to be representative

of the phenomena actually occurring in a radial outward channel [89]. As a consequence it can be expected that, even if the investigated geometry was not explicitly scaled in order to replicate the engine buoyancy parameters (see Section 3.1), it is still able to provide engine representative phenomena when the effect of buoyancy is significant.
Moving away from the particular investigated case, this technique could also be applied in order to perform dedicated investigations on the buoyancy effect: in fact, altering the model initial temperature allows to easily vary the density ratio $DR$ and thus the Buoyancy parameter $Bo$. The limits for these parameters are imposed by the thermal resistance of the test article and, in the present case, by the thermochromic liquid crystal event, which however can be chosen a priori in order to suit the desired test conditions.
The technique presented in this section, despite being based upon the standard theory of the semi-infinite wall transient method, presents some critical aspects which need to be discussed. First of all, the closure of the bypass valve which initiates the nominal flow requires a finite time, during which the mass flow increases: as a consequence, different flow conditions can actually occur at the beginning of the test. To avoid this issue, the closure time has to be evaluated and needs to be as low as possible. Moreover, the valve is located downstream the actual test section, which also requires to consider the actual time employed by the flow perturbation to reach the test article. Both these aspects were quantified in the present case and found to be satisfactory in the framework of the investigation (see Section 3.2.4): even so, in order to verify if these phenomena are able to alter the results in a significant way a validation of the technique was carried out, which will be presented in the following section.

#### 2.2.2.1 Technique validation

Before actually applying the experimental technique to the present case, its reliability was assessed by performing a preliminary validation. In particular, for the present case the validation is aimed at replicating all the critical aspects of the technique (e.g. the surface heating and cooling

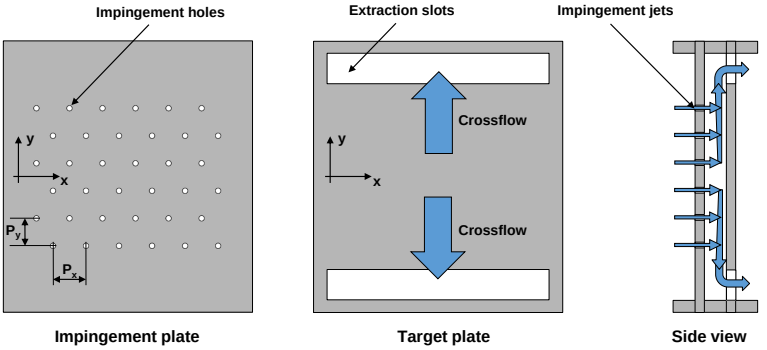


*Figure 2.4: Scheme of the validation geometry.*

cycle and the switching times between the preheating and test phases), in order to assess if they are actually able to alter the heat transfer results. To achieve this goal, a simple impingement array geometry with a flat target wall was investigated, with the aim to compare the obtained output with the data available in the open literature. The validation geometry consists of an impingement hole array composed of 6 rows of 6 holes each and is designed in order to obtain a staggered arrangement for the holes. Hole diameter is equal to 7 *mm*. Hole-to-hole spacing in the same row is equal to 6 diameters, row-to-row spacing is equal to 5 diameters and jet-to-target plate spacing is equal to 2.8 diameters. According to these values, the geometry fits within the validity ranges of the correlation developed by Florschuetz et al. [31], which can thus be used in order to validate the results. A scheme of the validation geometry is reported in Figure 2.4.

In order to perform heat transfer measurements on such geometry, a part of the experimental setup employed by Andreini et al. [36] was exploited. The coolant flow enters the impingement geometry by means of an electric heater, which is built using the same heating elements and design solutions of the one actually employed in the rotating test rig (which will be described in Section 3.2.3). The cooling geometry, which

is entirely made of transparent PMMA, is closed from all the four sides. Spent coolant flow is extracted by the impingement cavity through two slots symmetrically located at the opposite sides of the target surface: as a consequence, a symmetric flow field is created, which can be interpreted as generated by two independent hole arrays made of 3 rows each. It is also expected that the spent coolant flow will generate a transverse flow for the downstream impingement jets (downstream crossflow), thus altering the heat transfer pattern. The flow is finally collected into an extraction plenum, which also acts as an optical window to observe the side of the target wall opposite to the jets. In order to apply the transient heat transfer technique presented above, the jet target surface is painted with narrow band thermochromic liquid crystals of the same lot employed and calibrated for the rotating measurements. Care was taken to employ the exact experimental setup as the rotating test rig, including bypass and trigger system, temperature, pressure and mass flow rate measurement devices, image acquisition system and illumination arrangement, which will be described in Chapter 3. To apply the cold step transient technique, before the test the heat transfer surface was heated for around 90 minutes at a temperature of approximately $55°C$, and then cooled down with ambient temperature air to allow the transient heat transfer phenomenon to occur. In order to increase the significance of the validation, the duration and target temperature of the heating phase are also similar to the ones of the rotating test rig, as well as the heating and test mass flow rates.

A single test condition was investigated, corresponding to a jet Reynolds number value of around 15000. The result of such test, expressed as spatially resolved Nusselt number distribution, is reported in Figure 2.5a, while in Figure 2.5b the area averaged values for the different rows are compared with the outcomes of Florschuetz et al. [31] correlation. Given the expected flow field, area averaged values are calculated as the arithmetic average of the values of each couple of symmetric rows. The heat transfer distribution presents the typical phenomena of an impingement array system: the pattern reflects the holes arrangement,

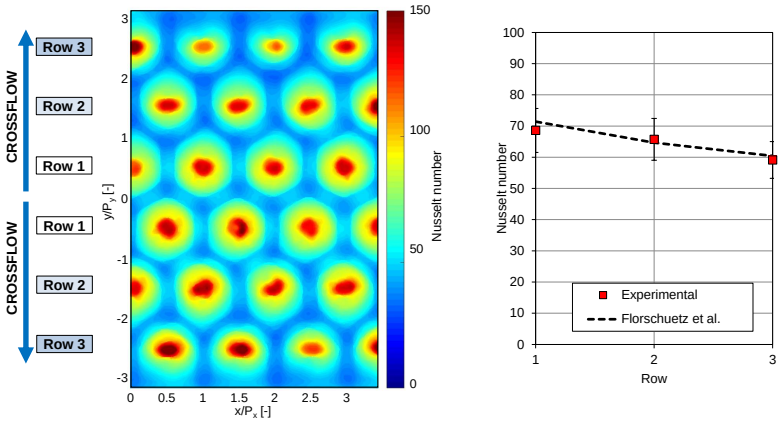


*(a)* *(b)*

*Figure 2.5: Spatially resolved $Nu$ distribution (a) and comparison with Florschuetz et al. [31] correlation (b).*

with a single heat transfer peak for each jet close to the ideal stagnation point. The interaction of the wall jet flow also generates a tessellation of the Nusselt number distribution. Low heat transfer regions are present in between the jets, which can be attributed to the onset of the so-called fountain effect [35]. The typical effects of crossflow can also be appreciated: moving towards the coolant exit, the shape of the heat transfer peaks elongates in the horizontal direction, and a decrease in averaged heat transfer entity can be observed.

If the comparison with the correlation outcome is considered, a reasonable agreement is obtained, since in every location discrepancies between measured and predicted values lie within $\pm 5\%$, which is lower than the experimental uncertainty. As a consequence, the experimental setup and technique can be considered as validated.

## 2.3 Liquid crystal thermography

The presentation of the different experimental methods performed in section 2.1 reveals that, in order to obtain space resolved heat transfer coefficient distributions, a point-by-point temperature measurement is required, which is usually performed by means of optical measurements. In particular, one of the most widely applied methods consists in the use of thermochromic liquid crystals (TLCs), i.e. of substances whose chromatic properties are related to their temperature. In many applications, TLCs are preferred to other optical techniques (e.g. IR thermography or TSP) given their relative ease of installation and employment, rapid response time, high spatial resolution and flexibility and small cost of data acquisition hardware. Given these considerations, TLCs were chosen as surface temperature measurement device for the present investigation. The main features of TLCs will be presented in this section, with a particular attention to the aspects related to their application for heat transfer measurement.

### 2.3.1 TLC characteristics

The therm liquid crystal (LC) is employed to identify an intermediate phase of matter (*mesophase*) between crystalline solid and liquid, which is presented by a range of complex organic substances [90]. As so, they present properties of both the adjacent phases, i.e. the optical properties of crystals and the fluidity of liquids. In particular, their chromatic properties derive from their molecular structure and arrangement. The LC molecules (*mesogens*) have an elongated and cigar-like shape [91] and present different arrangements as temperature increases, which allow to classify the corresponding mesophase as *smectic*, *nematic* or *chiral-nematic* (also called *cholesteric*). Just above the crystal melting point the smectic mesophase is present, where the molecules have both high positional and orientational order, being packed in a systematic pattern with their axes all parallel. As temperature increases, the positional order is lost, while orientational order is kept: in this case, the molecular axes can have

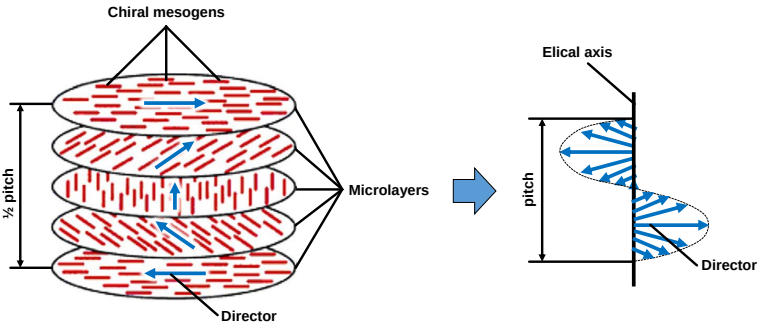


*Figure 2.6: Scheme of a chiral-nematic LC molecular structure [90]*

the same orientation for the whole phase (nematic) or for single parallel microlayers (chriral-nematic). In the latter case, the intermolecular forces cause each microlayer to be twisted at a certain angle with respect to the adjacent ones, forming a continuous helical structure (see Figure 2.6). If the helical axis is aligned with the incident light (i.e. the LC presents the so-called planar texture) the helix is able to interact with the incident light, providing selective light reflection according to the Bragg's law. The actual thermochromic properties of chiral nematic LC is given by the thermal motion of the molecules, which cause the displacement angle between adjacent microlayers to increase with temperature: as a consequence, the helical pitch decreases and so does the reflected wavelength of the incident light. According to this phenomenon, the whole spectrum of visible light will be selectively reflected by chiral-nematic LC, and so their color will pass from red to green to blue as temperature increases, as illustrated in Figure 2.7. The temperature interval in which this phenomenon occurs is named *colour play interval* or *activation bandwidth*: its lower limit defines the so-called *activation temperature*, and its upper limit the *clearing point temperature*. If the LC is heated above the nematic or chiral-nematic phase, the transition to isotropic liquid occurs. Amongst all the LC phases, only the chiral-nematic one is optically active and can interact with the incident light: as a consequence, outside the colour play range

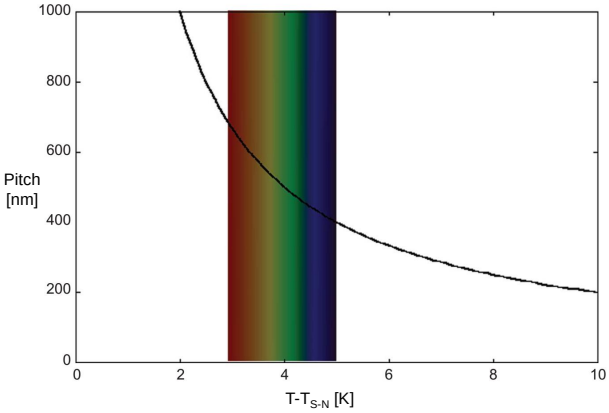


*Figure 2.7: Illustrative change in helix pitch and reflected wavelength as a function of temperature above the smectic-nematic transition [92]*

the LC appears as transparent. An extensive discussion on LC optical properties can be found in reference [91].
The colour play interval is different for different kind of TLC formulations and allows to classify them as *narrow band* (0.5-4$^{\circ}C$ activation bandwidth) or *wide band* (5-30$^{\circ}C$ activation bandwidth). Activation temperatures for commercially available products range from -30$^{\circ}C$ to 115$^{\circ}C$ [91].
An additional distinction between TLCs can be made according to the actual substance they are composed of: proper Cholesteric Liquid Crystals (CLCs) are derived from cholesterol esters, while TLCs derived from non sterol chemicals (like phenyl-benzoate esters) take the generic name of Chiral Nematic Liquid Crystals (CNLCs) [90].

### 2.3.2 Use of TLC for quantitative measurements

The features briefly presented in Section 2.3.1 indicate that TLCs are an attractive tool to obtain surface temperature information for a wide range of applications. However, in order to employ them as an actual temperature measurement device it is fundamental that the colour-

temperature response is defined in a precise and robust way. This is achieved by correctly choosing and applying the TLC and the color parameter to be put in relation with the temperature, by performing a suitable calibration and by taking into account those effects which may alter the colour-temperature response. These aspects will be briefly discussed in the present section.

#### 2.3.2.1 TLC choice and application

TLCs are commercially available in several formats, the most common ones being pure TLCs and microencapsulated TLCs. Pure TLCs allow to obtain sub-micron resolution and a brilliant colour play, but require special handling since they are highly susceptible to degradation, mainly from ultraviolet (UV) radiation and chemicals: as a consequence, pure TLCs are not suitable for general application. Microencapsulated TLCs are basically TLCs encased within spherical polymer capsules with diameters varying between 10 and 15 $\mu m$. The microencapsulation process protects TLCs from the environment, and thus allows to obtain product which is chemically more stable and less prone to degradation: as a consequence, it is preferable to employ microencapsulated TLCs in most of applications. Microencapsulated TLCs are usually available as aqueous slurries, which can be mixed with water and binder material in order to obtain a sprayable coating: in this way, TLCs can be applied to models with complex geometries. Microencapsulated TLCs are also available as pre-manufactured sheets, where a thin layer of TLC coating is applied to a polyester sheet: this solution allows to easily install and remove the temperature sensitive coating, but the application is limited to flat or single curvature surfaces.
The choice of the most suitable TLC formulation to be employed strongly depends upon the thermal conditions of the phenomenon to be investigated and to the chosen measurement technique. As an example, if the thin foil steady-state technique (see Section 2.1) is employed, the knowledge of local wall temperature is required in all or a significant part of the heat transfer surface: as a consequence, wide band TLC formulations

are suitable for this application. On the other hand, if the single event implementation of the semi-infinite wall method is employed (see Section 2.2) only the occurrence of a single temperature value is required, which then needs to be known with the highest possible accuracy. This goal is usually achieved by using narrow band TLCs, which provide lower uncertainty given the small colour play range. The output of narrow band TLCs also appear to be less influenced by viewing and illumination disturbances, resulting in a more robust measurement. In particular, Kakade et al. [93] reported negligible effects of viewing and illumination angles in the red and green regions of the colour-temperature curve for angles between 0° and 40°, while Abu Talib [94] showed no significant influence in TLC calibration due to a change in illumination intensity. Despite these advantages, the application of narrow band TLCs is limited by their small bandwidth.

The use of TLC paints in transient heat transfer techniques also requires that the response time of such substances is taken into account. The response time of TLCs appear to depend upon their chemical composition, where chiral nematic LCs generally have faster response times than cholesterics LCs [90]: in particular, Ireland and Jones [95] demonstrated that the response time of a microencapsulated CNLC film with 10 $\mu m$ thickness is 0.003 $s$. As a consequence, it can be stated that CNLCs are more suitable than CLCs for transient heat transfer measurements, and that the response times of the first are short enough to be neglected in most of the cases.

In order to improve the chromatic response of TLCs, a non reflecting background (usually black) shall be provided to the paint: in this way, the non reflected wavelengths are absorbed by the background and the surface color actually corresponds to the sole TLC response.

#### 2.3.2.2 Colour descriptors

TLCs can be employed as measurement devices if their colour can be associated with a corresponding temperature value in a non ambiguous way. To do so, a quantitative definition of colour has to be provided.

Consistently with the three-chromatic nature of human vision, digital image acquisition systems record the chromatic information of each pixel as red (R), green (G) and blue (B) colour intensities: as a consequence, three parameters are needed in order to rebuild the colour, and eventually the temperature, of a given point. Moreover, this description includes the effects of color brightness and saturation, and thus is not suitable to be employed in systems not showing constant and ideal optical conditions. To overcome this issue, more robust and computationally efficient color descriptors have been defined and applied. In particular, the HSI (Hue-Saturation-Intensity) colour space allows to describe colour in a more intuitive way: hue is a parameter which represents the actual color shade, saturation describes the colour purity (ranging from vibrant and pure to mute and gray), while intensity identifies the colour brightness. According to such definitions, it is evident that hue is associated with the dominant reflected wavelength of the object: as a consequence, when a TLC is considered hue is the most significant parameter to be associated with the temperature value. For such reason, hue-temperature representations are the most common colour-temperature representations for TLCs and have been widely used by researchers due to their simplicity and independence with respect to illumination intensity [96]. Hue parameter can be derived from 0-to-1 red, green and blue colour intensities using the relation:

$$H = tan^{-1}\left[\frac{\sqrt{3}(R-G)}{2R-G-B}\right] \tag{2.12}$$

which thus embodies a computationally expedient and reliable way to obtain such parameter directly from the digital acquisitions of TLC surface.

Hue-temperature representation is usually employed when a full surface temperature description is required. On the other hand, if the thermal evolution of a phenomenon has to be recorded, the elapsed time before a particular temperature is reached is often the only required information (see Section 2.2): in this case, the target temperature can be defined as the value associated with the peak of a given monochromatic intensity

(usually red or green) in TLC response, thus defining a simple and robust color descriptor. This kind of measurements is usually performed using narrow band TLCs, given their superior precision.

#### 2.3.2.3 Calibration

In order to use a particular sensor, the relationship linking the input to the output needs to be known. In the case of TLCs, this consists in the determination of the colour-temperature response, i.e. associating the values of the chosen colour descriptor with the corresponding temperature values. In general terms, TLCs calibration is performed by applying TLCs on a temperature controlled surface, which is equipped with one or more point temperature sensors (e.g. thermocouples) and a heating and/or cooling system. The surface temperature is then regulated in order to reach a series of desired values, and the colour change of TLCs is observed by means of a suitable illumination system and recorded by a video acquisition system. The different surface temperature levels can be obtained one at a time, if the surface is designed to be isothermal [97], or all together, if the surface allows to set a well defined temperature gradient [98]. Transient calibration is also possible, when the surface temperature varies in time and TLC images are captured during the heating or cooling process [94]. A complete discussion of different calibration approaches can be found in reference [90].

#### 2.3.2.4 Hysteresis

The behaviour of TLCs is characterized by thermal hysteresis, since their chromatic response is different when cooled rather than heated. In particular, for TLCs hysteresis seems to occur when they are heated above their clearing point temperature [99] and generally results in a decrease in color intensities (i.e. colors appear darker) and a bias in hue-temperature curve towards lower temperatures. Hysteresis effects seem to intensify as the maximum TLC temperature prior to cooling increases [100]. This phenomenon has been attributed to the loss of alignment between the incident light and the helical TLC molecular structures when the crystal

is cooled down from the isotropic liquid phase, which thus reduces the light reflection [100]. Hysteresis effects cease if the TLCs are cooled down below their activation temperature. Given these considerations, hysteresis effects need to be taken into account whenever a TLC coating is employed during a complete heating and cooling thermal cycle. In particular, if heat transfer measurements are carried out using transient techniques, it is recommended that the transient is initiated from the same direction (heating or cooling) and, if possible, from the same initial temperatures as those used for calibrations [100].

#### 2.3.2.5 Aging

Aging is a phenomenon whereby the TLCs exhibit a different behaviour due to prolonged use [90]. Due to TLC aging, the results obtained after repeated heating and cooling cycles may not be coherent with the initially determined calibration curve, thus providing non reliable information. As a general indication of different works focused on this subjects (e.g. [93, 97]) it can be stated that aging effects on TLCs comport a gradual decrease in magnitude of red, green and blue intensities, as well as a shift towards higher temperatures at which a given hue value occurs. These works also show that aging effects are reduced if a higher TLC film thickness is employed: as a consequence, a thick film thickness (higher than 40 $\mu m$) is recommended in order to preserve the colour-temperature response with time. Even so, the film thickness shall not be high enough to provide a milky appearance for the coating or large temperature gradients across it [90]. The employed film thickness shall be a tradeoff between these competing requirements.

# Chapter 3

# Experimental analysis

As illustrated in Chapter 1, gas turbine cooling systems usually involve different complex fluid and thermal phenomena, whose understanding is further compounded by their interaction. As a consequence, direct observation is often the only viable tool in order to obtain reliable information about the performance of such systems. Following this consideration, an experimental analysis of the system investigated in the present work was carried out, with the aim to study the heat transfer phenomena and their interaction with the different features of the cooling geometry.
In the present chapter, the details of the investigated geometries will be described, as well as the test conditions selected for the analysis. Subsequently the experimental apparatus and procedure employed for such investigation will be presented, followed by a discussion on the postprocessing tools applied to the raw data in order to obtain the final results.

## 3.1 Investigated geometries and test conditions

The system investigated in the present work represents a scaled up leading edge impingement cooling scheme, which exploits the impact of multiple air jets in order to remove heat from the blade inner side. The geometry replicates a radial section of the actual blade front region, and

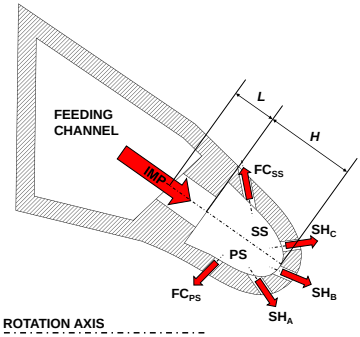


*Figure 3.1: Cross-section of the investigated geometry.*

was designed in order to mimic all the features of a realistic system, the only simplification being the constant cross-section in the radial direction. A sectional view of the investigated system is reported in Figure 3.1. A radial feeding channel provides coolant air to a series of square edged cylindrical holes, located on the side of the channel facing the leading edge. Such holes generate an array of jets, which impinge on the leading edge inner surface and thus perform the cooling action. Since the coolant is supplied to the jets directly from the blade hub without significant heat pickup along the feeding channel, this design is denoted as cold bridge [101]. Given the camber line shape of a typical high pressure blade, the leading edge is directed towards the blade pressure side, and so are the impingement jets: in particular, the jet axis is inclined of 35.6° in this direction. The spent coolant flow is extracted by the impingement cavity by means of five rows of extraction holes, the three central ones representing a showerhead (SH) system and the side ones a film cooling (FC) system. The holes of every row are aligned in the radial direction, and the axis of each hole lies on a tangential plane. The features of the different extraction holes are reported in Table 3.1.

In this work, three different impingement hole arrays were studied, in order to highlight the effects of different coolant mass flow distributions

*Table 3.1: Extraction holes geometric features.*

| Extraction row | | $FC_{PS}$ | $SH_A$ | $SH_B$ | $SH_C$ | $FC_{SS}$ |
|---|---|---|---|---|---|---|
| Holes number | $N_{ext}$ [-] | 8 | 11 | 12 | 11 | 10 |
| Hole diameter | $D_{ext}$ $[mm]$ | 4.8 | 5.6 | 5.6 | 5.6 | 5.6 |
| Radial pitch | $P_{z,ext}$ $[mm]$ | 48.6 | 33.9 | 32.6 | 33.4 | 37.7 |

inside the leading edge cavity. In fact, the three investigated geometries present different holes arrangements, numbers and diameters but have the same overall passage area: this allows to emphasize the outcomes of different flow patterns with similar average jet velocities and coolant consumption. The three geometries are denoted as GTE-A, GTE-B and GTE-C respectively. In particular, GTE-A geometry presents seven round impingement holes, aligned in the radial direction and equally spaced, located along the centerline of the impingement plate. The diameter of all holes is 20 $mm$. GTE-B presents the same hole number, diameter and radial distribution of holes with respect to GTE-A, but in this case the holes are aligned along two parallel lines in the radial direction, one closer to the pressure side (PS) and one to the suction side (SS), resulting in a staggered arrangement. Finally, GTE-C hosts twice the number of holes with respect to GTE-A and GTE-B, but with a smaller diameter (14.14 $mm$) in order to have the same total passage area of the previous geometries. Like GTE-B, also GTE-C presents a staggered arrangement for the impingement holes. A scheme of the three investigated geometries is represented in Figure 3.2, while their main geometric features are reported in Table 3.2.

The aim of this work is to replicate the phenomena occurring in the real cooling devices: as a consequence, test conditions were defined in order to obtain realistic values of the main dimensionless parameters characterizing the actual systems. The similitude in terms of flow phenomena was achieved by replicating the value of jet Reynolds number, defined as:

$$Re_j = \frac{\dot{m}_{IMP} D_j}{A_{IMP} \mu} = \frac{\dot{m}_{IMP} D_j}{N_j A_j \mu} \tag{3.1}$$

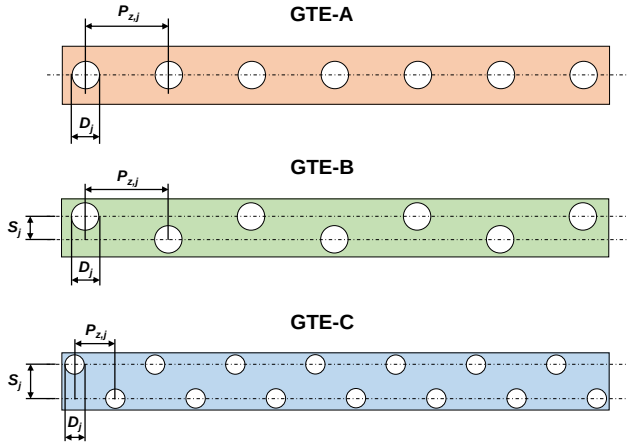


*Figure 3.2: Front view of the three impingement geometries.*

where $\dot{m}_{IMP}$ and $A_{IMP}$ are the overall impingement mass flow rate and passage area respectively, $A_j$ is the impingement hole cross-section area and $\mu$ is air dynamic viscosity, evaluated using the time averaged air temperature during the test. For each geometry, four equally spaced values of jet Reynolds number were investigated: in particular, $Re_j$ values ranging from 20000 to 50000 were tested for GTE-A and GTE-B geometries, while for GTE-C values ranging from 12500 to 35000 were replicated. Despite the different ranges, the mass flow rates corresponding to the single four $Re_j$ values are similar for the three geometries, thus allowing to significantly compare their performance at a given coolant consumption rate. To achieve this goal, the equivalent width of a 2D slot $b$ can be chosen as characteristic length, defined as:

$$b = \frac{A_{IMP}}{Z_{max}} \tag{3.2}$$

where $Z_{max}$ is the total radial extension of the heat transfer surface. Since the three geometries share the same overall passage area, the same value

of $b$ is obtained, equal to 5.86 $mm$. A different definition of Reynolds number can thus be obtained using $b$:

$$Re_b = \frac{\dot{m}_{IMP} b}{A_{IMP} \mu} \tag{3.3}$$

Such parameter is indicative of the actual coolant consumption and can thus be employed in order to directly compare the different geometries. In the present case, overall impingement mass flow rates ranging from $40\,g/s$ to $100\,g/s$ were employed.
The similitude in terms of rotational effects is obtained by replicating the Rotation number, defined as:

$$Ro_j = \frac{\omega D_j \rho A_{IMP}}{\dot{m}_{IMP}} \tag{3.4}$$

where $\omega$ is the rotational speed and $\rho$ is air density. For all the geometries and every $Re_j$ value tests were performed in static and rotating conditions, the latter ones corresponding to a fixed value of $Ro_j$ of 0.008 for GTE-A and GTE-B and of 0.006 for GTE-C. Also these values were chosen in order to allow a direct comparison between the different geometries: in fact, with the investigated $Ro_j$ values the rotational speeds corresponding to a given coolant mass flow rate are similar for all the geometries, given the different hole diameters. In order to better relate the rotational effects to the actual coolant consumption, Rotation number can also be redefined

*Table 3.2: Impingement plates geometric features.*

| **Geometry** | | **GTE-A** | **GTE-B** | | **GTE-C** | |
|---|---|---|---|---|---|---|
| | | | PS row | SS row | PS row | SS row |
| Jet number | $N_j$ [-] | 7 | 3 | 4 | 7 | 7 |
| Jet diameter | $D_j$ [mm] | 20.0 | 20.0 | 20.0 | 14.14 | 14.14 |
| Radial spacing | $P_{z,j}$ [mm] | 58.6 | 58.6 | | 28.3 | |
| | $P_{z,j}/D_j$ [-] | 2.96 | 2.96 | | 2.00 | |
| Tangential spacing | $S_j$ [mm] | - | 16.0 | | 24.0 | |
| | $S_j/D_j$ [-] | - | 0.8 | | 1.70 | |
| Jet-to-target distance | $H$ [mm] | 50.0 | 48.1 | 45.7 | 43.3 | 39.5 |
| | $H/D_j$ [-] | 2.5 | 2.41 | 2.29 | 3.06 | 2.79 |

using the equivalent slot width $b$ as characteristic length:

$$Ro_b = \frac{\omega b \rho A_{IMP}}{\dot{m}_{IMP}} \tag{3.5}$$

In this way, the tests performed in rotating conditions correspond to a $Ro_b$ value of around 0.002 for all the geometries. In order to obtain a fixed value of Rotation number for different values of Reynolds number, the rotational speed was varied accordingly: in this way, the maximum rotational speed corresponds to the maximum investigated Reynolds and is equal to 148 $rpm$.

Additional test specifications were defined in order to consider impingement jets supply and extraction conditions. In particular, the behaviour of the jets can be influenced by the flow field upstream the impingement holes, i.e. inside the feeding channel. Moving along the blade span, the mass flow rate of the feeding channel decreases as the coolant is drawn by the impingement holes: if the channel cross section is constant this leads to a reduction in the flow velocity, and thus to different supply conditions for the jets in different sections of the blade. In order to replicate this phenomenon, in the present case a part of the coolant flow does not enter the impingement holes and leaves the feeding channel at its outer radial extremity: in this way, an upstream transverse flow (crossflow) is generated for the impingement jets. In this case, three different crossflow conditions were investigated, corresponding to hub, midspan and tip radial sections of the blade. The three conditions are identified by the value of the crossflow ratio $Cr$, defined as

$$Cr = \frac{\dot{m}_{Cr}}{\dot{m}_{feed}} \tag{3.6}$$

where $\dot{m}_{Cr}$ is the mass flow rate leaving the geometry at the feeding channel outlet and $\dot{m}_{feed}$ is the total coolant amount entering the blade at the hub section. In particular, such parameter was set equal to 10% for the tip conditions, 40% for the midspan conditions and 70% for the hub conditions. A scheme of the crossflow condition is reported in Figure 3.3.

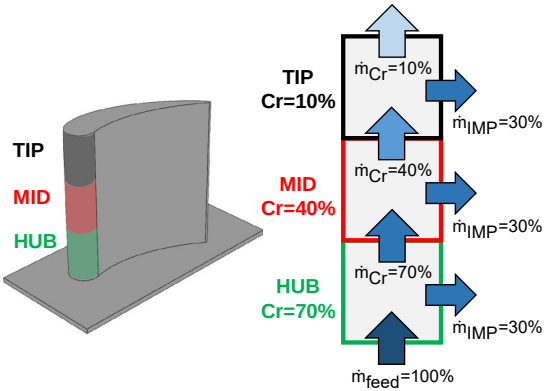


*Figure 3.3: Scheme of the investigated crossflow conditions.*

The effect of extraction condition on the impingement jets was also considered. In particular, the extraction holes discharge the spent coolant on the outer side of the blade, where a non uniform static pressure field is present: as a consequence, non uniform extraction conditions can be expected for the different rows. The mass flow rate through each extraction row was set in order to replicate this effect: in particular, the FC row located on the blade pressure side extracts 10% of the of the total impingement flow $\dot{m}_{IMP}$, the FC row on the suction side 30% of $\dot{m}_{IMP}$ and the three showerhead rows 20% of $\dot{m}_{IMP}$ each. This standard extraction layout was employed in every investigated condition. However, for a limited number of test points two additional configurations were investigated, in order to stress out the effect of extraction condition: in the first one, denoted as *All FC*, the coolant is entirely extracted by the two film cooling rows, while in the second one, denoted as *All SH*, the coolant is solely split between the three showerhead rows. A summary of the investigated extraction conditions is reported in Table 3.3.

*Table 3.3: Extraction holes geometric features.*

| **Extraction row** | $\mathbf{FC_{PS}}$ | $\mathbf{SH_A}$ | $\mathbf{SH_B}$ | $\mathbf{SH_C}$ | $\mathbf{FC_{SS}}$ |
|---|---|---|---|---|---|
| Standard | 10% | 20% | 20% | 20% | 30% |
| All FC | 50% | 0% | 0% | 0% | 50% |
| All SH | 0% | 33.3% | 33.3% | 33.3% | 0% |

## 3.2 Test rig

In order to study the cooling performance of the geometries presented in the previous section, a suitable test rig was developed and installed in the Heat Transfer and Combustion Laboratory of the Industrial Engineering Department of the University of Florence. In this section the main features of the rig will be presented, as well as the design, the characteristics and the interactions of its components.

### 3.2.1 General layout

The test rig employed in the present investigation, a scheme of which is reported in 3.4, consists of a suction type, open loop wind tunnel. The different components of the rig are designed in order replicate the desired flow conditions inside the cooling geometry, to allow the heat transfer phenomenon to occur and to measure all the parameters required for its study.

The rig is mainly composed by a horizontal axis rotating chassis, on which the model of the cooling geometry and part of the flow conditioning and measurement devices are installed. The coolant air enters the model passing through an electric heater, and a part of that enters the impingement holes, evolves into the leading edge cavity and is finally drawn by the extraction holes, while the remaining part passes through the feeding channel and leaves the model at its outer radial extremity. All of the air flows exiting from the model are collected into a central plenum, pass from the rotating to the static environment through a rotary joint and are finally drawn by a vacuum system. In order to ensure laboratory safety,

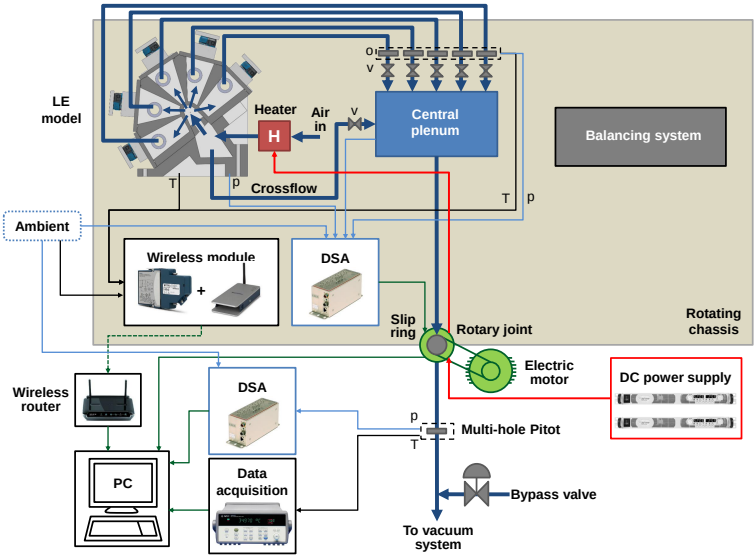


*Figure 3.4: Scheme of the test rig.*

the whole rotating equipment is enclosed in a steel cage. Pressure and temperature measurement systems allow to record such quantities across the whole rig, while the use of a TLC coating and a video acquisition system allow to evaluate the thermal response of the heat transfer surface. The different components of the rig will be presented in detail in the next sections.

### 3.2.2 Test article

The test article is the main part of the test rig, since it replicates the cooling geometry and allows the required measurements to be performed. The model employed in the present work (Figures 3.5 and 3.6) has an overall dimension of $330 \times 333 \times 447\,mm^3$, and is designed in order to replicate the supply channel, the impingement section and the jet target surface of the geometries presented in Section 3.1. The rear and

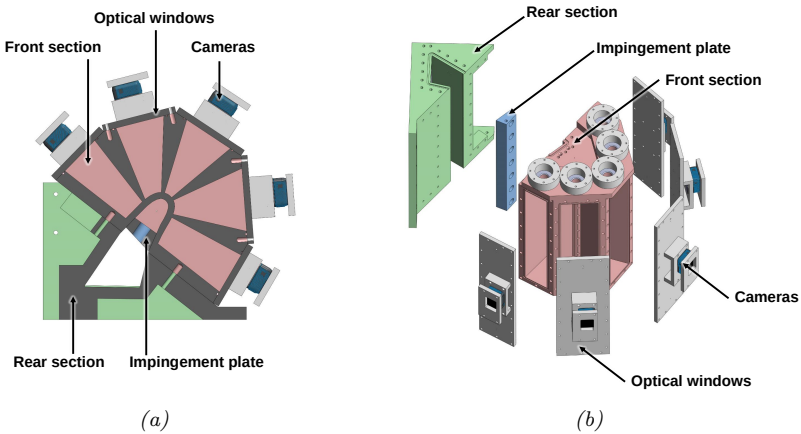


*Figure 3.5: Cross-section (a) and exploded view (b) of the test article.*

side walls of the supply channel are represented by a single component, entirely made of PMMA in order to obtain thermal insulation from the environment. Such component also hosts the holes for the anchor bolts, needed to fasten the test article to the rotating chassis. The impingement

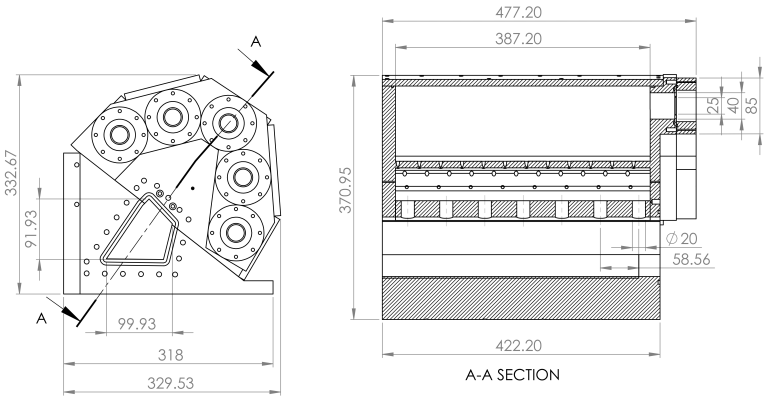


*Figure 3.6: Technical drawing of the test article.*

plate, which separates the supply channel from the LE cavity and houses the impingement holes, is represented by an interchangeable 3D printed polyamide part. Since the three investigated geometries only differ for the impingement holes layout, it is possible to replicate each of them by simply using different impingement plates: as a consequence, three components corresponding to GTE-A, GTE-B and GTE-C respectively were manufactured. The impingement plate is housed into the front section of the test article, which replicates the jet target surface. Such component is made in transparent PMMA, thus allowing both thermal insulation and optical access to the LE inner cavity. The jet target surface, which houses the five rows of extraction holes, has a 10 mm constant thickness: such value was chosen in order to ensure the semi-infinite wall hypothesis of the transient method to be respected (see Section 2.2) while containing the rotating mass. This component also acts as a discharge plenum for the extraction holes, a task which was performed by realizing five chambers on the outer side of the LE surface, each connected to an extraction row. This design presents multiple advantages for the present case:

- In rotating conditions, radial mass flow unbalances across each extraction row are avoided. This is obtained since the inlet and the outlet sections of each extraction hole are located at the same radius, and during rotation equal centrifugal pressure gradients are present inside the LE cavity and the extraction plenums.
- A uniform temperature for the heat transfer surface is obtained at the beginning of the test, since during the heating phase air at the same temperature is present on both sides of the surface itself. This condition is required by the application of transient technique (see Section 2.2).
- A compact design is obtained for the test article.
- The outer surface of each plenum, which is made of a transparent PMMA plate, can be used as an optical window; as a consequence, a camera is installed onto each of such surfaces.

In order to fulfill the last task, the shape and size of the walls dividing the different plenums was accurately set during the design phase so that a complete visibility of the heat transfer surface is obtained using five cameras, one for each plenum. This resulted in a wedge shape for such walls, with a thickness ranging from 5 mm in the inner part (in order to limit the optical obstruction of the heat transfer surface) to 15 mm in the outer part (in order to increase the strength of the test article and allow the connection and sealing of the optical windows).
The different parts of the model are connected together using bolts and screw-thread inserts, while pneumatic sealing in between the different cavities and towards the environment is obtained thanks to either O-rings or silicone glue, according to the size of the surfaces to be sealed.

### 3.2.3 Mesh heater

In order to heat up the air flow, as required by the technique presented in section 2.2.2, an electric heater is installed at the inlet section of the rig. The heater was designed in order to heat up the mass flow employed in the model preheating phase (around 60 $g/s$) up to a temperature of $55-56°C$, while keeping the temperature profile as uniform as possible across its passage section along the whole process. Moreover, a low thermal inertia is required for the heating elements in order to obtain a temperature history which is as close as possible to an ideal step, thus increasing the reliability of the measurement technique. Finally, the need of installing the heater in a rotating environment provides additional constraints, limiting the size and the weight of the device and the available power supply.
All of the aforementioned requirements lead to the design of a modular heater, represented in Figures 3.7 and 3.8, of the kind patented by Gillespie et al. [102]. The heater is composed of two identical stages, both made of a PTFE frame housing a fine metal mesh and four bus bars, two for each side, which hold the mesh steady and supply it with electric power. By applying a voltage to the bus bars the mesh is heated up by Joule effect, and is thus able to heat up the air flowing across it.
Each frame is 20 $mm$ thick with outer sides 210 $mm$ and 190 $mm$, and

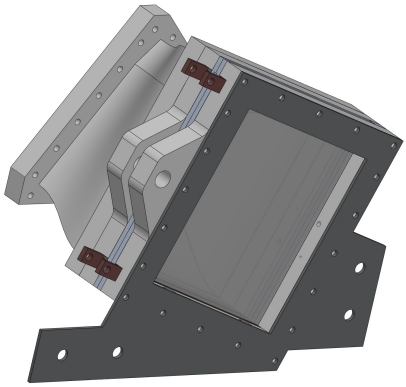

*Figure 3.7: CAD model of mesh heater and connection.*

realizes an inner passage section with sides 160 $mm$ and 140 $mm$. PTFE was selected for such component since it provides electrical insulation and is able to withstand temperatures (up to 250°$C$) higher than the expected operational temperatures of the device.

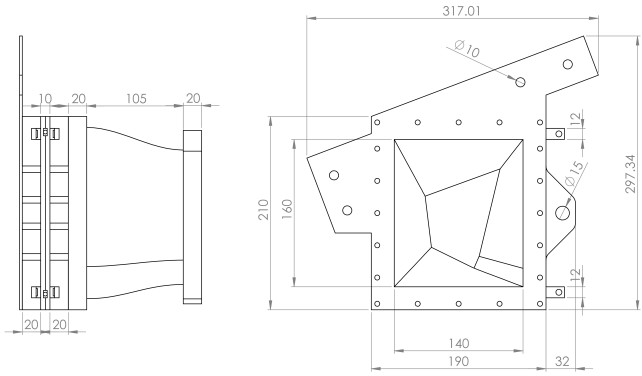


*Figure 3.8: Technical drawing of mesh heater and connection.*

The bus bars are located along the lower opposite sides of the passage section, and are connected to the frame by means of through screws. For each couple of bars, one is made of copper, has a rectangular cross section and actually performs the electrical connection between the mesh and the power supply. The second bar has the tasks to hold the mesh in position and to realize a suitable electric contact between the mesh and the copper bar by applying an adequate pressure. With the aim to perform both of these functions in the best possible way, this bar has a C-shaped cross section and is made of steel, thus taking advantage of the improved stiffness with respect to copper. Both the copper and the steel bars are $5\,mm$ thick and $12\,mm$ wide. The bus bars and the mesh are tightened together by means of five conical head bolts.
The metal grid is made of stainless steel wires with a diameter of $30\,\mu m$ arranged in a square mesh, with a distance between wires of $39\,\mu m$. This kind of mesh, which is one of the thinnest and thickest commercially available, was chosen due to its low thermal inertia, which allows to obtain a quick temperature variation of the air passing through it. An example of air temperature history downstream the heater is reported in Figure 3.9, which shows that at the beginning of one test (i.e. time

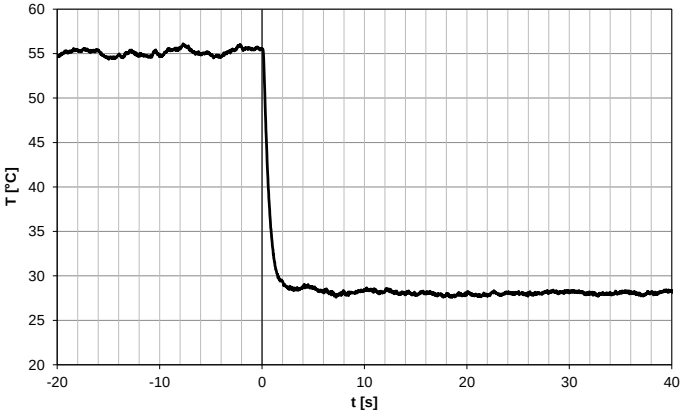


*Figure 3.9: Example of temperature history downstream the mesh heater.*

equal to zero) air takes around 3 $s$ to reach ambient temperature, a time which is considered satisfactory for the present case. A very fine mesh also allows to uniformly heat up the air across the whole passage section: this fact was verified by sampling temperature in different locations along the two main axes of the section.

The two stages are connected in a series and are fed by two DC power supplies Agilent N5763A, also connected in a series. Each of these units is able to provide up to 120 $A$ of direct current at 12.5 $V$, for a total power output of 1.5 $kW$. Such devices are also particularly suitable for transient heat transfer test, given the output response time of 0.05 $s$ and the capability to be shut down via a trigger signal. Since the power supplies are not installed onboard the rotating chassis, power transmission towards the heater is performed through a couple of slip rings on the rotary joint, capable of handling up to 100 $A$, 48 $V$ direct current. The features of the power supply system were also employed to determine the optimal size of the mesh: the length and width of the heating elements were defined to provide a voltage drop close to the available one when crossed by the maximum allowable current (100 $A$), thus fully exploiting the output of the DC power supplies.

During the heating phase, the mesh heater is usually set to provide around 1.8 $kW$ of thermal power to the inlet air. However, the management of such component for the whole time required to heat up the model can be critical, given its high power density. In fact, due to the non perfect electrical contact between the mesh and the bus bars heat is generated in such locations, which is not transferred to the air flow. For a short working time the excess heat is transferred to the high conductivity bus bars and thus causes a small wall temperature increase, with a negligible effect on flow temperature uniformity. However, for a long working time the temperature of the bus bars, which are installed into the low conductivity PTFE frames, can become high enough to significantly heat up the flow passing close to the wall and, eventually, damage the heater itself. In order to avoid such phenomenon, a cooling frame was installed in between the two stages of the heater. The cooling frame is made of aluminium

and hosts two straight cooling channels, which run along the shortest sides (i.e. the sides closer to the bus bars). During the heating phase, each channel is fed with compressed air: in this way the most part of the excess heat, which is transmitted from the bus bars to the cooling frame, is dispersed towards the laboratory environment. Compressed air is provided by a dedicated supply line, which is disconnected immediately before the rotating tests. Electric insulation between the bus bars and the cooling frame is obtained by using high temperature double side tape. Pictures of a mesh heater stage and of the cooling section are reported in Figure 3.10.

The mesh heater is also equipped with a filtering stage at the inlet section, and is connected to the rotating chassis by means of a support stage with brackets and a threaded rod. The location and orientation of the heater was set to align it with respect to the supply channel of the test article, as well as to obtain similar orientations for the cross sections of the heater and the channel. This choice, together with the design of the duct connecting the heater to the test article, allows to minimize the velocity non uniformities at the supply channel inlet section.

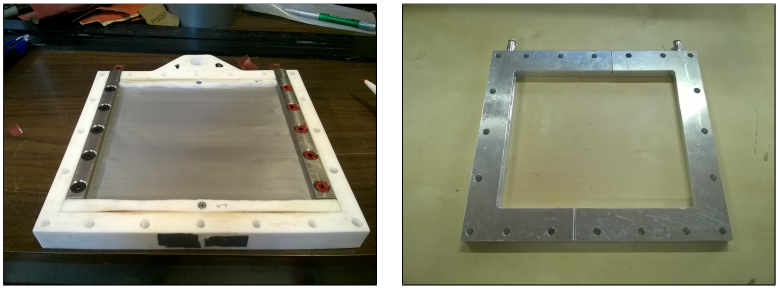

*(a)* *(b)*

*Figure 3.10: Mesh heater stage (a) and cooling frame (b).*

### 3.2.4 Air feeding system

The pneumatic system was designed in order to allow air circulation and to replicate the desired flow conditions inside the test article. Air enters the rig through the mesh heater, which is connected to the model by a 3D printed polyamide duct (visible in Figure 3.7). The flow then evolves into the test article, where a part passes through the impingement holes and is then collected into the extraction plenums, while the remaining part leaves the feeding channel at its outer radial extremity, realizing the upstream crossflow. The air is drawn from the five extraction plenums by means of five short DN40 ducts, housing a precalibrated orifice and a gate valve each in order to independently measure and set up the mass flow rate through each extraction row of holes. On the other hand, the crossflow mass flow rate is collected by a DN100 duct, connected to the test article with a custom designed flange. Such duct is made in copolymer polypropylene, which was chosen due to its lightness combined with thermal and mechanical properties adequate for the rig operational conditions. All the flows leaving the test articles are collected into a PMMA plenum, located in the center of the rotating chassis and with an outer size of $320 \times 440 \times 310\, mm^3$. The walls of the central plenum have a thickness of 25 $mm$, which was chosen in order to withstand the maximum operative pressure difference expected during the rig operation (around 40000 $Pa$). In order to control the crossflow mass flow rate, the outlet section of the corresponding pneumatic line inside the plenum can be partially obstructed thanks to a sliding aluminium plate, held in position by four bolts (Figure 3.11): such system was chosen since it is much lighter than a standard DN100 gate valve, despite making the flow set up slightly less practical.

The air flow is extracted from the central plenum through the hollow rotary joint. Downstream the joint, the flow enters a straight steel pipe (2 $m$ long, diameter DN150), on which a multi hole Pitot tube for overall mass flow measurement is installed. The steel tube is then connected to a T-junction, on a side of which a fast actuation bypass valve is installed. This device, which directly connects the vacuum system to the laboratory

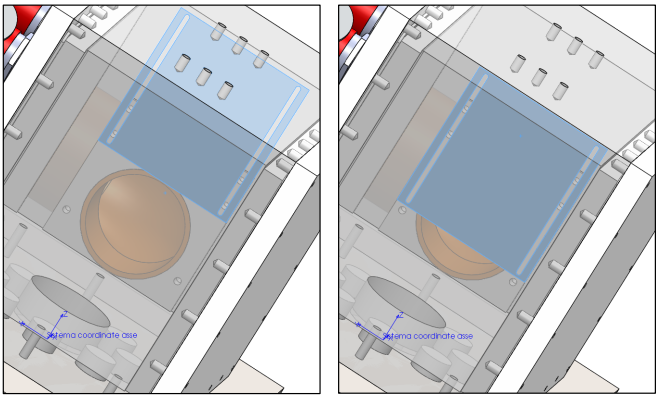

*Figure 3.11: Detail of the crossflow control plate in different positions.*

environment, is needed in order to apply the measurement technique presented in Section 2.2.2. During the heating phase the small mass flow rate needed to heat up the model is obtained by keeping the bypass valve opened and thus reducing the pressure drop across the rig. At the beginning of the test the valve is suddenly closed, thus allowing the whole nominal mass flow rate to enter the test article. The features of the employed valve were selected in order to obtain such behaviour: a DN150 butterfly valve was chosen (Ghibson BLKA LUG DN150) activated by a double effect pneumatic actuator (AIR TORQUE AT301DE). A 24 $V$ solenoid valve controls the actuator. The manufacturer declares a closing time of 0.23 $s$ and direct measurement confirmed that 90% closure is reached in around 0.13 $s$, which was considered satisfactory for the present case. The time employed by the flow perturbation to reach the model inlet was also evaluated ad found to be around 0.03 $s$. Moreover, time resolved measurements revealed that the nominal mass flow rate value sets up in less than the actual mass flow rate sampling time, which is lower than 1 $s$.

The shape of the pneumatic line connecting the rig to the vacuum system and the size and location of the bypass valve were also defined according to

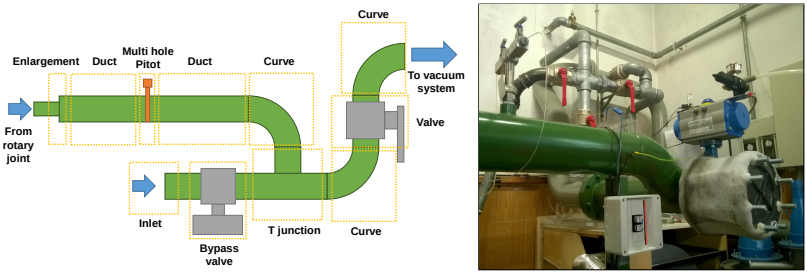


*Figure 3.12: Scheme (a) and picture (b) of the rig outlet line.*

the requirements of the measurement technique. In fact, it is mandatory that the mass flow rate employed during the rig heating phase is low enough to be heated up to the desired temperature using the available thermal power. This condition provides a limit value for the mass flow rate (around 45 $g/s$): as a consequence, when the rig is operated at its maximum capacity (maximum Reynolds and crossflow conditions) the mass flow rate across the rig needs to be lower than such value when the bypass valve is opened. To achieve this goal, a predesign 0D fluid model of the whole rig and pneumatic system was created in a Microsoft Excel worksheet, which allowed to test different configurations of the discharge line. In particular, the model was run with no bypass in order to find the volumetric flow rate; this value was then imposed (since the pump speed is not varied) in a second run of the model with the bypass valve opened, which provided the mass flow rate across the rig during the heating phase. A scheme and a picture of the rig outlet line are reported in Figure 3.12. The outlet line is connected to a vacuum system composed of two couples of vacuum pumps, each in a parallel configuration: a couple is realized by PVR and has an overall capacity of 1800 $m^3/h$, the other is manufactured by Becker and has a total capacity of 600 $m^3/h$. Each machine is powered by a three-phase asynchronous electric motor. The two couples are controlled by a dedicated control board each, which allows to independently turn on or off each pump and to vary their speed through an inverter.

### 3.2.5 Rotating system

In order to study heat transfer in rotating conditions, the model of the cooling geometry and the main rig components need to be installed on a suitable device. To achieve this goal, the rotary equipment designed by Bonanni et al. [103] was exploited. The rotating chassis, on which the main components of the rig are installed, has a horizontal axis and a maximum radius of 1100 *mm*. The structure is made of welded Fe510 square profiles, in order to adequately support the rig components at high rotational speeds. The model of the cooling geometry, the pneumatic extraction lines and the measurement devices are all installed on the same side of the chassis: as a consequence, the opposite side can be totally exploited for balancing purposes. The balancing system, represented in Figure 3.13, is composed of two 670 *mm* long steel rectangular profiles, to which a series of lead weights is connected by means of threaded rods. The number and location of the weights was defined in order to balance the rig both in static and rotating conditions: to achieve this goal, the mass distribution was set to make both the center of gravity and one of the principal axis of inertia of the whole rotating equipment lie along the

*Figure 3.13: Picture of the rig balancing system.*

rotation axis. This operation, which was performed *a priori* on the CAD model of the rig, allowed to reach the maximum rotational speed (around 150 *rpm*) without appreciable vibrations of the structure.
A rotary joint provided by Celco Profil performs the multiple tasks of supporting the rotating assembly, transmitting the rotary motion to the chassis, extracting air from the test section and providing power supply and data transfer for the onboard instrumentation. The latter task is obtained thanks to a series of slip rings, which can transmit one line each of DC and 220 $V$ AC electric current, a single Ethernet channel an up to 8 type T thermocouple signals. Rotation is obtained thanks to an electric motor (Marelli 7.5 $kW$ three phase asynchronous) controlled by an inverter (Lenze 7.5 $kW$, 400 $V$) and connected to the joint by means of a toothed belt. The whole assembly is supported by a steel frame and linked to the ground through damping supports. The safety of the laboratory environment is granted by a steel modular cage enclosing the whole rotating assembly.

### 3.2.6 Measurement devices

In order to study the heat transfer phenomenon, as well as to set up and control the experimental apparatus, the knowledge of thermal and fluid-dynamic parameters in different locations of the rig is requested. This task is carried on thanks to a series of measurement devices, installed in different locations of the rig, which will be described in this section.

#### 3.2.6.1 Mass flow measurement

For the present case, test conditions are mainly defined in terms of Reynolds number and crossflow ratio (see Section 3.1), and both of these parameters are a direct function of the mass flow rates across different sections of the model. As a consequence, the knowledge of mass flow rate values is required in order to correctly set up the tests.
The mass flow rate crossing each row of film cooling and showerhead holes is measured at the exit section of the corresponding extraction

plenum thanks to a custom designed orifice, which allows to relate the static pressure difference across the device with the mass flow rate value. For the present case, such difference was evaluated thanks to a couple of pressure probes, one in the upstream plenum and one located one duct diameter (i.e. 40 $mm$) downstream the orifice along the pneumatic discharge line. Each orifice has an inner diameter of 25.2 $mm$, which was chosen as a tradeoff between the opposite requirements of providing a measurable pressure difference and limiting the pressure losses. Since the dimensions of the rig did not allow to install orifices compliant with the standards, each device was calibrated before the tests in order to determine the corresponding relation between the pressure drop and the mass flow rate. To achieve this goal, each extraction line was connected to a pneumatic line housing an orifice compliant with the standard UNI EN ISO 5167-1: in this way, the mass flow through the custom orifice is known and equal to the one measured by the standard orifice. The calibration was performed by setting different mass flow rate values and recording the correspondent pressure drops of the custom orifice, as well as the air temperature. This operation allows to evaluate the pressure ratio $\beta$ across the custom orifice:

$$\beta = \frac{p_{up}}{p_{down}} \tag{3.7}$$

which can be associated with the corresponding value of corrected mass flow rate $\dot{m}_{corr}$:

$$\dot{m}_{corr} = \frac{\dot{m} \cdot \sqrt{RT}}{p_{up} D_o^2} \tag{3.8}$$

where $R$ is the specific gas constant and $D_o$ is the custom orifice diameter. The obtained $\beta$ and $\dot{m}_{corr}$ couples were correlated using the following function:

$$\dot{m}_{corr} = (a \cdot \beta + b) \cdot \sqrt{\frac{2\gamma}{\gamma - 1} \left( \beta^{-\frac{2}{\gamma}} - \beta^{-\frac{1+\gamma}{\gamma}} \right)} \tag{3.9}$$

where $a$ and $b$ are constants which are defined thanks to a best fit operation. Such function was derived from the definition of the discharge coefficient ,

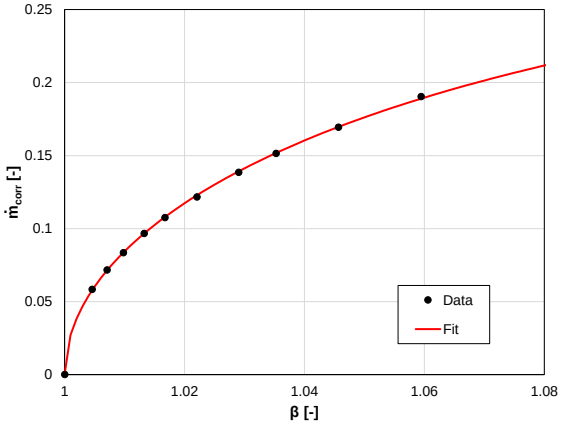


*Figure 3.14: Data and fitted flow function for $FC_A$ orifice.*

with the aim to replicate the physical behaviour of a concentrated pressure loss. An example of the relation obtained for a single custom orifice is reported in Figure 3.14. In this way, a flow function is obtained for each of the custom orifices, which was directly implemented in the data acquisition software.

The knowledge of the mass flow rates across the five extraction rows also allows to evaluate the total impingement mass flow, which is given by the sum of such values. On the other hand, a direct measurement of the crossflow mass flow rate was not performed, since due to space and weight constraints it was not practical to install a measurement device on the crossflow extraction line. As a consequence, such quantity was calculated as the difference between the total mass flow rate across the rig and the impingement mass flow rate. In the present case, the overall mass flow was measured on the pneumatic line connecting the rig to the vacuum pumps by means of a multi-hole Pitot tube, which was preferred to a standard calibrated orifice given the lower generated pressure drops and the reduced constraints in terms of installation.

#### 3.2.6.2 Pressure measurement

As seen in the previous section, pressure measurements are required in order to evaluate the mass flow rate, which is performed thanks to the pressure probes located upstream and downstream the extraction orifices and directly on the multi-hole Pitot tube. Even so, the knowledge of pressure value also allows to control the rig operation and to evaluate the flow parameters for the investigated geometries. To achieve this goal, pressure is evaluated in different locations of the test article. In particular, seven pressure probes are located along the feeding channel and two inside the impingement cavity (at its hub and tip sections respectively), thus allowing to perform a flow characterization of the impingement holes. Static pressure inside the central plenum is also measured in order to grant a safe operation for the rig, since inside such device the lowest pressure of the whole rotating assembly is present.
In the present case, static pressure was measured using two Scanivalve DSA 3217 pressure scanners, each equipped with 16 temperature compensated piezoresistive relative pressure sensors. In order to obtain the absolute pressure value, reference pressure for the DSA scanner was chosen as the ambient one, which gets measured by a mercury barometer. For measurements onboard the rotating chassis, a single DSA module is employed, housing 8 channels with a full scale deflection of 5 *psid* ($\simeq$ 35000 $Pa$) and 8 with a range of 15 *psid* ($\simeq$ 100000 $Pa$). All the channels have 0.05% accuracy over full scale. This DSA module was directly installed on the central plenum along the rotation axis to minimize the deformation of the piezoresistive elements due to centrifugal forces. The second DSA module records the total and static pressure measurement on the multi-hole Pitot tube, and is thus installed close to such component. In this case, a unit was employed with 8 channels with 1 *psid* ($\simeq$ 7000 $Pa$) range and 0.10% accuracy and 8 channels with 5 *psid* range and 0.05% accuracy. The smaller range and uncertainty of this device allow to improve the mass flow rate measurement accuracy. Only for the largest values of mass flow rate a higher range unit was employed, identical to the one installed on the rotating chassis.

#### 3.2.6.3 Temperature measurement

Temperature is the main physical quantity which needs to be recorded in convective heat transfer measurements. In particular, the experimental technique employed in the present work requires the knowledge of both the flow and the surface temperature evolution, which are recorded thanks to thermocouples and thermochromic liquid crystals respectively.

**Thermocouples** The measurement of air temperature is performed using type T thermocouple located in significant sections of the rig, all manufactured by Tersid and with an accuracy of 0.5 $K$. A junction is installed in the centerline of each impingement hole: these sensors provide the actual temperature evolution for every single impingement jet, allowing to perform an independent data postprocessing for each jet and thus to take into account any possible difference in the temperature profile. In order to correctly apply the transient technique, it is necessary to accurately describe the time evolution of the air temperature, which requires the use of sensors with a low thermal inertia. For the present case, jet temperature is recorded using thermocouples with exposed hot junction and with a diameter of the weld joint of around 0.3 $mm$. The combination of small sensor mass and high jet velocity provides a maximum time constant of around 0.3 $s$ for such thermocouples, which allows an accurate reconstruction of the temperature history in every investigated condition. Flow temperature is also required to correctly evaluate air density and thus mass flow rate values: as a consequence, a thermocouple is also installed upstream each calibrated orifice inside the extraction plenums, as well as immediately downstream the multi-hole Pitot tube along the rig extraction line. Thermocouples are also employed in order to verify that the temperature of the model is uniform and steady at the beginning of the test: to achieve this goal, two thermocouples are installed inside the heat transfer surface at half its thickness and 20 $mm$ far from the edge of the surface at opposite sides (hub and tip).
The thermocouples located onboard the rotating chassis are connected to a NI 9214 16 channel isothermal input module, equipped with three

cold junction compensation sensors which provide the absolute reference temperature value. Using this device, a sampling rate around 47 $S/s$ was obtained for the sensors, thus providing an accurate description of the air temperature evolution. The combined accuracy of sensors and input module provide an overall accuracy of 1.35 $K$ for the thermocouples onboard the rotating frame. The module is linked to a NI CDAQ-9191 Wi-Fi chassis, which allows wireless temperature data transmission to an acquisition personal computer.
Temperature measurement for the thermocouple close to the multi-hole Pitot is performed by a 20 channel multiplexer module connected to an Agilent HP34970A data acquisition unit. The cold junctions of all channels are located inside a thermally insulated hollow brass cylinder, in order to have a constant and uniform reference temperature for all the junctions, and the temperature compensation is performed thanks to a Pt100 RTD (uncertainty 0.1 $K$, level of confidence 95%) located inside the cylinder. The unit is connected to the acquisition personal computer by means of a GPIB interface, which allows to control the unit and to record the measured values.

**TLC** The temperature evolution of the jet target surface is obtained thanks to a coating of thermochromic liquid crystal paint. Since the knowledge of a single temperature value is required in order to apply the measurement technique (see section 2.2.2), narrow band TLCs were employed in the present case. In particular, the R40C1W formulation provided by Hallcrest was selected, composed of TLC with a declared red start temperature of $40°C$ and difference between the red start and blue start temperatures of $1°C$. The choice of the most suitable activation range was performed in order to minimize the measurement uncertainty, according to the criterion proposed by Wolfersdorf and Weigand [20] and presented in Equation 2.11.
The TLC formulation is provided as a microencapsulated paint, and was applied to the heat transfer surface by means of a professional airbrush. In order to have a strong color response, as well as to reduce the possible

aging effects [90, 93, 97], a significantly thick layer of TLC paint is required (namely between 20 and 50$\mu m$), and thus the application was repeated until the surface appeared completely opaque. The coated surface was then painted with a water based black paint, which is needed in order to absorb all the visible wavelengths not reflected by the TLCs and thus to have a cleaner color output.

As seen in section 2.3, in order to use a TLC coating for quantitative measurements it is necessary to accurately know the colour-temperature response of the crystals, which can be obtained by means of a suitable calibration operation. The chromatic output of the TLCs depends upon a wide number of parameters, including the image acquisition device, the light source kind and location, the viewing angle and the eventual medium interposed between the crystals and the observer. The most practical and reliable way to take into account all of these effects would be to directly calibrate the TLC coating on the investigated system (*in situ* calibration), which requires to equip the crystal coated surface with temperature measurement devices different from TLCs (e.g. thermocouples). This kind of calibration is not suitable for the present case, since the small dimension and the limited accessibility of the heat transfer surface make the application of the calibration equipment challenging and likely disruptive for the measurement itself. To overcome these issues an *ex situ* calibration apparatus was set up, with the aim of replicating the same optical conditions as the actual test rig. Such device was designed in order to apply the steady state gradient method presented by Chan et al. [98]. TLC paint and black coating were applied to a PMMA plate of the same thickness as the heat transfer surface. A 4 $mm$ thick, rectangular aluminium plate was then thermally connected to the TLC coated surface by means of a high conductivity compound. A cartridge electrical heater is installed at a side of the plate, while the opposite side can be cooled down by means of a flow of compressed air. An expanded polyurethane enclosing thermally insulates the whole assembly from the environment. The plate is designed in such a way that a suitable one-dimensional temperature gradient can be set along its length by regulating the heating

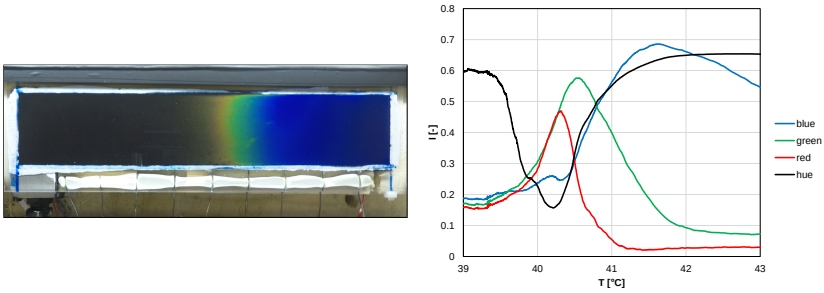


*(a)* *(b)*

*Figure 3.15: Example of calibration run (a) and corresponding output (b).*

power and air mass flow rate. Nine type T thermocouples, whose positions are precisely known, are embedded into the aluminium plate and measure the surface temperature in the corresponding locations, thus allowing to rebuild the thermal gradient. The camera type and illumination device are the same installed in the actual test rig, and allow to record images of the calibration sample: in this way, the TLC color can be associated with the temperature data (Figure 3.15). To improve the accuracy in the narrow TLC activation range, thermocouples were recalibrated using a Pt100 RTD. In order to apply the employed measurement technique, a precise event needs to be associated with specific temperature ($T_{event}$): in this case, the most repeatable and evident effect resulted to be the green colour peak intensity, which was chosen as the color descriptor. Since during the tests TLCs undergo a cycle of heating and subsequent cooling, thermal hysteresis effects also need to be taken into account: as a consequence, each acquisition was performed by applying the same thermal cycle as the test article, i.e. by uniformly heating the calibration sample at 55-56$^{\circ}C$ for around 90 minutes, and then cooling it down to the TLC activation range.

Calibration was repeated several times in order to improve the reliability of the results. For the lot of TLC paint employed for the whole experimental campaign, the calibration runs provided a mean value for the

green peak at $40.5°C$, with a standard deviation of $0.13°C$.
These runs also verified that the peak green intensity occurs at approximately the same temperature if the TLCs are heated to a maximum temperature lower than $57°C$ and for a maximum time of 100 minutes: as a consequence, during the tests the model heating phase is performed in order not to exceed such limits. Moreover, repeated thermal cycles have shown non significant ageing effects for the TLCs with the employed conditions.

#### 3.2.6.4 Image acquisition

In order to record the TLC chromatic information and convert it into temperature data, a digital image acquisition system is required. In this case, action cameras were employed for this purpose. The choice of such devices is bound to the constraints imposed by the measurement technique, which requires the knowledge of the time resolved temperature evolution of the heat transfer surface: as a consequence, video acquisition devices should be installed onboard the rotating chassis. Action cameras are particularly suitable for this application since they are compact and lightweight and do not need of external power supply or acquisition hardware. Moreover, they are usually equipped with wide angle optics, which allow to install them very close to the model while still getting a complete view of the investigated surface. Finally, the rugged construction and the fixed focus optics grant that the camera is not damaged and the optical setup is not altered even by strong centrifugal forces. Amongst all the commercially available products, GoPro HERO5 Black cameras were selected for the present case (Figure 3.16a). This choice is due to the fact that such cameras allow to manually set a wide number of optical and chromatic properties (white balance, color profile, gain, exposure), which is a mandatory requirement in order to obtain repeatable results.
Five cameras were employed in the present case, each installed on the outer surface of an extraction plenum. Each camera is supported by a custom designed PMMA housing, which firmly locks the device in place while still allowing to operate on the rear touchscreen and side control

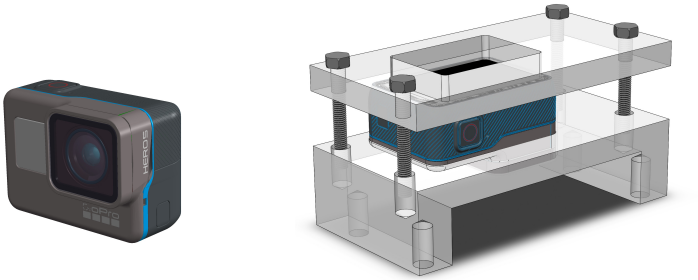

(a) (b)

*Figure 3.16: GoPro HERO5 Black camera (a) and camera support (b).*

buttons and to open the connection and battery compartment doors (Figure 3.16b).

The location of the five cameras and the shape and size of the supports was designed in order to obtain a complete vision of the heat transfer surface. For the present case, cameras were set to record a $1920 \times 1080$ pixel video file stream at constant framerate of around 29.97 $fps$, which provides a high spatial resolution for the investigated surface while keeping the size of data to be postprocessed at a manageable level. It was also verified that the framerate value was constant along the test duration and that no frames are missed during the recording by preliminary assessment of the synchronization between each camera and a 60 $Hz$ PC screen.

The illumination of the investigated surface is performed by means of a 50 $W$ white led strip. Thanks to its flexibility the strip was directly taped on the model outer surface: this allowed to freely set its location in order to provide as uniform as possible illumination while avoiding local light reflections. With the employed experimental setup, however, light radiation may be absorbed by the black paint, thus increasing the surface temperature in a non controllable way: this effect was minimized by lighting up the led strip immediately before the test.

When performing optical measurements in a rotating environments, also the external optical disturbances need to be taken into account: in fact,

the relative position of the test article with respect to the external light sources continuously changes during the rotation, and so may do the local color intensity. In order to avoid this phenomenon, the test section is entirely covered with opaque dark tape, and rotating tests are performed by creating a dark environment into the laboratory.

### 3.2.7 Synchronization system

The employed experimental technique is based upon the measurement of the time response of the TLC following a sudden variation of air temperature, measured by thermocouples. Moreover, in order to correctly apply the technique the bypass valve must be closed and the mesh heater must be switched off in the same moment. As a consequence, it is of primary importance that these events are synchronized and that the corresponding time instant is recorded by all measurement instruments. This goal is achieved by setting a suitable synchronization system, a scheme of which is reported in Figure 3.17.
After the heating phase and once the desired initial conditions are met, the test is started by manually activating a control switch, which closes a circuit fed by a 24 $V$ DC power supply. Such circuit powers up the solenoid valve of the pneumatic actuator, which in turn closes the bypass valve at the rig outlet. Two 24 $V$ relays are also connected to the circuit. The first relay closes the circuit of a thermocouple junction, which is connected to the NI9214 acquisition module installed on the rotating chassis by means of the slip rings. The module provides an error output signal when the thermocouple circuit is open and the correct temperature when the circuit is closed: as a consequence, the continuous recording of this "dummy" thermocouple signal allows to identify the moment of the control switch activation, as well as to synchronize it with the output of the other thermocouples connected to the acquisition module. The second relay closes a circuit parallel connected to both the DC power supplies via a D-sub connector: these units are set in order to shut down once the circuit is closed, thus interrupting the current distribution to the mesh heater. Moreover, five micro light bulbs are parallel connected to the

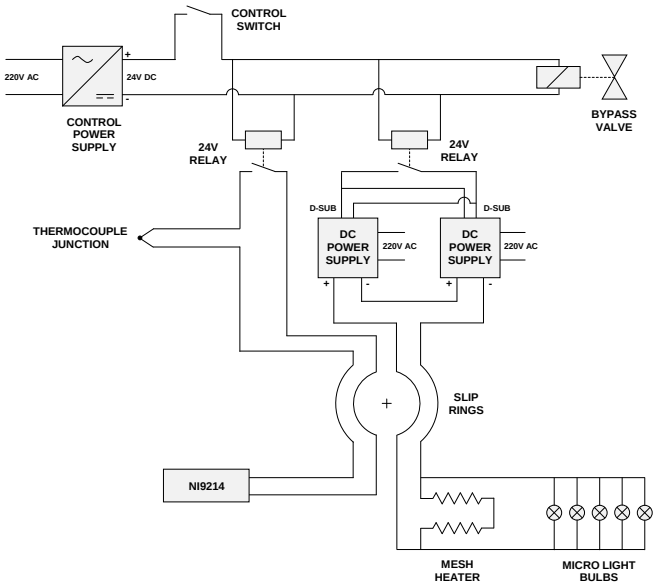


*Figure 3.17: Scheme of the rig synchronization system.*

mesh heater and are observed by a camera each: in this way, it is possible to identify the frame corresponding to the test start, thus synchronizing the video acquisition with the other events.
All the events synchronized with this system occur in a time frame smaller than 0.05 $s$, which is lower than the combined time uncertainty of camera framerate and temperature acquisition (around 0.07 $s$): as a consequence, they can be considered as simultaneous for the present case.

## 3.3 Test procedure

The test execution procedure consists of all the operations performed to set up the desired test conditions, run the transient experiment and simultaneously record the all of the parameters of interest. The control of the rig is performed by means of a dedicated personal computer, which

is connected to temperature and pressure measurement devices. Data acquisition and visualisation is obtained thanks to two custom designed LabVIEW programs, one dedicated to the high frequency acquisition of the thermocouples upstream the impingement jets and the other to the recording of the other pressure and temperature values. The latter program also performs the direct calculation of mass flow rate values, thus allowing to set and record the values of such quantity.
Before the test, a preliminary check up of the rig is performed: a visual inspection of the rotating chassis is carried out in order to verify that all the connections are tightened, and it is verified that all of the measurement instruments are correctly connected and able to record. Subsequently, the mass flow rate and rotational speed values corresponding to the desired test conditions, expressed as the combination of Reynolds number, Rotation number, crossflow ratio and extraction split, are obtained thanks to a Microsoft Excel worksheet, given the actual ambient pressure and temperature values. A flow check of the rig is then performed: the vacuum pumps are switched on, their speed is adjusted and the valves onboard the rig are operated in order to target the desired mass flow rate values. During this operation, the bypass valve is closed. Once the correct test conditions are set, the bypass valve is opened, so that the mass flow rate across the rig decreases due to the reduced pressure drop. The DC power supplies are then switched on and regulated in order to heat up the air flow, and thus the test article, to a temperature of around 55-56$^{\circ}C$. During the heating phase, the temperature of the jets are continuously monitored, thus allowing to adjust the power output in order to maintain the air temperature to a constant and desired value. The inner temperatures of the heat transfer surface provided by the two embedded thermocouples are also recorded, thus allowing to check when the wall temperature is uniform and equal to the air one. The duration of the heating phase is usually around 90 minutes when starting from ambient conditions. Jet temperatures are recorded during this phase, since they will be employed to evaluate the initial temperature of the heat transfer surface (see Section 3.4.2).

Once suitable thermal conditions for the test article are reached, the transient test can actually take place. In case of a rotating test, all the external connections are unplugged from the rotating chassis (namely the compressed air supply for the mesh heater cooling stage) and the desired rotational speed is set on the electric motor control panel. The LabVIEW programs then begin recording data, and the video acquisition is also launched. Finally, the test is actually started by activating the control switch, which closes the bypass valve and shuts down the heaters: the whole nominal mass flow rate thus enters the test article at ambient temperature and the transient heat transfer takes place.
The test is considered as concluded when the TLCs reach the peak green color intensity in every point of the heat transfer surface. The time taken by this phenomenon to occur depends upon the flow conditions and the air temperature, i.e. the laboratory ambient temperature. Given the employed measurement technique, test duration is a critical parameter in order to obtain significant and reliable results, and thus requires a deeper analysis to be performed.

### 3.3.1 Test duration analysis

The use of a time based thermal analysis implies that also the investigated time frame may be subject to some constraints in order to grant the validity of the analysis. In particular, an upper limit for the duration is provided by the semi-infinite solid hypothesis of the transient technique, which requires that during the test the temperature perturbation does not reach the opposite side of the heat transfer surface. In order to respect this condition, the criterion proposed by Vogel and Weigand [85] and reported in Equation 2.10 was applied. In this case, since both sides of the heat transfer surface are exposed to a temperature change the reference wall thickness value is considered as equal to half the wall thickness, i.e. 5 $mm$: this provides a maximum value for test duration of 57.5 $s$. Since the laboratory environment can be thermostatically controlled, it was possible to vary the rig inlet temperature (namely between 20°$C$ and 35°$C$) in order to alter the test duration. For the present case, tests were

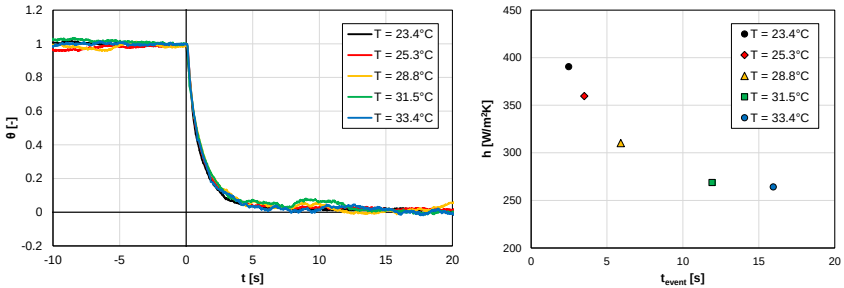


(a) (b)

*Figure 3.18: Non dimensional air temperature ratio (a) and h values in the same point (b) for tests performed at different jet temperatures.*

performed in order to obtain a full TLC color play within 50 $s$ in every investigated condition, thus respecting the hypothesis of the employed method.

On the other hand, a lower limit for the test duration is also present. For a given value of Reynolds number, the obtained Nusselt number in a certain point of the heat transfer surface should be insensitive to the value of air temperature. However, with the transient heat transfer technique this may not occur in high heat transfer regions, e.g. close to the jet stagnation point. This phenomenon can be appreciated by considering the data reported in Figure 3.18, which presents the outcomes of different tests performed in the same condition (namely $Re_j = 50000$, $Ro_j = 0$, $Cr = 40\%$ for GTE-A geometry) but using different air reference temperatures $T_{ref}$. The left chart presents the air temperature history of such tests, expressed as non dimensional temperature $\theta$:

$$\theta(t) = \frac{T_a(t) - T_{ref}}{T_i - T_{ref}} \tag{3.10}$$

where $T_a$ is air temperature. On the other hand, the right chart presents $h$ values sampled in the same point of the investigated surface for the different tests, plotted against the corresponding TLC event time. This

last chart shows that the measured $h$ values decrease as TLC event time increases, i.e. as air reference temperature increases, reaching an asymptotic value over a certain event time value. An interpretation of this phenomenon, which was also observed by other authors [34], is not straightforward to provide. A plausible hypothesis is that during the first seconds of the test strongly unsteady fluid and thermal phenomena occur within the test rig, which may lead to different heat transfer conditions with respect to the expected ones. Since the semi-infinite wall transient technique is based on the assumption that the heat transfer coefficient $h$ is constant all along the test, the energy balance providing $h$ may be influenced by the first section of the test if TLC event occurs close to the test beginning. On the other hand, if the event occurs after a reasonable amount of time the relative weight of the initial phenomena reduces down to a negligible level. As a consequence, in order to obtain temperature-independent results TLC event needs to occur beyond a certain time in every point of the surface, which for the present case was evaluated to be around 12 $s$. Given these considerations, this was again obtained by imposing a suitable value for the inlet air temperature, namely higher for high Reynolds tests and lower for low Reynolds tests. In fact, since the curves of Figure 3.18a are all similar, it can be stated that the transient phenomena occurring in the first part of the experiment are temperature independent, and it is thus possible vary air temperature without altering the effect of such phenomena on heat transfer. Different experiments were carried out for each significant condition (namely each nominal Reynolds value) to determine an inlet air temperature value which would provide a test duration lying in between the upper and the lower limit.

## 3.4 Data postprocessing

For every test, the experimental procedure described in the previous section provides a significant amount of raw data, namely RGB videos and text files containing time resolved temperature, pressure and mass flow rate values. In order to obtain spatially resolved heat transfer coefficient

distributions this data needs to be processed, which is performed according to a well defined procedure and using specific software tools. The details of the postprocessing operation will be presented in this section.

### 3.4.1 Video data analysis

The TLC chromatic information is stored inside five video files, one for each camera. In order to extract this information, each video is converted into a sequence of frames in bitmap format, and the frames recorded before the beginning of the test are identified (thanks to the micro light bulb switch off) and eliminated. Knowing the video framerate, a custom Matlab macro reads each frame and associates to it the corresponding time elapsed from the beginning of the test. The same macro also crops the frames (in order to reduce the amount of data to be processed) and applies them a mask (which excludes the areas where measurement is not reliable or possible, e.g. the extraction holes). Green is then extracted from each frame and stored into a $x \times y \times n$ array, where $x$ and $y$ are the sizes in pixel of the cropped frame and $n$ is the number of the frames. A simple maximum finding algorithm is finally applied to each pixel, providing the frame number, and thus the corresponding time, in which the TLC event occurs. These time values are stored in a $x \times y$ array, the so called *event time matrix*, which is stored in a text file in order to be employed for the subsequent heat transfer evaluation.

### 3.4.2 Heat transfer calculation

In order to calculate heat transfer coefficient values according to the transient method, Fourier's conduction equation needs to be solved for the investigated surface. This requires the knowledge of the time and temperature corresponding to the TLC event, as well as of the air temperature history, the wall initial temperature and the material properties. TLC event time is contained in the previously evaluated event time matrix, while event temperature is known thanks to the TLC calibration. The time resolved air temperature is obtained by extracting

the jet temperature from the raw data and evaluating the time elapsed between each acquisition and the beginning of the test, identified thanks to the "dummy" thermocouple signal (see Section 3.2.7). On the other hand, the initial uniform value of the wall temperature is derived from air temperature. In fact, thanks to the test article design it can be supposed that at the beginning of the test the wall temperature is uniform and equal to the air one: as a consequence, the initial wall temperature is set as equal to the time averaged jet temperature before the test.
In the present case, the solution of the transient conduction equation is performed by the in house code *HTCvalue*. For a given value of event time $t_{event}$, the program evaluates the corresponding heat transfer coefficient $h$ through an iterative procedure, consisting of the following steps:

1. A first attempt $h$ value is set;
2. Fourier transient heat conduction equation is solved imposing the first attempt $h$ until the event time $t_{event}$;
3. The obtained wall temperature value is compared with the event temperature given by the TLC calibration;
4. If the difference between the two temperatures is lower than a given tolerance (typically $0.001°C$) the imposed $h$ value is considered valid; otherwise, a new value of $h$ is assumed using the secant method and the procedure restarts from point 1.

The whole procedure is repeated until the convergence on $h$ value is reached. In order to improve the measurement accuracy, the actual shape of the air temperature history is taken into account by the code: this is obtained by discretizing air temperature into a series of individual step changes and thus applying the superposed solution of Fourier equation in the form of Eq. 2.8.
Since the leading edge surface is curved and the employed analytical solutions for heat transfer are obtained for a flat plate, it is necessary to quantify the error introduced by such approach. In the present case, this was evaluated by applying an explicit finite difference method in cylindrical

coordinates to a series of sample points which made it possible to verify that, due to the small TLC event times, surface curvature has a negligible effect on heat conduction inside the wall (maximum discrepancies on $h$ lower than 4% locally and lower than 1% in area averaged terms).
Since in the present case the number of points in which $h$ should be evaluated is considerably high (ranging from 200000 to over 570000 for each camera) the application of the aforementioned procedure to every element of the event time matrix would be significantly time consuming. In order to reduce the amount of time required for the calculation, a fast approach procedure was implemented, on the example of the ones adopted for previous works [88]. The iterative procedure is applied to a limited number of event time values (usually 500) equally spaced and sampled between the minimum and the maximum value of the event time matrix. The obtained $h$ values are then employed to build and interpolant in the form $h = f(t_{event})$, which is then applied to every point of the original event time matrix. In this way, the full heat transfer coefficient distribution is obtained with a three orders of magnitude reduction in computational cost. The error introduced using this procedure was evaluated and was found to be lower than 0.1% locally, thus having a negligible effect in the final outcome of the calculation.
The event time matrix generated by each camera is processed using the *HTCvalue* code. Moreover, since the wall initial temperature and air temperature history are known for the various impingement jets, for each camera the code is independently applied to every jet, thus allowing to take into consideration the local variations of air and wall temperature. In this way, a complete two dimensional heat transfer distribution is obtained for each camera, an example of which is presented in Figure 3.19.

### 3.4.3 Data mapping

In order to obtain a full space resolved heat transfer coefficient map on the investigated surface, the outputs of the five cameras need to be combined. However, the $h$ patterns resulting from the previous step are based upon the direct video frames, and are thus distorted by both the camera

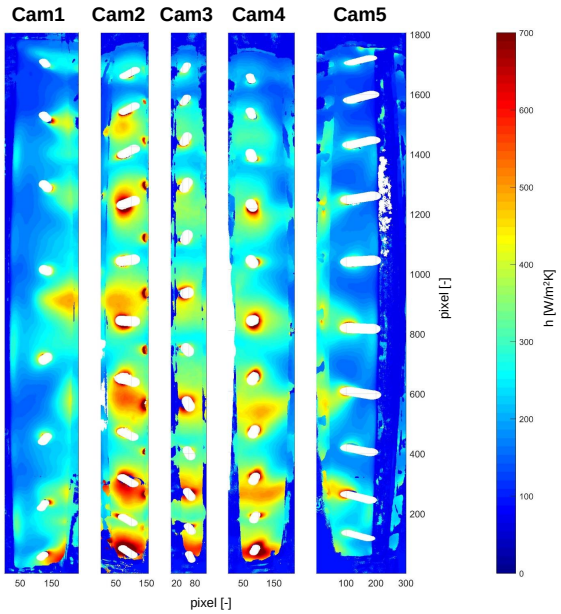


*Figure 3.19: Example of raw h distributions obtained for the five cameras.*

wide angle lens and the PMMA optical distortion: as a consequence, a simple combination of the five maps is not possible. Moreover, the maps of Figure 3.19 contain a sizeable number of points which are non significant for the measurement, namely the points located outside the investigated surface but still included in the camera field of view. These issues could be sorted out if such distributions could be interpreted, identifying the points actually belonging to the investigated surface and knowing their spatial location. In order to perform this operation, a custom 3D mapping procedure was developed, a scheme of which is reported in Figure 3.20. The location and viewing range of each camera is rebuilt in the CAD space of the test article, where the jet target surface is coloured with a linear gray scale according to the variable which needs to be mapped. In this case, four gray scale images are generated, corresponding to the $x$, $y$, and

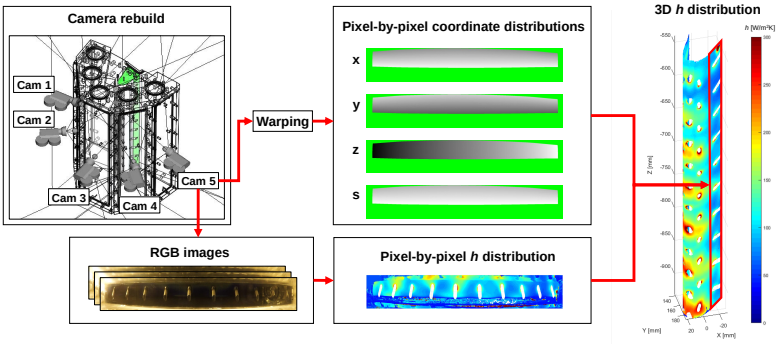


*Figure 3.20: Scheme of the camera mapping procedure.*

$z$ coordinates as well as to the coordinate $s$ along the heat transfer surface span. These images are then warped in order to obtain an accurate pixel by pixel correspondence with the raw $h$ map, thus taking into account the optical distortion effects of camera lens and PMMA. The location of two known points are then identified on the warped gray scale images: in this way, it is possible to associate the coordinate values of such points with the gray intensity on the corresponding image. This allows to transform the gray scale images in coordinate distributions by simply applying a linear interpolation to the gray intensity values. It is thus possible to know the spatial coordinates of any pixel in the heat transfer map by querying the points of the coordinate distributions having the same indices. In order to identify the points not belonging to the investigated surface, a non-gray value is attributed to the corresponding pixel (pure green in the present case), which allows to easily exclude such points them from the analysis. The whole mapping is performed by Matlab scripts, while the grayscale images are obtained using Solidworks.

Once the procedure is applied to every camera, the five output are merged together and reinterpolated over a regularly spaced grid, thus obtaining both 3D and plane developed ($s$-$z$ coordinate space) heat transfer distributions.

## 3.5 Uncertainty analysis

In order to provide physical relevance to any measured quantity, the corresponding uncertainty needs to be known. For the present case, the uncertainty analysis was carried out according to the standard ANSI/ASME PTC 19.1 [104] based on Kline and McClintock [105] method. For a given recorded quantity, its uncertainty is related to the accuracy of the devices employed for the measurement and to the definition of the quantity itself. In fact, according to whether the quantity is obtained by a primary measurement or derived from other quantities different approaches need to be employed.

A quantity is derived from a primary measurement if it corresponds to the direct output of a measurement device (e.g. voltage from a voltmeter). In this case, the uncertainty is provided by the manufacturer of the measurement device and is usually expressed as an uncertainty interval, i.e. a symmetrical interval surrounding the measured value within which the true value should lie. If $G$ is the measured quantity, the uncertainty interval is usually expressed as

$$G \pm \Delta G \tag{3.11}$$

Assuming that $G$ can be statistically described by a Gaussian distribution, the uncertainty $\Delta G$ is usually provided as the corresponding standard deviation, often defined with a 95% confidence level. The uncertainty provided in the previous sections for pressure and temperature values are compliant with such definition.

If the quantity $G$ is defined as a function of $n$ quantities $g_i$, each of which is obtained by a direct measurement, the uncertainty interval of $G$ will also be a function of the uncertainties $\Delta g_i$ of such primary quantities:

$$G \pm \Delta G = f\left(g_1 \pm \Delta g_1, g_2 \pm \Delta g_2, \ ..., \ g_n \pm \Delta g_n\right) \tag{3.12}$$

In this case, it can be demonstrated that the uncertainty $\Delta G$ can be expressed as:

$$\Delta G = \sqrt{\left(\Delta g_1 \frac{\partial f}{\partial g_1}\right)^2 + \left(\Delta g_2 \frac{\partial f}{\partial g_2}\right)^2 + \ ... \ + \left(\Delta g_n \frac{\partial f}{\partial g_n}\right)^2} \tag{3.13}$$

The uncertainty of the derived quantity is thus a function of the uncertainties of the primary measurement and of the definition of the derived quantity itself, expressed by the function $f$. For the present case, this approach was employed to evaluate the uncertainty of all the derived quantities of interest, namely Reynolds number, Rotation Number and Nusselt number.

Considering Reynolds number, according to the definition of Equation 3.1 its value is given by geometric parameters, impingement mass flow rate and air properties. The uncertainty of the first is fixed and can be estimated around 0.7%. The accuracy of mass flow rate measurement depends upon the corresponding pressure drop across the calibrated orifices located downstream the five extraction plenums, and thus uncertainty increases as mass flow rate decreases. Moreover, also the accuracy of the measurement devices employed to precalibrate the orifices and the standard deviation of the calibration fit have to be considered. The combination of all of these parameters provides an uncertainty for impingement mass flow rate as high as 16% for the lowest investigated mass flow rate, while ranging from 4% to 8% for the other investigated conditions. Uncertainty in air properties, namely air dynamic viscosity, depends upon air temperature and can be estimated around 0.3%. The final uncertainty on Reynolds number, given by the three contributions, is almost totally dominated by the mass flow rate contribution, and thus ranges from 4% to 16% as Reynolds decreases.

Similar considerations can also be performed on the uncertainty of Rotation number, defined by Equation 3.4. In this case, also the uncertainty in rotational speed needs to be taken into account, which is maximum for lower $\omega$ values but never exceeds 0.4%. The combination of the various contributions shows that Rotation number is also dominated by the accuracy of mass flow rate value measurement: as a consequence, 16% uncertainty is obtained for the lowest mass flow and values ranging from 8% to 5% are recorded as mass flow rate increases.

Finally, if Nusselt number is taken into account it can be expected that the accuracy of such parameter is directly bound to the one of convective

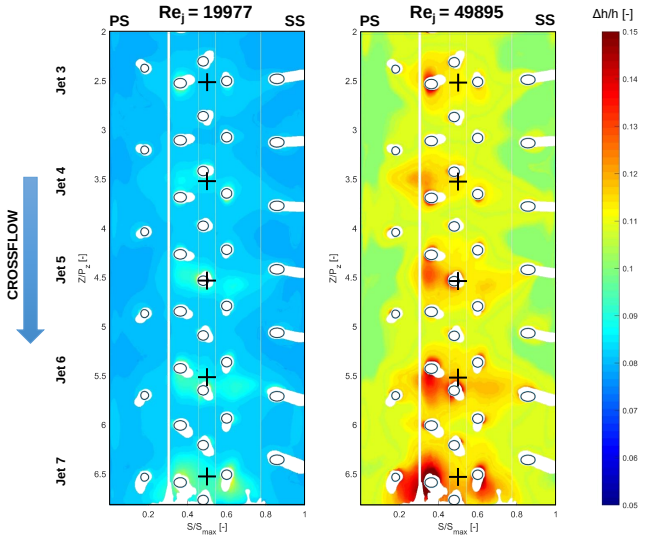


*Figure 3.21: Sample distributions of h uncertainty for different $Re_j$ values (GTE-A geometry, $Cr = 40\%$, $Ro_j = 0$).*

heat transfer coefficient $h$. Given the employed experimental technique and according to equation 2.7, it can be stated that the uncertainty of $h$ depends upon the contributions of air and initial temperatures, TLC event temperature and time and material properties. In the present case, the combined accuracies of temperature measurements lead to higher uncertainties for $h$ for the tests performed with lower temperature differences, i.e. with higher Reynolds numbers (see Section 3.3.1). On the other hand, the relative uncertainty in event time increases as event time decreases, i.e. as $h$ value increases. Finally, the uncertainty of material properties is constant and can be estimated to be around 5% [106]. The sample uncertainty distributions reported in Figure 3.21, obtained by applying Equation 3.13 to every point of the heat transfer surface, allow to appreciate these dependencies: lower uncertainty levels are recorded for the test performed at a lower $Re_j$ value (due to the temperature contribution) and within each test, the highest uncertainties are observed

in the heat transfer peaks (due to the event time contribution). For the present case, the uncertainty calculation is directly implemented in the *HTCvalue* code. The uncertainty on $Nu$ closely follows the corresponding one for $h$: maximum uncertainty is recorded for the highest $Re_j$ tests and can be as high as 16% locally and 11.7% in average terms, while typical average values for the other tests range from 9% to 11%. A more detailed analysis of the uncertainty evaluation applied to Equation 2.7 is reported in Appendix A.
An overview of the uncertainty values associated with the different quantities recorded during this work is reported in Table 3.4.

*Table 3.4: Uncertainty of the main recorded quantities (values reported with 95% confidence level).*

| | **Variable** | **Uncertainty** | **Units** |
|---|---|---|---|
| $D_j$ | Hole diameter | 0.1 | $mm$ |
| $T$ | Temperature | 1.35 | $K$ |
| $p$ | Pressure | 7-51 | $Pa$ |
| $\dot{m}_{IMP}$ | Impingement mass flow rate | 4%-16% | - |
| $Re_j$ | Reynolds number | 4%-16% | - |
| $Ro_j$ | Rotation number | 5%-16% | - |
| $Nu$ | Nusselt number | 9%-12% | - |

# Chapter 4

# Numerical analysis

The outcomes of the experimental campaign performed in this work, which will be presented in Chapter 5, allow to completely determine the heat transfer characteristics on the surface of interest, as well as to relate them to different geometric and flow parameters. Even so, such results only allow to hint the underlying fluid phenomena which actually determine the obtained heat transfer distributions. As a consequence, a parallel computational investigation of the present case has been carried out, simulating the most relevant outcomes of the experimental campaign. In this way a complete comprehension of the results is obtained, as well as additional and detailed information on the corresponding flow and thermal phenomena.
In this chapter, a brief introduction to flow numerical study will be presented, as well as a short discussion on turbulence and its modelling, given its outstanding relevance in the framework of this investigation. Finally, the numerical setup employed in this work and the investigated conditions will be presented.

## 4.1 Computational fluid dynamics

The experimental analysis is able to provide reliable information on thermal and fluid physical processes, since the actual phenomenon is

directly observed and measured. Even so, such approach presents evident limitations: it is often not possible to perform tests on the actual hardware, thus scaled up and often simplified models need to be employed. Moreover, only a limited number of physical quantities can be measured, thus making a full comprehension of the phenomena challenging to obtain. Finally, experimental uncertainty may reduce the confidence in the obtained results. Such issues could be avoided if the underlying physics governing the phenomenon could be cast in a mathematical form and then solved. In this way, a model of the phenomenon would be obtained, which could be able to describe its behaviour in any location and time. Following this approach, Computational Fluid Dynamics (CFD) was developed, whose aim is to solve the governing equations of flow and thermal phenomena by means of computational resources. The main advantages of CFD include the availability of complete and detailed information on the phenomenon and the ease in analysing different geometries and boundary conditions. On the other hand, the direct solution of the governing equations is usually too expensive in terms of computational resources, thus the employed mathematical model is often based upon hypothesis and simplifications: as a consequence, computational results need to be validated through the comparison with the experimental ones, in order to assess the capability of the model to describe the actual physical behaviour. Given these considerations, it is evident that experimental and numerical investigations have to coexist and interact: a full interpretation of the experimental results can be achieved thanks to the computational outcome, while the validity of the latter is provided by the first ones.

### 4.1.1 Turbulence modelling

In most of the cases of engineering interest, including the present one, a turbulent flow is employed. In these cases, the physics of fluid motion becomes extremely unsteady, with a continuous development, transport and destruction of flow structures over a wide range of length and time scales. Such behaviour is very challenging in terms of fluid analysis and simulation: in fact, turbulent flows are still described by Navier-Stokes

equations, but in order to describe the phenomenon their solution needs to be computed over the whole range of scales, which is in general extremely costly and difficult [107]. To overcome this issue, all or a part of the turbulent behaviour can be taken into account by means of analytical models, reducing the amount of flow structures being solved and thus the computational effort.

A reasonable tradeoff between flow resolution accuracy and computational cost is usually provided by *Scale Resolving Simulation* (SRS) models, according to which the largest turbulence scales (energy carrying range) are solved while the smaller scales are modelled. The rationale behind such choice is that, contrary to the large eddies, the smallest turbulence scales are isotropic and their behaviour is universal: as a consequence, their effect on the large scales structures can be represented by a suitable model. SRS models are particularly suitable for those engineering cases taking advantage from the solution of at least a part of the turbulent spectrum: this is particularly significant for unsteady or highly separated flows, as well as when turbulence driven phenomena need to be investigated (e.g. acoustics, fluid-structure unsteady interactions, vortex cavitation, etc) [108].

If scale resolution is applied to the whole computational domain, the *Large Eddy Simulation* (LES) approach is obtained. In this case, the separation between solved and modelled scales is obtained by applying a high pass filter to the Navier-Stokes equations, which performs a spatial average of the variables based on a local length: the scales lying below the filter length are modelled, while the other are solved.

Even if LES is the most widely applied SRS model over the years, its application becomes particularly demanding when dealing with wall-bounded flows. In fact, if $y$ is the wall normal distance the turbulent length scale $l^*$ of the largest eddies close to a wall is directly proportional to $y$ itself. As a consequence, the dimension of even the largest eddies becomes increasingly small approaching the wall, and thus their solution requires high resolution in space an time. The minimum value of $l^*$ which needs to be solved is provided by the existence of the *viscous* or *laminar sublayer*, in

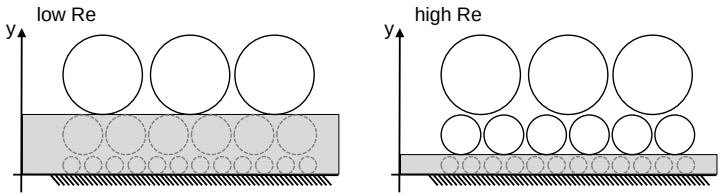


*Figure 4.1: Scheme of turbulent structures (circles) relation with viscous sublayer (gray region) at different Reynolds numbers [108].*

which molecular viscosity dampens flow turbulence. Even so, the thickness of the viscous sublayer decreases as flow Reynolds number increases, and so does the dimension of the smaller turbulent structures, as depicted in Figure 4.1: this makes wall-bounded flow resolution with LES approach prohibitively expensive even for moderate Reynolds number values. LES also requires that the turbulent boundary conditions at the inlets of the domain are accurately defined [109], which is usually challenging to achieve. These issues actually hinder the application of LES to most flows engineering interest.

In an attempt to maintain the accuracy of LES while limiting the computational cost to an affordable level, hybrid RANS-LES models were developed, which allow to apply the scale resolution to those regions where instability occurs and to cover the remaining part of the domain with a RANS approach. The combination of these methods is made possible by the fact that both approaches model the unresolved turbulent scales with an eddy viscosity: as a consequence, the conservation equations can operate in RANS or LES mode only according to the magnitude of such parameter provided by the turbulence model [108].

A commonly used hybrid approach is the *Detached Eddy Simulation* (DES) firstly proposed by Spalart [110], whose aim is to cover the boundary layer with a RANS solution and automatically switch to a LES approach in the detached regions of the flow. In this case, the switch is triggered by the comparison between the grid dimension and the turbulence length $l^*$: if the grid refinement is sufficient to solve the turbulent structures, a

LES solution is performed, otherwise RANS is employed. The reduction in computational cost is mainly achieved thanks to the RANS solution of wall-close regions, where the small $l^*$ value does not activate the switch. The possibility to obtain a real LES solution by simply refining the computational grid is one of the most desirable features of DES approach. Even so, a preliminary knowledge of the phenomenon is necessary to apply such approach, in order to determine where the grid should be refined. Moreover, the dependency of the local approach from the grid size may cause the activation of LES resolution in regions where the grid refinement is not sufficient (thus determining "gray zones" where the RANS solution is impacted) or directly inside the boundary layer (resulting in the so-called grid induced separation). Even if the latter issue is strongly reduced by recently developed formulations (like Delayed DES, DDES), DES approach is still more suitable for locally unstable flows, where the regions of flow separation are clearly known and defined. A higher flexibility with respect to DES is obtained by the *Scale Adaptive Simulation* (SAS) approach. SAS method, which was firstly introduced by Menter and Egorov [111] starting from the considerations perfromed by Rotta in the development of $k$-$kL$ model [112, 113], is an improved URANS formulation which allows the resolution of the turbulent spectrum in unstable flows [114]. This goal is achieved by the introduction of the von Karman length scale $L_{vK}$ in the source term of the turbulence scale equation:

$$L_{vK} = \kappa \left| \frac{\overline{U}'}{\overline{U}''} \right|, \quad \text{with} \quad \overline{U}' = \sqrt{\frac{\partial \overline{U}_i}{\partial x_j} \frac{\partial \overline{U}_j}{\partial x_i}} \quad \text{and} \quad \overline{U}'' = \sqrt{\frac{\partial^2 \overline{U}_i}{\partial x_j^2} \frac{\partial^2 \overline{U}_j}{\partial x_k^2}}, \tag{4.1}$$

where $\kappa$ is a constant, $U$ is the flow velocity, $x$ is the generic coordinate and overlines indicate the averaging operation. The definition of $L_{vK}$ includes the second velocity gradient, which is sensible to inhomogeneous and unstable velocity profiles. In fact, unsteady flow vortex structures are associated with a spatial variation of the local strain rate, which is given to first order by the von Karman length scale [114]. This parameter can thus be employed in order to identify the unstable regions, thus

reducing the eddy viscosity and obtaining a LES-like resolution only when required by the flow physics. Such approach, which adapts the length scale to the resolved turbulent structures (hence the name of the model), can be implemented in any two-equation turbulence model through an appropriate modification of the scale defining equation. The SAS version included in ANSYS Fluent (and employed in the present work) is built upon the robust $k$-$\omega$ SST model, and the scale resolving capabilities are obtained by including an additional production term $Q_{SAS}$ in the specific dissipation $\omega$ transport equation [114]. The quadratic ratio of turbulent length scale and von Karman scale ($l^*/L_{vK}$) is included in $Q_{SAS}$: since $L_{vK}$ is smaller for an unsteady velocity profile [115], the aforementioned ratio increases, augmenting the production of $\omega$ and thus reducing the eddy viscosity $\mu_t = \overline{\rho}k/\omega$ [116]. A significant advantage of this approach is that the performance of SST model is not affected in the stable flow regions: as a consequence, since the RANS part of the model is not influenced by the grid spacing, the typical issues of DES approach (namely grid induced separation and "gray zones") are avoided. This results in a more robust behaviour with respect to DES, which allows to employ SAS on a much wider range of computational grids. On the other hand, LES-like turbulence solution in SAS needs to be activated by the flow itself: as a consequence, if flow unsteadiness is not strong enough to trigger the switch from RANS to LES the model can produce steady solutions even where a scale resolution is desired. As a consequence, SAS approach is more suitable for globally unstable flows (i.e. flows with strong instabilities and interactions) [108].
Since the present case falls within this latter class of phenomena, SAS approach was considered to be particularly suitable in order to obtain a detailed resolution of flow field, and was thus applied in the corresponding numerical investigation.

## 4.2 Numerical setup

In this section, the investigated conditions as well as the numerical methods employed for their simulation will be presented.

### 4.2.1 Investigated conditions

In this case the aim of the numerical analysis is to provide a deeper comprehension on the underlying phenomena driving heat transfer: as a consequence, the test conditions to be simulated were defined by selecting the most relevant and interesting effects emerged from the experimental outcomes, which will be presented in Chapter 5. In particular, the unique heat transfer pattern and the large influence of extraction holes observed for GTE-A deserved a deeper analysis, which was carried out by simulating the test point corresponding to $Re_j \simeq 30000$ and $Cr = 40\%$ in static conditions. Moreover, in order to highlight the effects of rotation, the same test point was also simulated in rotating conditions. Finally, interesting phenomena were also observed for GTE-C hole arrangement, which was thus simulated in static conditions with $Re_j$ around 20000 and $Cr = 40\%$. Since the test points considered for GTE-A and GTE-C employ similar mass flow rate values (corresponding to an equivalent slot Reynolds number $Re_b$ of around 8200) a direct comparison was also achievable between the numerical outcomes of the two cases, in order to better understand the effects of holes diameter, number and arrangement.

### 4.2.2 Numerical methods

In order to identify the accuracy required to obtain a proper simulation of the present case, simulations were run using both a RANS turbulence modelling ans a scale resolving approach. In particular, the $k$-$\omega$ SST model was selected for the RANS simulation, embodying one of the best compromises between accuracy and computational cost for LE impingement problems (see Section 1.4). On the other hand, SAS model was chosen to perform scale resolving analysis, given its robustness and suitability to globally unstable flows (see Section 4.1.1).

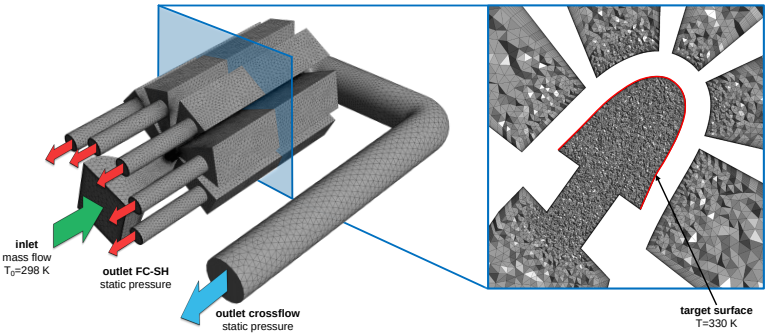


*Figure 4.2: Computational domain and boundary conditions.*

The computational domain, together with the employed boundary conditions, is presented in Figure 4.2. The domain includes the radial feeding channel, the impingement holes, the LE cavity, the extraction holes and the corresponding plena and the various outlet ducts (both extraction and crossflow ones). The only difference between GTE-A and GTE-C domains consists in the impingement holes section. ANSYS meshing was employed to generate the computational grids for both geometries. As shown in Figure 4.2, leading edge cavity was discretized with a finer grid in order to achieve a higher resolution in this region, while a coarser mesh was employed to model the remaining part of the domain. Following this criterion, an unstructured tetrahedral mesh of $7.7 \cdot 10^6$ elements was built for RANS simulations of both geometries, with an element sizing of 1.5 *mm* in the impingement region. On the other hand, SAS computations were carried out on finer grids of $20 \cdot 10^6$ and $25 \cdot 10^6$ elements for GTE-A and GTE-C respectively, obtained by adopting a smaller elements sizing (0.8 *mm* in the LE cavity). In both RANS and SAS grids the near wall region was covered with 20 prismatic layers, in order to achieve a proper resolution of boundary layers.

Mesh sizing was defined keeping in consideration previous works performed on similar test cases [77] and according to the considerations presented by

Celik et al. [117], which suggest to adopt a grid resolution based on the local values of turbulence Reynolds number and of Kolmogorov length scale for a proper scale resolving simulation. This criterion was applied for the definition of all the numerical grids employed for SAS simulations. In order to assess the reliability of such approach, a mesh sensitivity analysis was also carried out for the baseline case (GTE-A geometry in static conditions). In particular, a coarser mesh was defined, increasing the element size of 1.5 times in the leading edge region (where scale resolution is desired) and leaving the sizing of the other regions unchanged: this provided a mesh of $9.1 \cdot 10^6$ elements. A simulation was thus carried out using this grid, using the same settings as the finer mesh and only using a different time step ($7 \cdot 10^{-6}$ $s$) in order to have similar values of Courant number in the two simulations. The Nusselt number distributions obtained for the two simulations, time averaged over the same total time, are reported in Figure 4.3 together with the experimental outcome, all scaled with respect to the area averaged value $\overline{\overline{Nu}}$. On the other hand, in Figure 4.4 the streamwise averaged heat transfer results are compared for the two mesh refinements.

Figure 4.3 shows that the two computational grids provide very similar results in qualitative terms, with only slight discrepancies in secondary peaks and jet shape, and both of them reasonably predict the experimental pattern. The outcomes are also very similar from the quantitative point of view, as shown by Figure 4.4: in fact, the maximum local difference on line averaged $Nu$ values is around 5%. As a consequence of the previous considerations, it can be stated that the results obtained with the employed computational grid are not affected by the mesh sizing itself, and thus that the employed sizing criterion is suitable for the present case.

As regards near-wall treatment, an automatic blending approach between Wall Function and Wall Integration depending on the local $y^+$ value was employed. Even so, in the present case $y^+$ values lower than unity are achieved on the whole jet target surface, thus the Low Reynolds formulation is always recovered in this region.

The same boundary conditions were selected for all the simulations, with

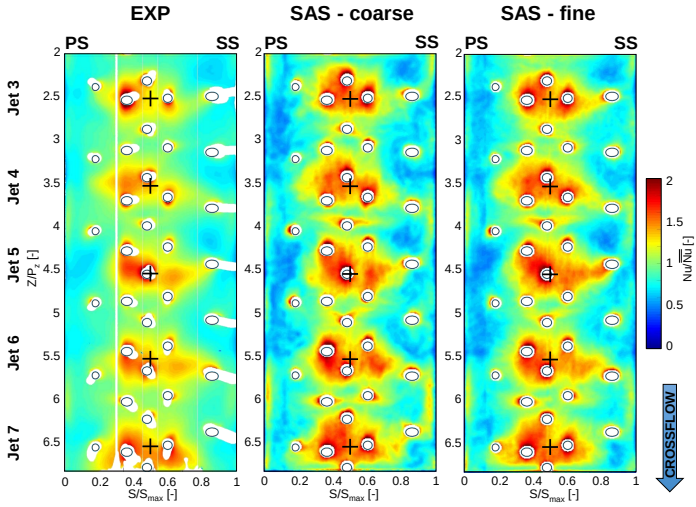


*Figure 4.3: $Nu/\overline{\overline{Nu}}$ distributions for static GTE-A test.*

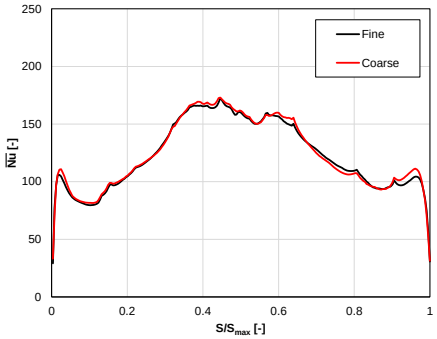


*Figure 4.4: Spanwise $\overline{Nu}$ distributions for static GTE-A test for the two mesh refinements.*

the exception of rotational speed. Mass flow rate value was imposed at the inlet section, together with top-hat profiles of velocity and total temperature (the latter being equal to 298 $K$ according to the experimental

conditions). A free-stream turbulence level of 5% was also imposed in this section according to the assumption of uniform velocity and low turbulence, which represents a consistent hypothesis considering the presence of the mesh heater and the downstream convergent section. Static pressure outlet condition was adopted for all the outlet sections, whose value was adjusted in order to obtain the same mass flow split employed for the experiments. A constant temperature of 330 $K$ was imposed on the jet target surface, according to the fact that the transient technique employed in the experiments approximates an isothermal wall situation at each time instant [118]. All the other walls are considered as adiabatic. All surfaces are modelled as smooth with no-slip condition applied. Concerning fluid properties, since low Mach number values are present in every point of the domain and the flow undergoes negligible temperature variations, air is treated as incompressible with constant properties.

As regards the employed numerical schemes, in RANS simulations a second order upwind scheme is adopted for spatial discretization and a least square cell-based method is employed for gradient calculation. In the SAS simulations a bounded central difference scheme is adopted for spatial discretization and a second order implicit formulation is applied for time discretization. A time step of $5 \cdot 10^{-6}$ $s$ was employed in all the unsteady simulations in order to maintain a Courant number lower than unity, and for each time step 7 sub-iterations were performed, with the aim to achieve adequate residual values. In particular, the number of sub-iterations has been derived from a sensitivity analysis: further increasing the number of sub-iterations did not provide a significant decrease of the residuals. In particular, residuals drop of an order of magnitude for the continuity equation, while for the three momentum equations and for energy equation the decrease is of two orders of magnitude. Transient statistics were collected over a a total time of 0.1 $s$, in order to ensure and adequate number of flow-through times through the impingement cavity (around 50-60 passages depending on the geometry).

# Chapter 5

# Experimental results

In this chapter the outcomes of the experimental campaign will be presented: the obtained heat transfer distributions will be analysed, as well as the effect of the different investigated phenomena, for each of the three impingement geometries. A direct comparison between such geometries will also allow to reveal the effects of different holes arrangements and diameters, in order to determine which one provides the best cooling performance.

## 5.1 GTE-A results

This section reports the heat transfer results obtained with GTE-A geometry. In order to improve the relevance of such results, the evaluated $h$ values on the jet target surface are recast in a dimensionless form as Nusselt number using the impingement hole diameter $D_j$ as reference length:

$$Nu = \frac{hD_j}{\lambda} \tag{5.1}$$

where $\lambda$ is average air thermal conductivity during the test. $Nu$ distributions obtained in static and rotating conditions are reported in Figures 5.1 and 5.2 respectively.

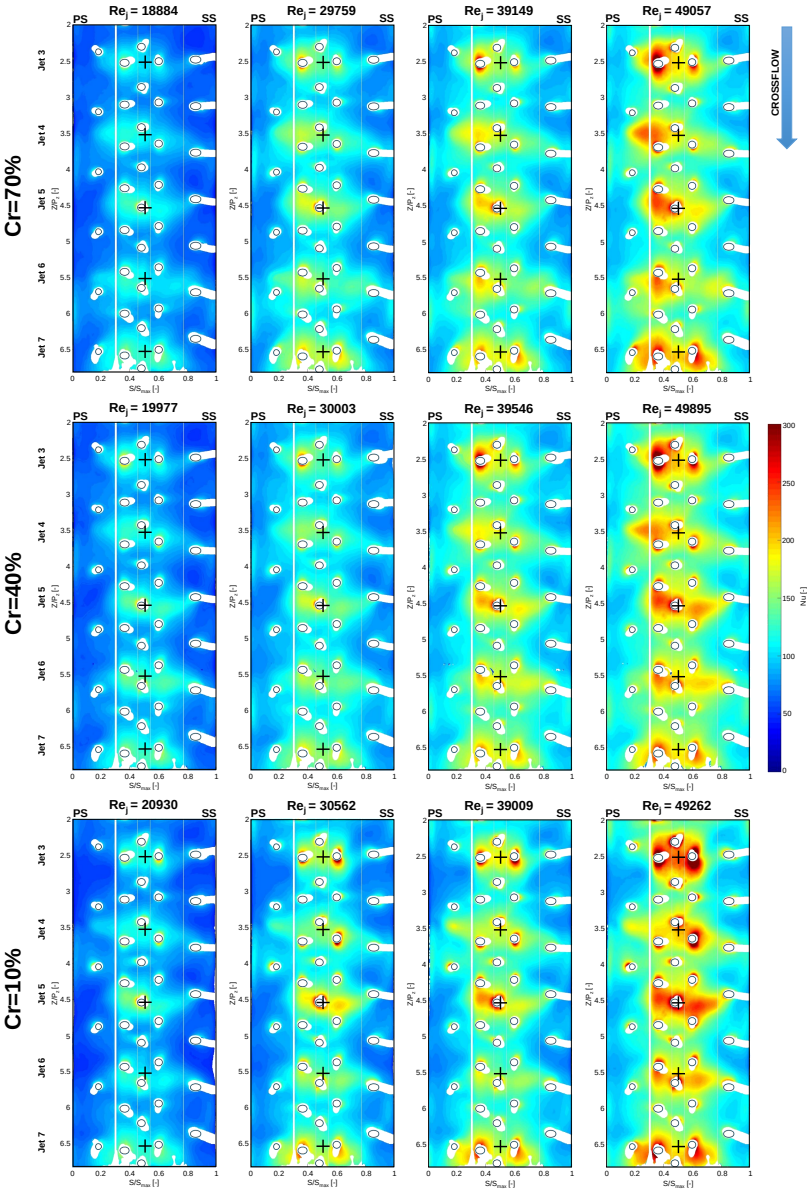


*Figure 5.1: Nu distributions for GTE-A geometry in static conditions ($Ro_j = 0$).*

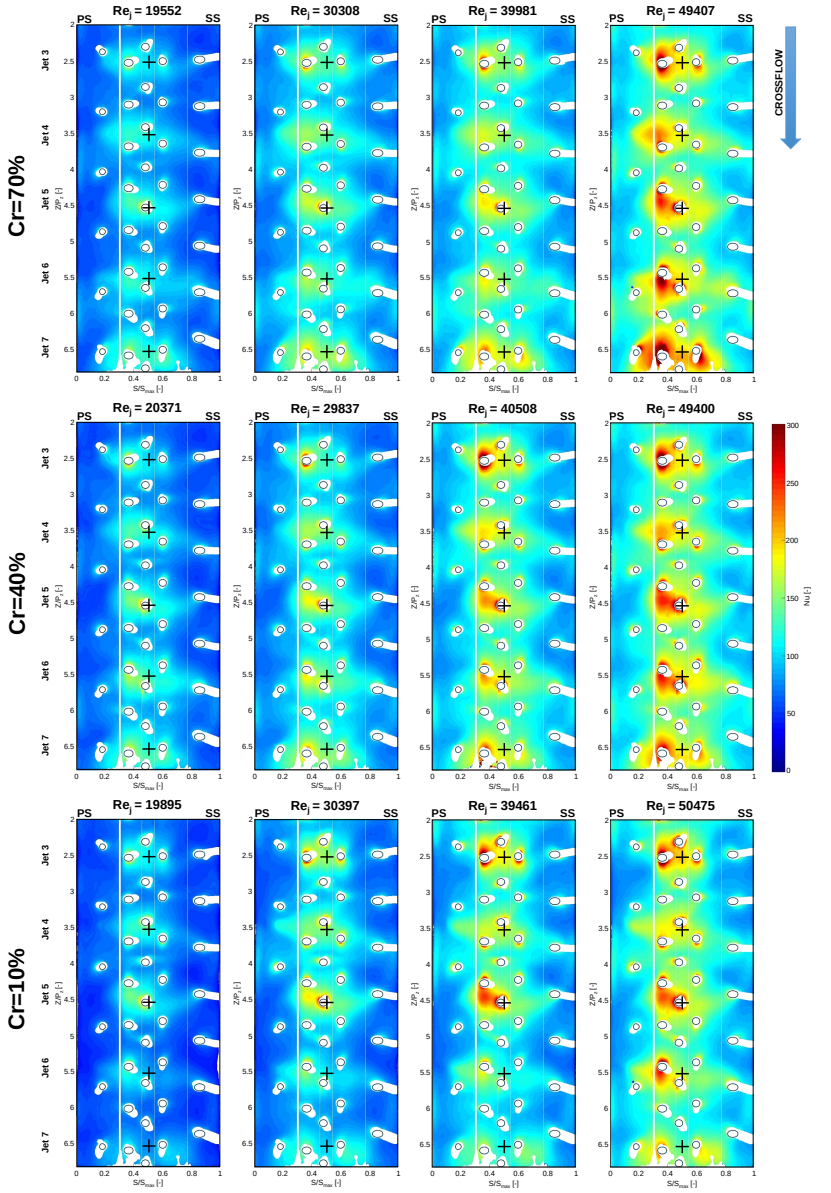


*Figure 5.2: Nu distributions for GTE-A geometry in rotating conditions ($Ro_j = 0.008$).*

For a better representation, in Figures 5.1 and 5.2 the leading edge inner surface is unrolled on a flat plane: vertical coordinate $Z$ is aligned along the radial direction and is scaled with respect to the jet-to-jet radial spacing $P_z$, while horizontal coordinate $S$ represents the distance along the surface itself from its extremity closer to the pressure side, and is scaled with respect to the total surface span $S_{max}$. The $Z$ direction will also be referred as *streamwise*, while the $S$ direction as *spanwise*. The traces of extraction holes are reported in solid line, while cross symbols mark the intersection between the surface and the axis of each jet, i.e. the ideal jet stagnation point. Some regions are excluded from the analysis and are reported as white areas: these include regions where measurement was either not possible (i.e. areas covered by the extraction holes or with optical disturbances) or unreliable (namely close to the extraction holes, where one-dimensional heat transfer hypothesis is not verified). Jets are numbered increasingly in the radial outward direction (i.e. jet 1 is at the inner radius and jet 7 at the outer radius). For the present case, the results will be presented for jets 3-7 ($2 \leq Z/P_z \leq 7$), since these are not affected by boundary effects.

Nusselt number distributions reveal that each jet generates a single region of high heat transfer, which is located close to the jet stagnation point but whose shape is strongly influenced both by the target surface curvature and by the extraction holes presence and location. In particular, all the heat transfer peaks present a horizontally elongated shape, which reveals that jet impingement occurs not only in the central part of the curved surface (close to the stagnation point) but also on the side walls (corresponding to the regions having $S/S_{max} < 0.3$ and $S/S_{max} > 0.7$). The distributions also reveal that the extraction holes have a relevant effect on the internal flow field: such holes seem to be able to drive the impingement jets, resulting in a distortion of the heat transfer pattern towards the closer holes. This phenomenon appears to be strong enough to generate secondary heat transfer peaks: an example of this can be noticed for static tests on the suction side of jets 5 and 6, as highlighted in Figure 5.3. The geometric features of the system allow to highlight the

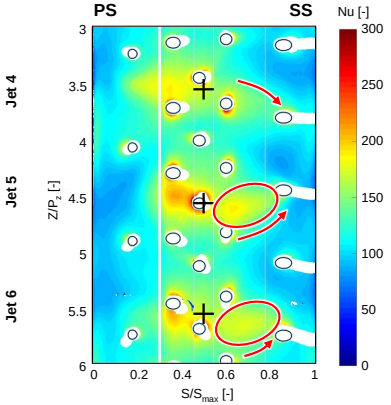


*Figure 5.3: Example of extraction driven distortions and secondary peaks ($Cr = 40\%$, $Re_j \simeq 40000$, $Ro_j = 0$).*

effects of extraction holes: in fact, in this case the relative arrangement of impingement and extraction holes is different for each jet, which results in strongly different heat transfer pattern shapes. Such a strong influence can be attributed to the large number and relevant diameter of extraction holes. Secondary heat transfer peaks can also be noticed surrounding each extraction hole. The phenomena causing such a unique heat transfer pattern, which are challenging to identify relying on the sole experimental analysis, will be presented in Chapter 6 thanks to the computational outcomes.

Additional considerations can be performed if spanwise distributions of averaged $Nu$ are considered for different $Re_j$ nominal values, a sample of which is reported in Figure 5.4. The data reported in such figure is obtained by line averaging $Nu$ values along the $Z$ direction for the various spanwise locations. The charts show that the lateral spreading of the heat transfer peaks generates a plateau-like distribution on the central part of the leading edge ($0.3 < S/S_{max} < 0.7$), with almost constant heat transfer values. Moving away from the central region, an almost linear decrease of heat transfer is recorded towards the side walls, with average $Nu$ values up to 40% lower than the central ones.

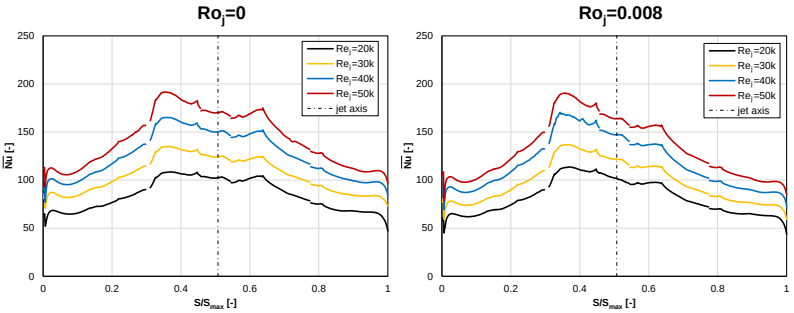


*(a)* *(b)*

*Figure 5.4: Line averaged $Nu$ spanwise distributions for GTE-A geometry with $Cr = 40\%$ in static (a) and rotating (b) conditions.*

### 5.1.1 Effect of Reynolds number

The maps of Figures 5.1 and 5.2 and the distributions of Figure 5.4 also allow to appreciate the effect of jet Reynolds number: for a given value of crossflow ratio and Rotation number, an increase in $Re_j$ seems to increase heat transfer in every location, but without any significant alteration of the heat transfer pattern shape.

The relation between heat transfer and jet Reynolds number can be quantified if the area averaged $Nu$ values are plotted as a function of $Re_j$, which is performed in Figure 5.5 for all the static tests. In this case, the analysis of the data reveals that, for all the investigated conditions, area averaged $Nu$ are a close function of $Re_j^{0.6}$: similar exponent values for the Reynolds dependency were found in many different works performed on similar test cases available in the open literature [44, 119].

In order to further validate the data presented in this investigation, the correlation derived by Chupp et al. [43] was applied to the present case: in fact, even if such correlation does not consider the effect of coolant extraction and supply condition, it was derived from a geometry similar to the present case (single row of round jets impinging on a concave surface). The outcome of the correlation is also reported in Figure 5.5: it is evident

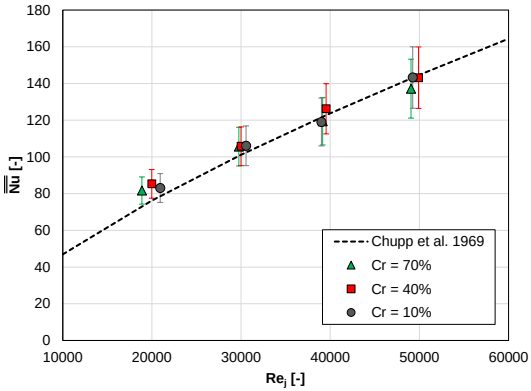


*Figure 5.5: Area averaged $Nu$ values for GTE-A geometry in static conditions ($Ro_j = 0$).*

that a good agreement is present between the calculated and the measured data, with differences generally lower than 10% despite the underlying differences in geometric and boundary conditions.

### 5.1.2 Effect of crossflow condition

The effects of different jet supply conditions, i.e. of different blade radial sections, on heat transfer can be evaluated by comparing the heat transfer distributions obtained for different values of crossflow ratio, which is performed in Figure 5.6 for static tests performed at a nominal $Re_j$ value of 40000. Since the actual $Re_j$ value may vary slightly in between different tests and the effect of such parameter on heat transfer is particularly strong (as seen in Section 5.1.1), in this case the local $Nu$ values have been scaled with respect to the corresponding $Re_j$, thus removing its effect from the data.

The reported $Nu$ distributions reveal that a higher crossflow (i.e. moving from the tip to the hub of the blade) promotes the jet lateral spreading: high heat transfer regions on the side walls tend to expand in size and magnitude (e.g. on the pressure side of jet 4) and a shift of the secondary

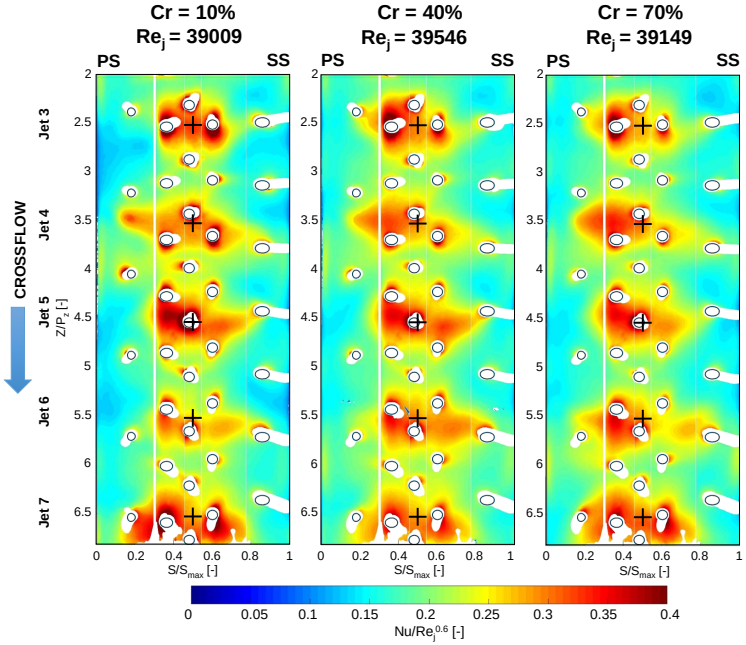


*Figure 5.6: $Nu/Re_j^{0.6}$ distributions for GTE-A geometry in static conditions ($Ro_j = 0$) for different crossflow values.*

peaks towards the edges of the surface can be observed (e.g. on the suction side for jet 6). At the same time, a slight decrease of heat transfer values can be noticed close to the jet stagnation points. These effects can also be observed if line averaged heat transfer values are considered for the three distributions, which is performed in Figure 5.7: as crossflow increases, heat transfer increases on the suction side ($S/S_{max} < 0.3$) and decreases in the central region ($0.3 < S/S_{max} < 0.7$), while a clear trend is not possible to identify on the suction side ($S/S_{max} > 0.7$).

A possible explanation of this phenomenon is reported in Figure 5.8. With a low crossflow, i.e. close to the blade tip, the flow velocity inside the supply channel is small, and the jet feeding condition is similar to a plenum: the flow enters the impingement holes with a low residual

component of radial momentum, and thus the apparent hole passage section is almost circular. On the other hand, when the crossflow is high the flow enters the impingement jets with a strong component of radial momentum, which drives the flow along the downstream side of the impingement hole: the apparent passage section is thus reduced, increasing the jet velocity. It can also be expected that the shape of such apparent section becomes more elliptical than circular: if the hole length is small (i.e. low $L/D_j$ value), the jet will likely retain this shape, resulting in an enhanced lateral spreading with respect to a lower crossflow situation. Despite its strong effects on heat transfer pattern shape, this phenomenon seems not to influence area averaged heat transfer values in a significant way, as reported in Figure 5.5.

A similar phenomenon, both in terms of local and overall effects, was already observed by Andrei et al. [57] and Massini et al. [58], despite the different hole shape (racetrack instead of circular) and inlet condition (filleted instead of square-edged). On the other hand, the obtained results are in contrast with the outcomes of Jordan et al. [47, 55], which found an upstream crossflow to significantly deflect the impingement jets and to decrease heat transfer also for square edged holes. Even so, a higher

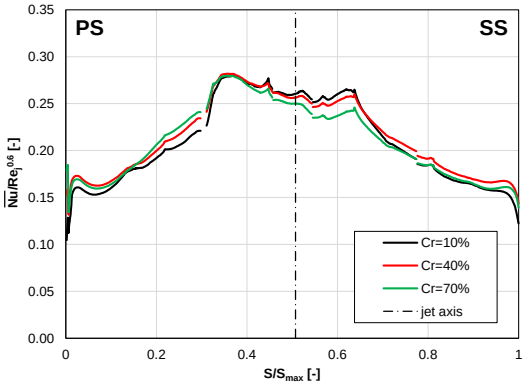


*Figure 5.7: Line averaged $Nu/Re_j^{0.6}$ distributions for GTE-A geometry in static conditions ($Ro_j = 0$) for different crossflow values.*

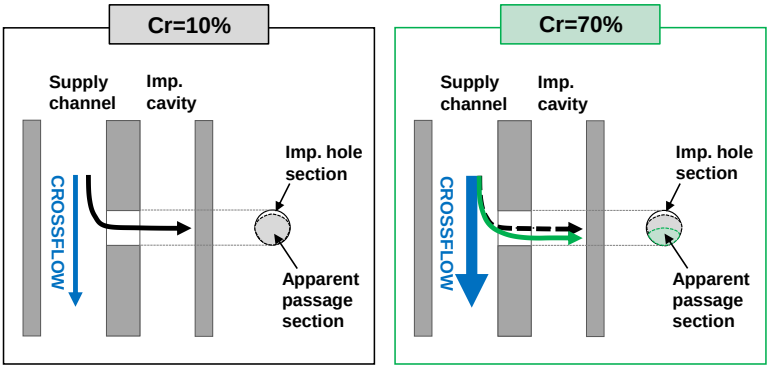


*Figure 5.8: Scheme of the possible phenomena related to different crossflow situations.*

jet-to-target plate distance with respect to the present case was employed in these studies (4 diameters instead of 2.5) and, most important, with a wide semi-circular target surface (rather than wedge-shaped). It can thus be expected that in the studies of Jordan et al. there is more room for the jet to develop in the radial direction with respect to the present case, while the wider target surface is likely to reduce the interaction of the jets with the side walls, which is a significant contribution in the present case.

### 5.1.3 Effect of rotation

In order to highlight the effect of rotation on heat transfer, $Nu/Re_j^{0.6}$ distributions obtained for a nominal $Re_j$ value of 20000 and for $Cr$=40% are reported in Figure 5.9.

As a general consideration, it can be noticed that rotation seems to reduce the jet lateral spreading: if a single jet is considered, the extension and the entity of high heat transfer regions decrease on the side walls, while peak magnitude generally increases in the central region. A possible explanation of this effect, which is verified for every investigated $Re_j$ condition, is reported in Figure 5.10. In this case, impingement jets are directed towards the blade pressure side: as a consequence, during rotation a Coriolis force $\vec{F}_{Co}$ is generated towards the inward radial

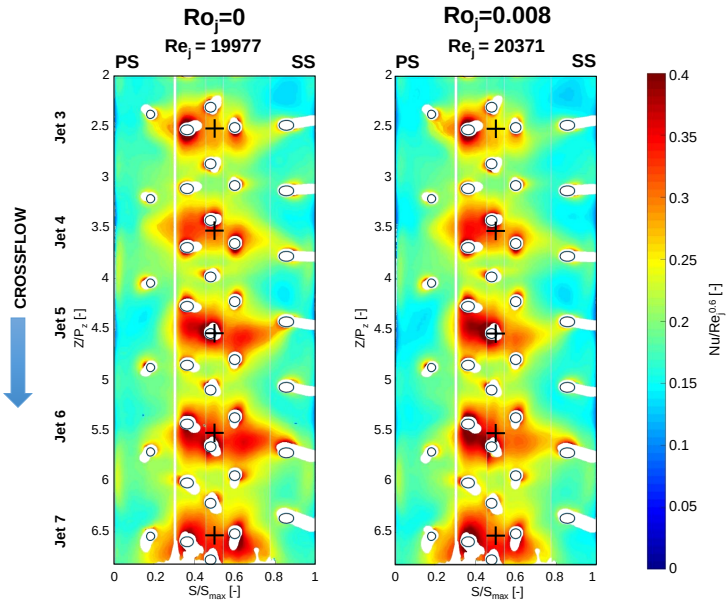


*Figure 5.9: $Nu/Re_j^{0.6}$ distributions for GTE-A geometry at $Re_j = 20000$, $Cr = 40\%$ in static ($Ro_j = 0$) and rotating ($Ro_j = 0.008$) conditions .*

direction. When the flow enters the impingement holes, it is thus subject to two opposite forces: the inertia force, which is bound to the feeding channel crossflow and tends to move the flow towards the outer radii, and the Coriolis force, which tends to drive it towards the inner radii. Rotation and crossflow effects are thus likely to interact: in particular, Coriolis force may balance a part of the residual radial momentum of the flow, recalling the jet core towards the inner radii and thus providing a more circular shape of the jet and reducing its lateral spreading. This interpretation is confirmed by the outcomes of the numerical analysis (see Chapter 6). The aforementioned phenomenon seems to occur in every crossflow condition, but its magnitude appears to increase as crossflow decreases, i.e. moving towards the tip of the blade. This can be verified by observing the $Nu/Re_j^{0.6}$ distributions of Figure 5.11, still obtained for $Re_j$ around 20000 but in $Cr$=10% conditions. In order to justify

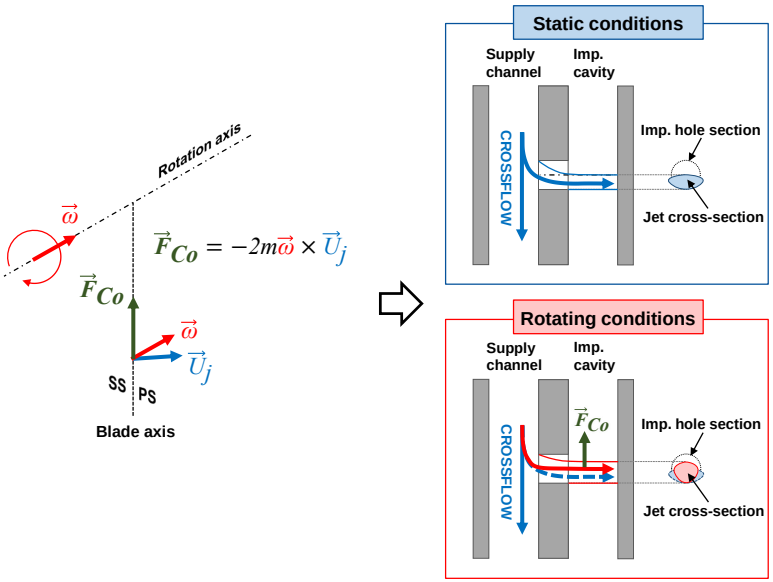


*Figure 5.10: Scheme of the possible phenomena inside the impingement hole related to rotation.*

such dependency of rotational effects upon the crossflow value, it can be considered that the residual radial momentum is likely to be proportional to the square of the supply channel velocity, while the magnitude of Coriolis force is equal in every crossflow condition. This leads the relative rotational effect to be maximum for tip supply conditions and almost negligible for hub conditions, which can also be appreciated from the corresponding $Nu$ distributions of Figures 5.1 and 5.2.

The distributions reported in Figure 5.11 also allow to notice a different phenomenon: in rotating conditions, heat transfer appears to progressively decrease from jet to jet moving along the crossflow direction, with a maximum reduction of around 20% for jet 7. This phenomenon is only verified for the tests performed with $Cr = 10\%$. An interpretation can be provided by considering that rotation also affects the flow inside the feeding channel: in particular, in rotating conditions a Coriolis force is generated, which tends to drive the flow along the pressure side [18] and

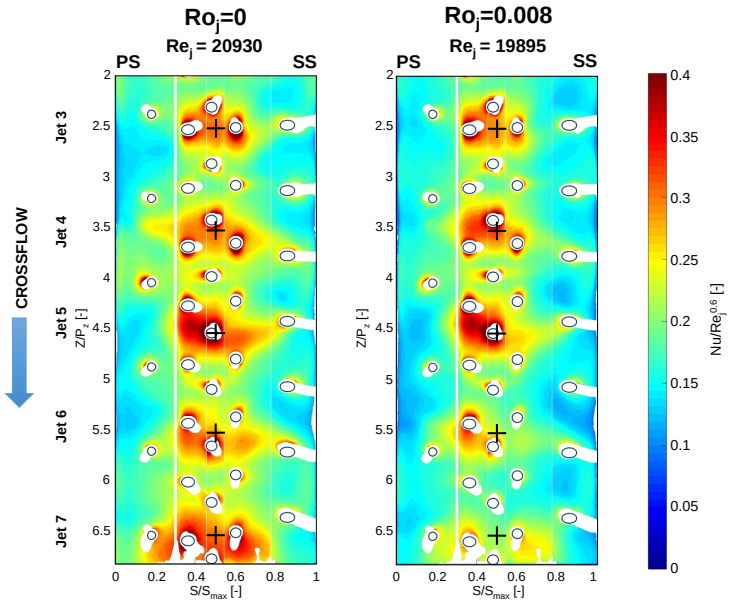


*Figure 5.11: $Nu/Re_j^{0.6}$ distributions for GTE-A geometry at $Re_j = 20000$, $Cr = 10\%$ in static ($Ro_j = 0$) and rotating ($Ro_j = 0.008$) conditions.*

may thus cause an uneven supply condition for the impingement jets [58]. This effect can be quantified if a rotation number is defined for the feeding channel:

$$Ro_{Cr} = \frac{\omega D_{h,Cr}}{U_{Cr}} \tag{5.2}$$

where $D_{h,Cr}$ and $U_{Cr}$ are feeding channel hydraulic diameter and flow velocity respectively. According to its definition, $Ro_{Cr}$ increases as $U_{Cr}$ decreases, i.e. as crossflow decreases and moving along the radial direction (due to the flow being drawn by the impingement holes). Rotational effects in the feeding channel can thus be expected to be maximum for the outer jets of $Cr = 10\%$ condition, where a $Ro_{Cr}$ value close to 0.2 is reached: in this case the maximum nonuniformity can be expected for jet supply, which is likely to disturb jet generation and thus heat transfer.

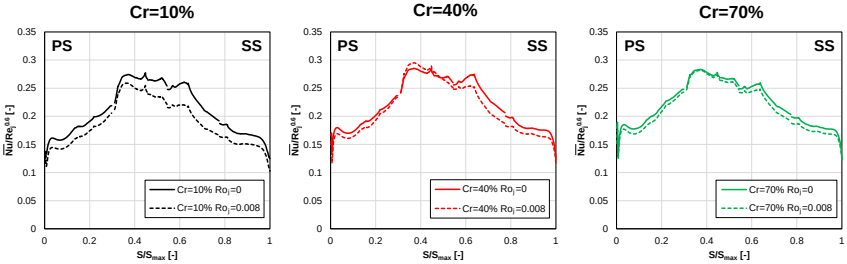


*Figure 5.12: Line averaged $Nu/Re_j^{0.6}$ distributions for GTE-A geometry at around $Re_j = 20000$.*

The combined effects of rotation can be appreciated by considering line averaged heat transfer distributions, which are reported in Figure 5.12 for the three crossflow conditions at around $Re_j$=20000. The charts show that for the minimum crossflow condition the combined Coriolis effects on the jet and on the supply channel lead to a general decrease in heat transfer, with local differences ranging from 8% to 18%. On the other hand, $Cr = 40\%$ situation presents lower heat transfer on the side walls in rotating conditions, but also approximately equivalent values in the central region. Finally, very small differences are recorded in $Cr = 70\%$ condition, with only slightly lower values for the rotating case.
A general quantification of the rotational effects can be obtained if the area averaged $Nu$ values are considered, which is performed in the charts

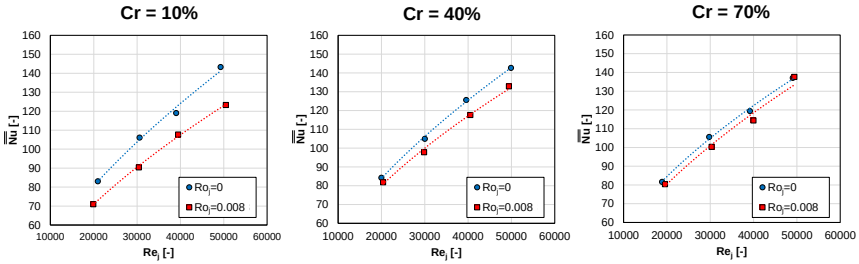


*Figure 5.13: Area averaged $Nu$ values for GTE-A geometry for different crossflow conditions.*

of Figure 5.13. This representation clearly shows the combined effects of rotation and crossflow. For $Cr = 10\%$ conditions a uniform decrease in heat transfer is observed, with a 13% average difference with respect to the static case. Such difference decreases to 6.0% with $Cr = 40\%$ and to an almost negligible 3.6% with $Cr = 70\%$.

### 5.1.4 Effect of extraction condition

In the present case, extraction condition seems to be able to significantly influence the heat transfer pattern. As reported in Section 3.1, in order to deepen the comprehension of such influence additional tests were performed by varying the mass flow split amongst the extraction rows. For geometry GTE-A, the two additional split conditions (All FC and

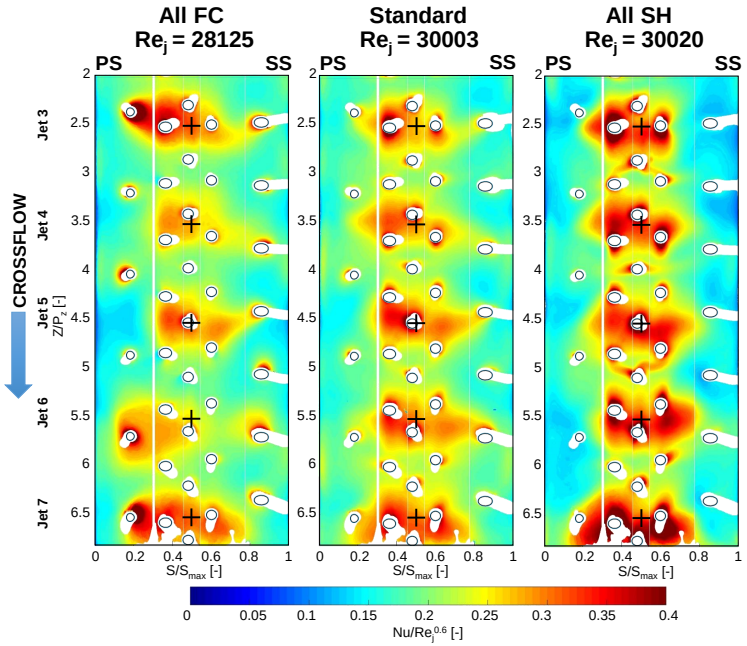


*Figure 5.14: $Nu/Re_j^{0.6}$ distributions for GTE-A geometry for different extraction conditions ($Cr = 40\%$, $Ro_j = 0$, $Re_j =\simeq 30000$).*

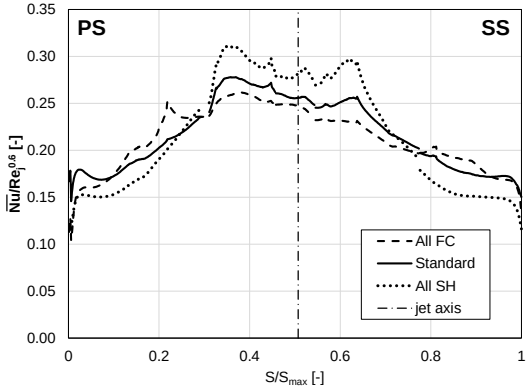


*Figure 5.15: Line averaged $Nu/Re_j^{0.6}$ distributions for GTE-A geometry for different extraction conditions ($Cr = 40\%$, $Ro_j = 0$, $Re_j =\simeq 30000$).*

All SH) were investigated for a single test point, corresponding to static conditions, $Re_j =\simeq 30000$ and $Cr = 40\%$. The obtained heat transfer distributions are reported in Figure 5.14, together with the corresponding outcome obtained with standard extraction layout

The three distributions confirm that GTE-A geometry is strongly sensible to extraction condition. In particular, when the coolant flow is completely extracted by the FC holes, the heat transfer peaks tend to shift towards the edges of the surface (especially for jets 3, 6 and 7), while their magnitude decreases with respect to the standard case. The opposite effect is obtained if the coolant flow is entirely extracted from the three central SH rows: wide regions of low heat transfer appear on the side walls, while the peak entity is strongly enhanced in the central region. Moreover, in this configuration a complex heat transfer pattern is generated: horizontally elongated secondary peaks appear midway between the impingement jets (clearly visible at $Z/P_z$ values around 3, 4 and 5) which can be interpreted as caused by a fountain type flow [35] and whose shape is strongly deformed by the closest extraction holes. If the two extreme cases are considered, local differences can be as high as 75%. In order to better quantify the extraction effect, the line averaged heat transfer values can

be considered (Figure 5.15).
The distributions allow to appreciate that for the All FC case a flatter heat transfer distribution is present with respect to the standard, bound to 6% higher heat transfer values on the side walls and 6% lower in the central region. On the other hand, the All SH case provides lower heat transfer values on the side walls and higher in the central region (both with a 12% difference with respect to the standard case). Despite the aforementioned considerations, the influence of extraction condition on area averaged heat transfer seems to be negligible: averaged $Nu/Re_j^{0.6}$ values range between 0.21 and 0.22 for each of the tree distributions.

### 5.1.5 Flow check results

Even if the rig is not equipped with detailed flow visualization devices, it is still possible to obtain significant information on the internal flow from the static pressure taps installed in different locations. In particular, pressure measurements upstream and downstream the impingement holes made it possible to evaluate the holes discharge coefficient $Cd$, whose values corresponding to the tests of Figures 5.1 and 5.2 are reported in Figure 5.16.
The $Cd$ values reveal that, unlike the heat transfer magnitude, the flow

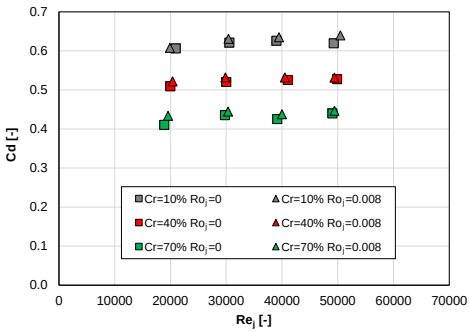


*Figure 5.16: Impingement holes discharge coefficient for GTE-A geometry.*

field is strongly affected by different crossflow conditions: reductions higher than 30% are recorded passing from $Cr = 10\%$ to $Cr = 70\%$, while $Cr = 40\%$ lies midway between the two extreme cases. This finding is consistent with results available in the open literature [120]: with a high upstream crossflow the flow needs to overcome a large turning angle in order to enter the hole, which causes a separation on the upstream side of the hole [121]. The size of the separation region determines the pressure losses, and thus the discharge coefficient values.

The other test parameters seem not to influence the discharge coefficient in a significant way. In particular, Reynolds number seems to have an extremely slight positive effect, while the consequence of rotation is unclear: therefore, it may be supposed that rotational effects on the impingement flow occur only downstream the hole inlet section.

## 5.2 GTE-B results

In this section the results obtained with GTE-B geometry will be presented. An overview of the outcomes in the different investigated conditions is provided in Figures 5.17 and 5.18, which report the $Nu$ distributions on the jet target surface in static and rotating conditions respectively. The employed notation is identical to GTE-A maps, and also in this case the region corresponding to the first two jets ($Z/P_z < 2$) is not reported due to boundary effects affecting the measurement.
The $Nu$ distributions reveal that in the present case a complex heat transfer pattern is generated, due to the interaction of impingement jets and extraction flow field. In particular, a high heat transfer region is present for each impingement jet, which is clearly oriented towards the pressure or suction side according to the position of the corresponding impingement hole. Moreover, the highest heat transfer values are usually recorded on the lateral surfaces ($S/S_{max} < 0.3$ or $S/S_{max} > 0.7$), which may also be due to the impingement jets being closer to the side walls thanks to their staggered arrangement. Since a small angle is present between the side walls and the jet axis, this may suggest that in this kind of geometry the direct interaction between the jet shear layer and the solid surface play an important role in the heat transfer phenomenon (Figure 5.19).
In this case, the high heat transfer regions have strongly different shapes for the different jets: the pattern is segmented in multiple secondary peaks, most of which surround the extraction holes, and is clearly distorted towards the extraction holes themselves. This suggests a strong influence of extraction layout on the heat transfer phenomenon, even stronger than the one recorded for the inline geometry (GTE-A): the flow field determined by such orifices seems to be able to interact with the jets before the actual impingement, thus driving the flow along different paths with respect to the expected ones.

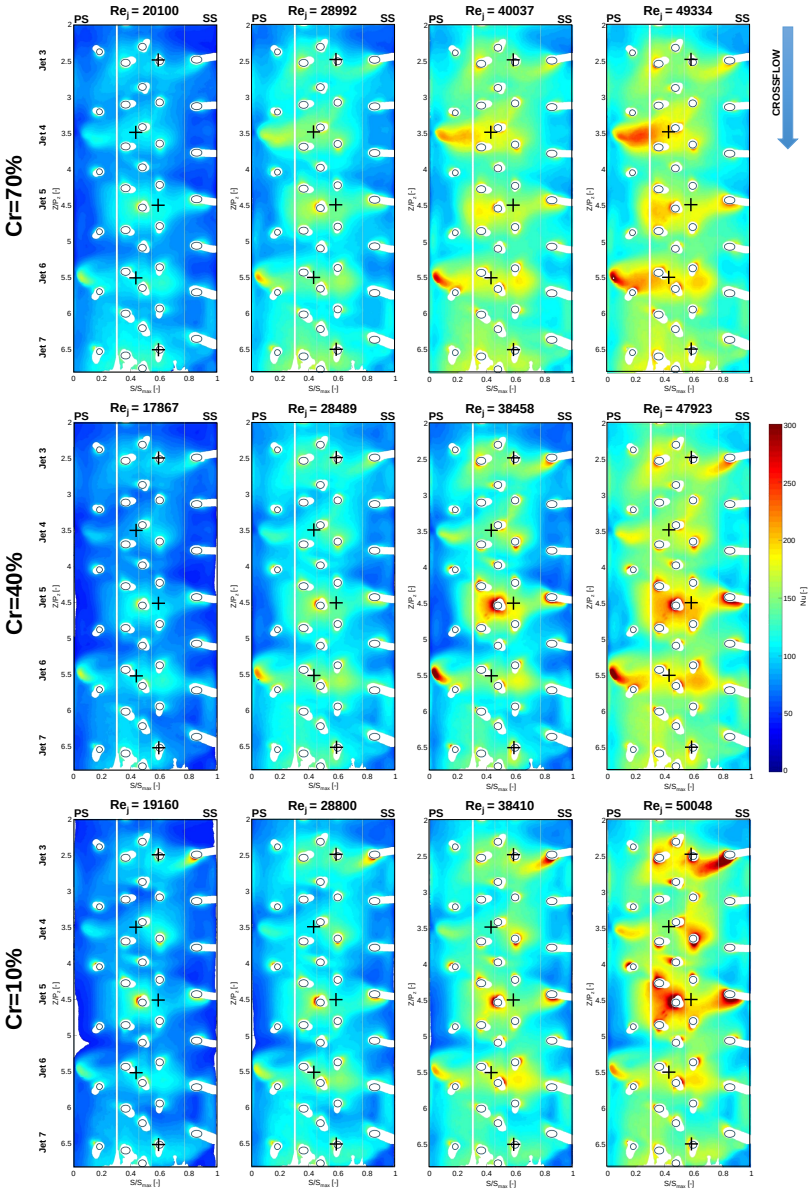


*Figure 5.17: Nu distributions for GTE-B geometry in static conditions ($Ro_j = 0$).*

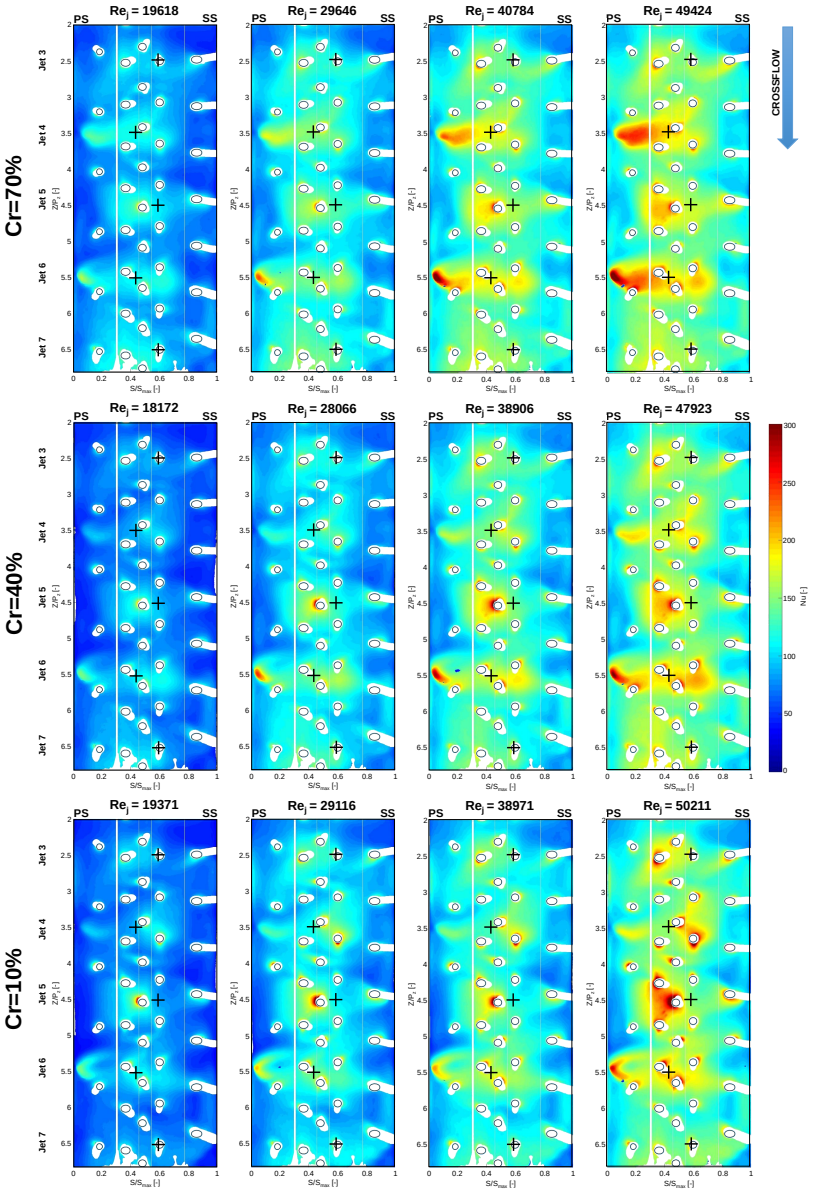


*Figure 5.18: Nu distributions for GTE-B geometry in rotating conditions ($Ro_j = 0.008$).*

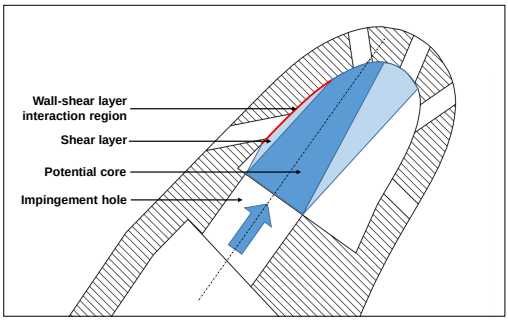


*Figure 5.19: Scheme of the wall-shear layer interaction for GTE-B geometry.*

### 5.2.1 Effect of Reynolds number

The $Nu$ distributions of Figures 5.17 and 5.18 also allow to appreciate that an increase in jet Reynolds number leads to an increase in heat transfer magnitude in every location, while the heat transfer pattern shape seems almost insensitive to such parameter.
A quantitative representation of the Reynolds effect on heat transfer

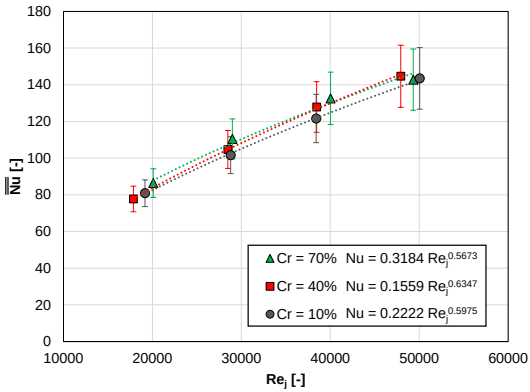


*Figure 5.20: Area averaged $Nu$ values for GTE-B geometry in static conditions ($Ro_j = 0$).*

magnitude is reported in Figure 5.20, which presents area averaged Nusselt values as a function of Reynolds for static tests. Like in the GTE-A case, average $Nu$ appear to be closely proportional to $Re_j^{0.6}$ in every investigated condition. Rotating results, which are not reported for the sake of brevity, also present similar trends.

### 5.2.2 Effect of crossflow condition

Figure 5.21 presents heat transfer distributions for tests performed in similar conditions (static with $Re_j$ around 40000) but with different values of crossflow ratio. Following the considerations of Section 5.2.1, $Nu$ values are scaled with respect to $Re_j^{0.6}$ in order to remove the possible effects of this parameter. In this case, a significant effect of the crossflow

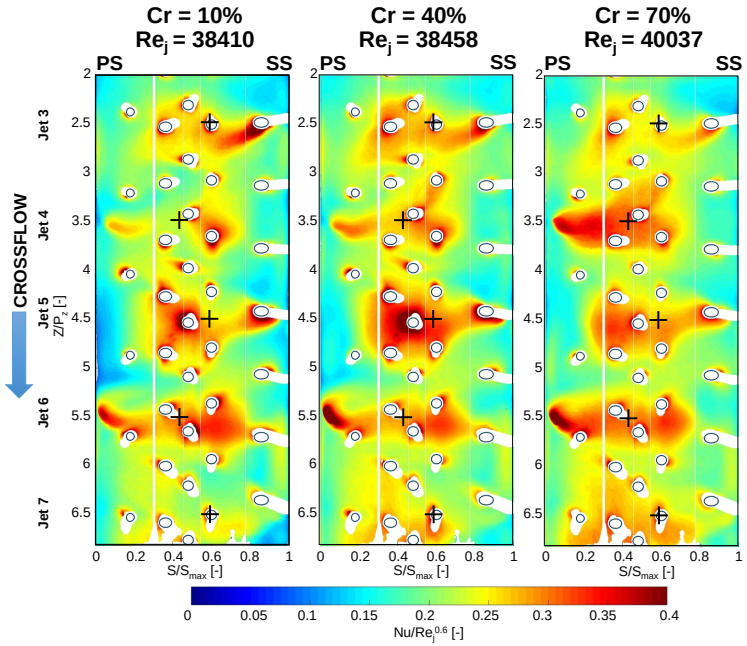


*Figure 5.21: $Nu/Re_j^{0.6}$ distributions for GTE-B geometry in static conditions ($Ro_j = 0$) for different crossflow values.*

is present. As crossflow increases (i.e. moving from the tip to the hub of the blade) a relevant increase in heat transfer is recorded: in particular, the peak extension strongly increases with the crossflow, leading to an overall positive effect. The observed phenomena are coherent with the supposition presented in Section 5.1.2, which is that a higher crossflow enhances the jet lateral spreading. Since in this case the interaction between the jets and the side walls seems to be a significant driving mechanism for heat transfer, it is likely that a higher jet lateral spreading significantly promotes the system performance.

On the other hand, no significant shift of the peak locations in the crossflow direction can be noticed, which leads to the supposition that the impingement holes are able to drive the flow normal to the target surface despite the upstream condition.

An additional insight on the crossflow effect can be provided by analysing the line averaged $Nu/Re_j^{0.6}$ distributions corresponding to the maps of Figure 5.21, which are reported in Figure 5.22. A higher crossflow is generally positive for heat transfer, but in a non uniform way: on the pressure side ($S/S_{max} < 0.3$) heat transfer increases of around 10% passing from $Cr = 10\%$ to $Cr = 70\%$, while on the central region

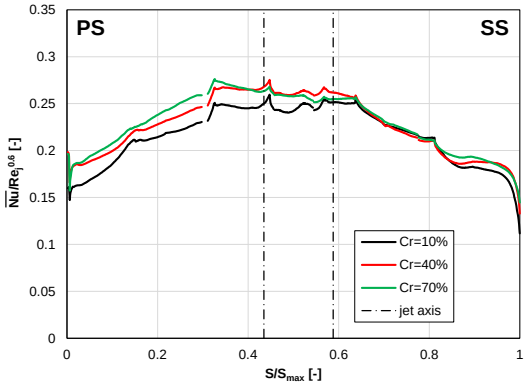


*Figure 5.22: Line averaged $Nu/Re_j^{0.6}$ distributions for GTE-B geometry in static conditions ($Ro_j = 0$) for different crossflow values.*

($0.3 < S/S_{max} < 0.7$) the increase is around 5%; on the other hand, a non significant increase (lower than 2%) is present on the suction side ($S/S_{max} > 0.7$). The overall combined effect is positive and can be quantified with an increase in heat transfer of around 5% in static conditions (which can also be noticed from values reported in Figure 5.20), while in rotating conditions an increase of around 10% is recorded.

### 5.2.3 Effect of rotation

In order to give an insight on the rotational effects for GTE-B geometry, heat transfer distributions obtained in static and rotating conditions are compared in Figure 5.23.
For the present case, passing from static to rotating conditions seems to

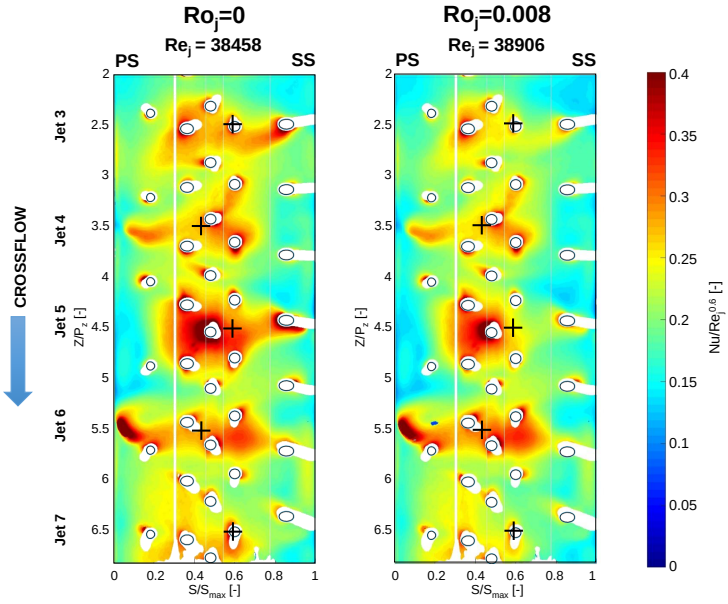


*Figure 5.23: $Nu/Re_j^{0.6}$ distributions for GTE-B geometry at $Re_j \simeq 40000$, $Cr = 40\%$ in static ($Ro_j = 0$) and rotating ($Ro_j = 0.008$) conditions .*

have little effect on the maximum values of heat transfer (see the peaks in the central regions located at around $Z/P_z = 3.5$, 4.5 and 5.5) but causes a significant decrease in every other location. As observed for GTE-A geometry, in rotating conditions the jets are expected to get concentrated towards the central part of the leading edge: in this case, the resulting lower lateral expansion would reduce the interaction between the jets and the side walls, thus decreasing heat transfer.

The two distributions also reveal that the heat transfer reduction seems stronger for the jets located closer to the suction side with respect to the ones located closer to the pressure side: if the area corresponding to each jet is considered, jet 3, 5 and 7 (which are closer to the SS) experience a heat transfer decrease around 9%, while jets 4 and 6 (which are closer to the PS) undergo a decrease of around 5%. This fact can be justified by considering rotational effects in the supply channel. As illustrated in section 5.1.3, during rotation the flow inside the supply channel is driven along the pressure side by the resulting Coriolis forces, leading total pressure to increase in this region. This phenomenon may promote coolant supply for the jets located closer to the pressure side, thus weakening the negative rotational effects in this region.

For the present case, rotation seems to have a negative effect on cooling performance for every crossflow condition. Even so, the entity of the rotation related phenomena decreases as crossflow increases, which can be observed looking at the line averaged heat transfer distributions

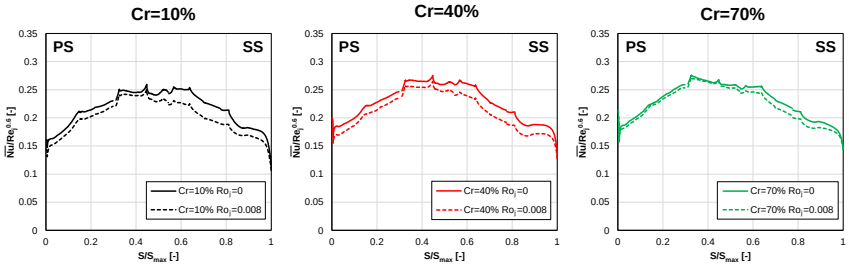


*Figure 5.24: Line averaged $Nu/Re_j^{0.6}$ distributions for GTE-B geometry at around $Re_j = 40000$.*

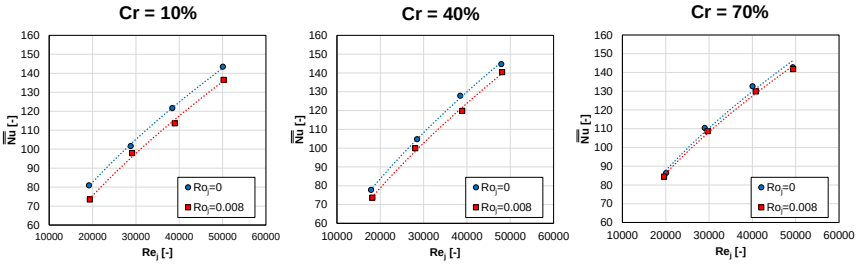


*Figure 5.25: Area averaged $Nu$ values for GTE-B geometry for different crossflow conditions.*

reported in Figure 5.24. In particular, in every investigated condition heat transfer decreases due to rotation, but the decrease appears stronger for the $Cr = 10\%$ case in every spanwise location. Moreover, $Cr = 10\%$ condition also presents the largest difference between pressure and suction side during rotation, which may be attributed to the stronger rotational effects occurring inside the supply channel in this case.
The overall effect of rotation on heat transfer can be quantified by considering area averaged $Nu$ values, which can be performed looking at the charts of Figure 5.25 for the three investigated crossflow conditions. These values confirm that the maximum heat transfer decrease is recorded for $Cr = 10\%$ condition, with a 7% reduction with respect to the static case. The entity of such difference then decreases as crossflow increases, passing to 5% at $Cr = 40\%$ and finally to 2% at $Cr = 70\%$.

### 5.2.4 Effect of extraction condition

For GTE-B geometry the influence of extraction condition was determined by evaluating the two extreme split cases (All FC and All SH) for a single test point corresponding to static conditions, $Re_j \simeq 30000$ and $Cr = 40\%$ (i.e. in the same conditions also considered for GTE-A geometry). Figure 5.26 presents the obtained heat transfer distributions, together with the reference standard extraction case.
The data reveal the influence of extraction layout for this geometry: for

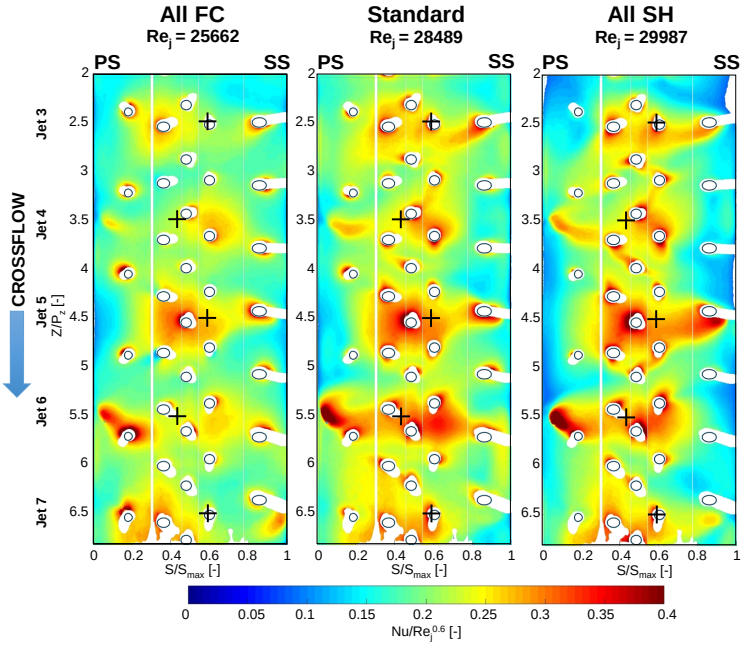


*Figure 5.26: $Nu/Re_j^{0.6}$ distributions for GTE-B geometry for different extraction conditions ($Cr = 40\%$, $Ro_j = 0$, $Re_j \simeq 30000$).*

the three investigated conditions, the general shape of the heat transfer pattern is similar, but the gradients become much more intense passing from the All FC to the All SH conditions. In All FC condition, in particular, a unique pattern is generated for each impingement jet, since heat transfer seems to concentrate into two distinct regions at opposite sides of the stagnation point, highlighted in Figure 5.27. The most uniform distribution is also obtained in this case. On the other hand, for the All SH condition a strong non-uniformity is present: the extraction only through the SH rows seems to be able to concentrate the impingement flow only in the LE central region, where a complex heat transfer pattern is generated by the mutual interaction of the close extraction holes. It is also worth noticing that the heat transfer peaks on the side walls are

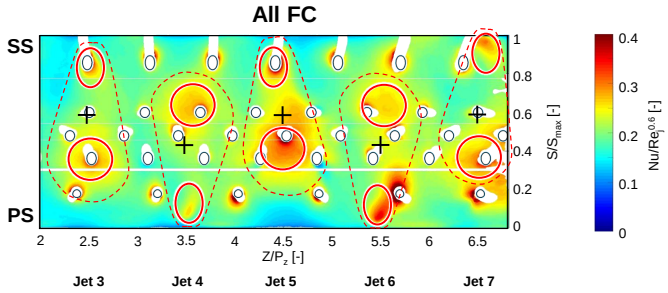


*Figure 5.27: Detail of the double peak structure for the All FC case.*

stronger in this extraction condition, but at the same time such peaks are surrounded by wide regions of low heat transfer. The comparison with the All FC condition suggests that flow extraction from FC holes was actually disturbing jet impingement on the side walls, but at the same time was able to recall a part of the spent coolant flow towards these regions, globally enhancing heat transfer.

The phenomena highlighted by the heat transfer maps are reflected by the

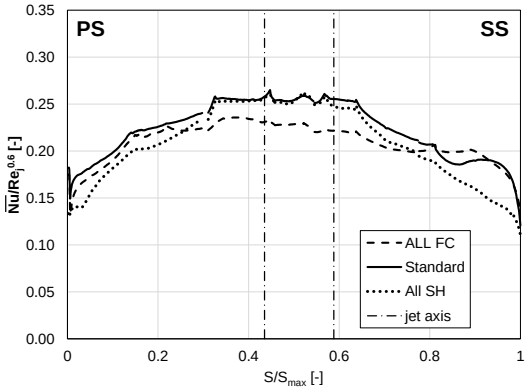


*Figure 5.28: Line averaged $Nu/Re_j^{0.6}$ distributions for GTE-B geometry for different extraction conditions ($Cr = 40\%$, $Ro_j = 0$, $Re_j \simeq 30000$).*

corresponding line averaged distributions, reported in Figure 5.28. The direct comparison between the two extreme cases reveals that passing from the All FC to the All SH condition line averaged heat transfer can decrease up to 28% on the side walls and increase up to 12% in the central region. Even so, the combination of these differences has a negligible effect on overall heat transfer, since for the two extreme cases the area averaged value of $Nu/Re_j^{0.6}$ is 0.209 and 0.208 respectively. On the other hand, Figure 5.28 shows that the best cooling performance is obtained by the standard extraction case almost in every location, which in fact provides an area averaged value of $Nu/Re_j^{0.6}$ equal to 0.222, i.e. 7% higher than the two extreme cases. This last evidence suggests that GTE-B flow field, and thus heat transfer, is more influenced by the extraction holes than by the impingement jets, given the ability of the former to drive the coolant flow towards their locations.

### 5.2.5 Flow check results

The discharge coefficient values corresponding to the tests of Figures 5.17 and 5.18 are plotted as a function of jet Reynolds number in Figure 5.29. In this case similar results are obtained with respect to the GTE-A

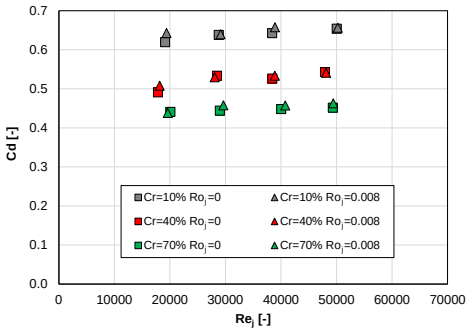


*Figure 5.29: Impingement holes discharge coefficient for GTE-B geometry.*

geometry: the highest $Cd$ values are obtained in $Cr = 10\%$ conditions, when the impingement holes supply is more similar to a plenum. Increasing the $Cr$ value significantly degrades $Cd$: reductions of around 18% are recorded passing to $Cr = 40\%$ and of 30% passing to $Cr = 70\%$. Such degradations can be attributed to the size of flow separation occurring on the impingement holes upstream side, which can be expected to increase with the crossflow [120]. Like for GTE-A geometry, no significant effects of Reynolds number or rotation on the $Cd$ values are recorded in this case.

## 5.3 GTE-C results

This section illustrates the results obtained with GTE-C geometry, an overview of which is provided by the $Nu$ maps presented in Figures 5.30 and 5.31 for static and rotating tests respectively.
The notation is identical to the one employed for GTE-A and GTE-B maps. Like in the previous cases, only the region which is not affected by thermal boundary effects is presented, which in this case lead to the exclusion of the region corresponding to the jets 1-4 ($Z/P_z < 4$). Given the different holes number and diameter with respect to GTE-A and GTE-B, the use of similar mass flow rate and rotational speed values for all the geometries resulted for the GTE-C in different nominal $Re_j$ and $Ro_j$ values (see section 3.1): in particular, $Re_j$ values ranging from 12500 to 35000 were tested in this case, as well as a $Ro_j$ value of 0.006 in rotating conditions.
Similarly to the other investigated geometries, a high heat transfer region is present for each impingement jet, located on the pressure or on the suction side according to the location of the corresponding impingement hole. These regions have a strongly elongated shape in the horizontal direction, and the largest part of them is located on the side walls ($S/S_{max} < 0.3$ and $S/S_{max} > 0.7$). These features allow to suppose that these peaks are mainly due to the interaction between the impingement jets and the side walls. This hypothesis is also confirmed by the fact that the highest $Nu$ values are usually located closer to the outer extremities of the surface.
It can also be noticed that the magnitude of $Nu$ peaks is stronger on the PS than on the SS. Since impingement holes and target surface features are similar for both PS and SS impingement rows, the reasons of such difference may be attributed to the hole supply condition. In particular, heat transfer peaks on the suction side seems to be located at a higher distance from the target surface extremity with respect to the pressure side. Moreover, while PS peaks appear to be aligned with the corresponding impingement holes, SS peaks all seem to be shifted in the crossflow direction. An interpretation of this phenomenon, which is

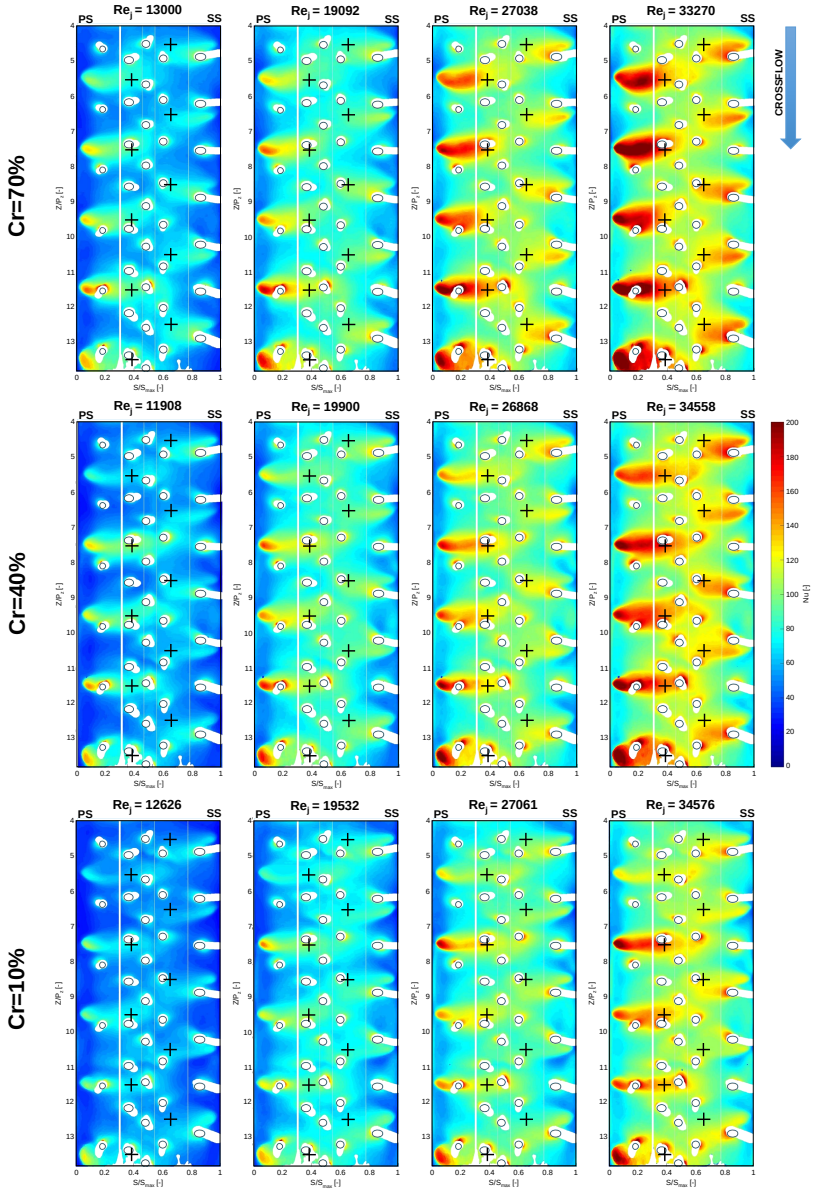


*Figure 5.30: Nu distributions for GTE-C geometry in static conditions ($Ro_j = 0$).*

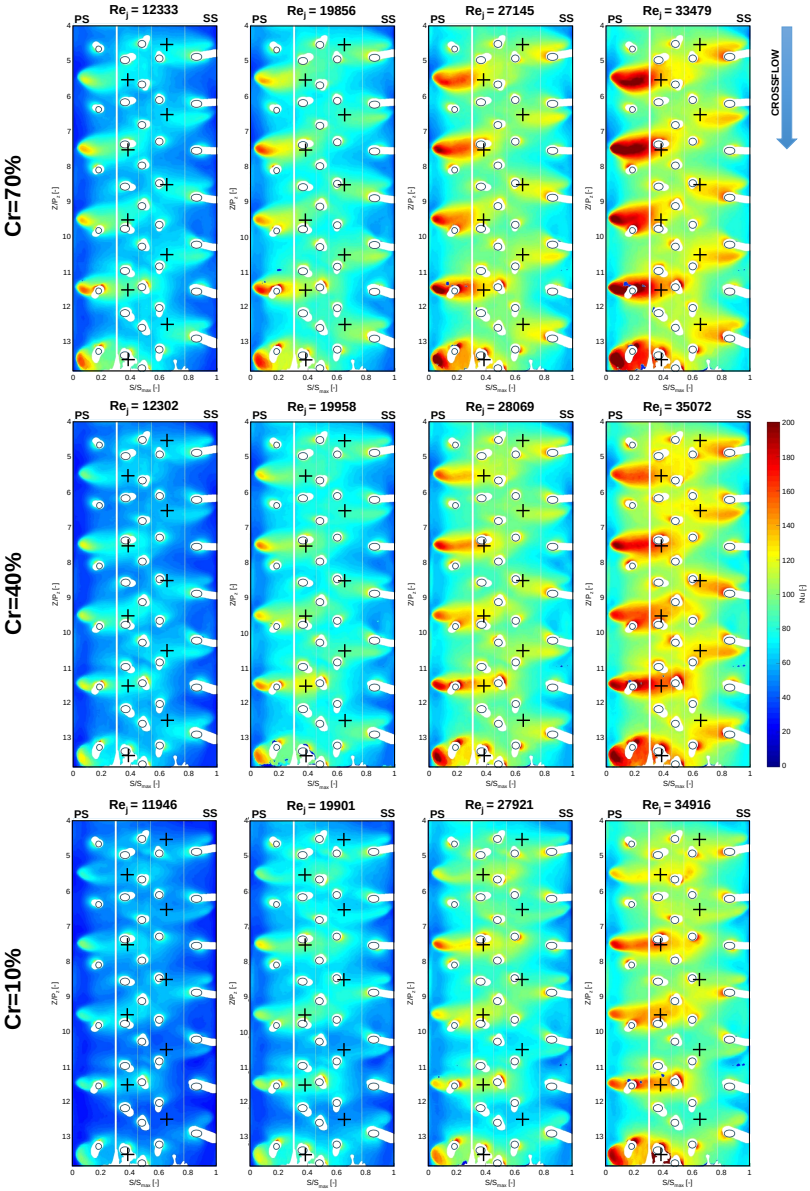


*Figure 5.31: Nu distributions for GTE-C geometry in rotating conditions ($Ro_j = 0.008$).*

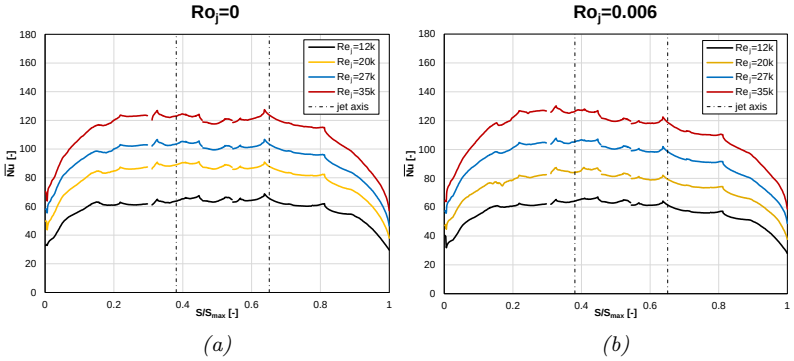


*Figure 5.32: Line averaged $Nu$ spanwise distributions for GTE-C geometry with $Cr = 40\%$ in static (a) and rotating (b) conditions.*

challenging to retrieve from the sole heat transfer experimental results, will be provided in Chapter 6 exploiting the outcomes of the numerical analysis. The heat transfer distributions of Figures 5.30 and 5.31 also allow to notice that a reasonably repeatable heat transfer pattern is present for both PS and SS impingement jets: the peak shape is similar for each hole, and appears to be only slightly distorted by the closer extraction holes. This phenomenon suggests that in this case heat transfer is dominated by the jet flow field, at least on the side walls. In the central region, the influence of extraction holes on $Nu$ pattern seems stronger, with clear peaks surrounding each hole: since the jet-wall interaction seems to occur mainly on the side walls, it is reasonable to suppose that the momentum of jet flow is significantly reduced when it reaches such region, thus leading to a stronger effect of the extraction flow field.

The combined effect of all the aforementioned phenomena can be quantified by considering the line averaged $Nu$ distributions reported in Figure 5.32 for the $Cr = 40\%$ case. The low heat transfer regions on the side walls compensate the intense heat transfer peaks in these zones, providing an average heat transfer which is almost equal to the one in the central region. This results in an evident uniformity of the streamwise pattern, with almost constant $Nu$ values for $S/S_{max}$ between 0.2 and 0.8.

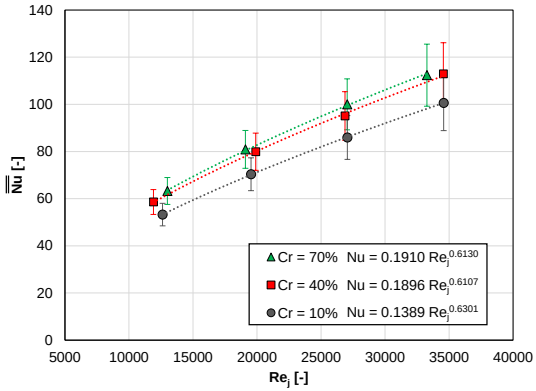


*Figure 5.33: Area averaged $Nu$ values for GTE-C geometry in static conditions ($Ro_j = 0$).*

### 5.3.1 Effect of Reynolds number

The effect of jet Reynolds number on heat transfer can be determined by the analysis of Figures 5.30, 5.31 and 5.32. As already observed for the previous geometries, an increase in $Re_j$ value uniformly improves heat transfer in every location, and thus has negligible effects on the shape of the heat transfer pattern.
An insight on the overall dependency of heat transfer from the jet Reynolds number can be provided by the area averaged $Nu$ values, which are reported in Figure 5.33 for the tests performed in static conditions. A similar dependency can be observed for every investigated crossflow condition, with average $Nu$ values being almost proportional to $Re_j^{0.6}$. Similar trends are also recorded for the outcomes of rotating tests.

### 5.3.2 Effect of crossflow condition

The effect of different jet supply conditions, i.e. of different blade radial sections, can be determined if the heat transfer distributions obtained for different crossflow values are compared, which is performed in Figure

5.34 for test performed at a nominal $Re_j$ value of 20000. Like for the previous geometries, $Nu$ values are scaled with respect to $Re_j^{0.6}$ to remove the effect of such parameter from the results. The most evident effect of a higher crossflow ratio is the intensification of the heat transfer peaks: passing from $Cr = 10\%$ to $Cr = 70\%$ both the PS and the SS peaks grow in size and magnitude, with an overall positive effect on heat transfer. Outside of the peaks the crossflow effect is weaker, but a slight heat transfer enhancement is still present. Apart for that, no significant change in the heat transfer pattern shape can be identified. This phenomenon is somewhat similar to the one already observed for GTE-B geometry, and can be ascribed to the same cause: increasing the crossflow leads to an enhancement of the lateral expansion of the jets, thus increasing the interaction between the side walls and the jet themselves. In this case,

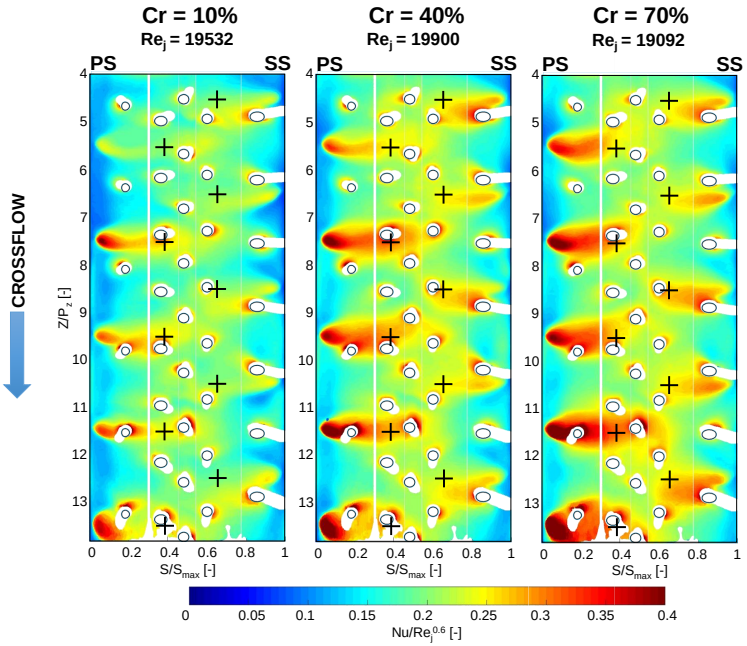


*Figure 5.34: $Nu/Re_j^{0.6}$ distributions for GTE-C geometry in static conditions ($Ro_j = 0$) for different crossflow values.*

however, the phenomenon is particularly intense, since in this geometry heat transfer seems to be mainly driven by the aforementioned interaction. A quantification of the crossflow effects can be obtained by considering the line averaged spanwise heat transfer distributions, which are reported in Figure 5.35 for the maps of Figure 5.34. Passing from $Cr = 10\%$ to $Cr = 40\%$ an almost uniform heat transfer increase is recorded: in average terms, heat transfer increase is around 14% on the pressure side and around 11% both in the central region and on the suction side. On the other hand, passing from $Cr = 40\%$ to $Cr = 70\%$ still causes heat transfer to increase on pressure and suction side (of 7% and 4% respectively) but no significant variation is recorded in the central region.
The aforementioned variations lead overall heat transfer to increase with crossflow ratio: passing from the minimum to the maximum crossflow condition, area average $Nu$ increases of around 14% in static conditions (which can be noticed from Figure 5.33) and of around 18% in rotating conditions. These effects are coherent with the ones recorded for the other geometry housing staggered holes, but are significantly more intense in this case.

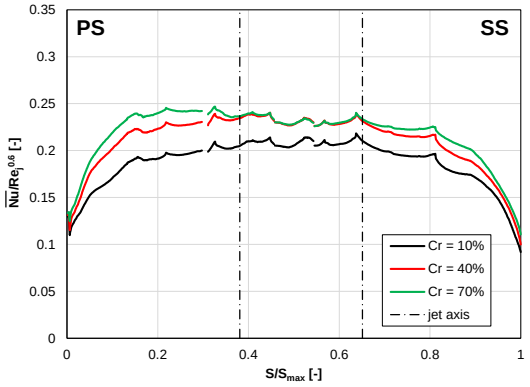


*Figure 5.35: Line averaged $Nu/Re_j^{0.6}$ distributions for GTE-C geometry in static conditions ($Ro_j = 0$) for different crossflow values.*

### 5.3.3 Effect of rotation

In Figure 5.36 two sample heat transfer distributions obtained for corresponding test conditions in static and rotating conditions are presented. The two distributions reveal a non uniform influence of rotation. On the pressure side the rotational effects are weak, with a widespread slight decrease in heat transfer. On the other hand, on the suction side a significant heat transfer reduction is present, with local values decreasing in every location. If the different regions are considered separately, rotation seems not to have a significant effect on heat transfer pattern shape. Even if this effect is slightly different from the one recorded for GTE-B, they both can be justified considering the same combination of phenomena. In fact, as presented in Section 5.1.3 rotation is expected to decrease jet lateral spreading, thus reducing the jet-wall interaction

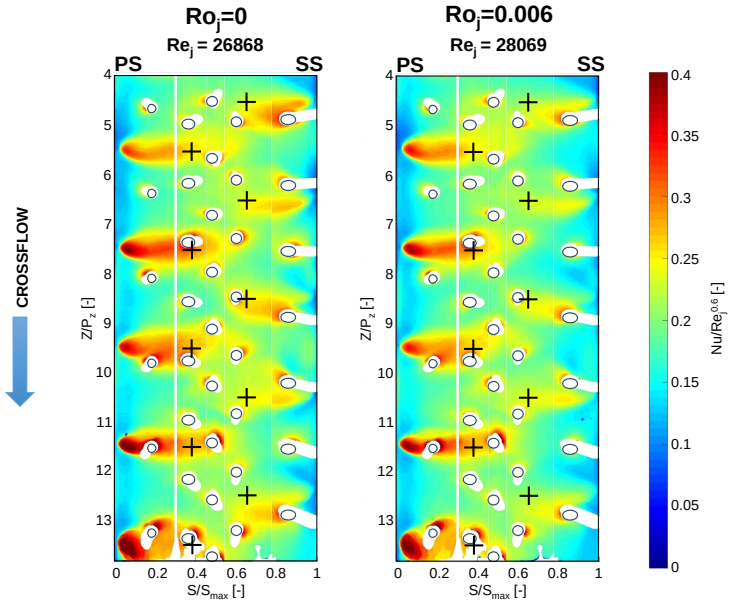


*Figure 5.36: $Nu/Re_j^{0.6}$ distributions for GTE-C geometry at $Re_j \simeq 27500$, $Cr = 40\%$ in static ($Ro_j = 0$) and rotating ($Ro_j = 0.006$) conditions .*

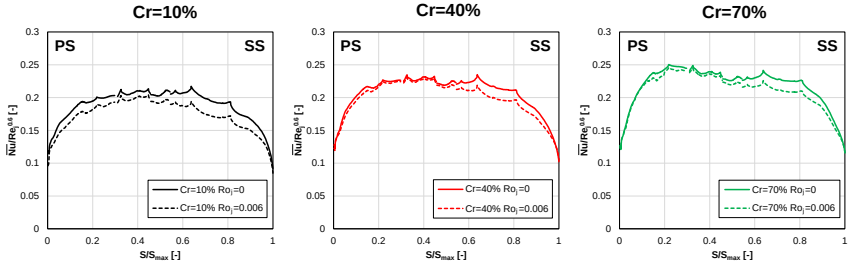


*Figure 5.37: Line averaged $Nu/Re_j^{0.6}$ distributions for GTE-C geometry at around $Re_j = 27500$.*

and decreasing heat transfer. However, at the same time Coriolis forces inside the feeding channel drive the flow along the pressure side, which is expected to promote the coolant supply for the jets located in this region. As a result, on the pressure side the two effects are counterbalanced, while on the suction side their negative effects on heat transfer are combined, resulting in a significant reduction.

As recorded for the other geometries, also for GTE-C rotational effects are sensible to crossflow. This can be appreciated by observing the line averaged heat transfer distributions of Figure 5.37. In $Cr = 10\%$ conditions, rotation leads heat transfer to decrease in every location, but such reduction is weaker for the pressure side with respect to the suction side (approximately 7% and 11% respectively). On the other hand, for both

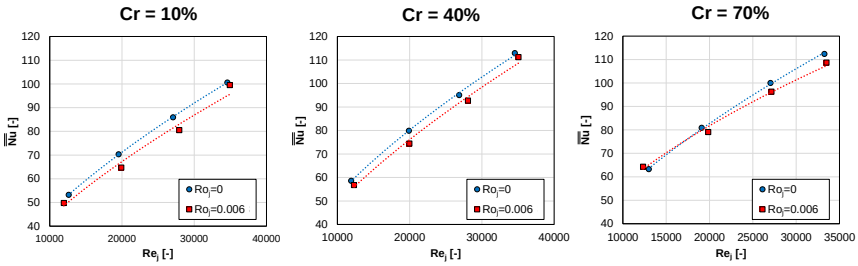


*Figure 5.38: Area averaged $Nu$ values for GTE-C geometry for different crossflow conditions.*

$Cr = 40\%$ and $Cr = 70\%$ a negligible difference is present on the pressure side, while a small reduction is recorded on the suction side (around 8% and 6% respectively).
The overall effects of crossflow can be determined considering area averaged $Nu$ values, which are reported in the charts of Figure 5.38 for different crossflow conditions. Such values reveal that the strongest decrease occurs in $Cr = 10\%$ conditions, with a 6% heat transfer reduction with respect to the static case. Differences decrease to 5% in $Cr = 40\%$ condition and finally to a negligible 2% in $Cr = 70\%$ condition.

### 5.3.4 Effect of extraction condition

For the present case, the two additional extraction conditions were investigated for the test with a nominal $Re_j$ of 20000, in static conditions and at the intermediate crossflow ratio. The corresponding heat transfer

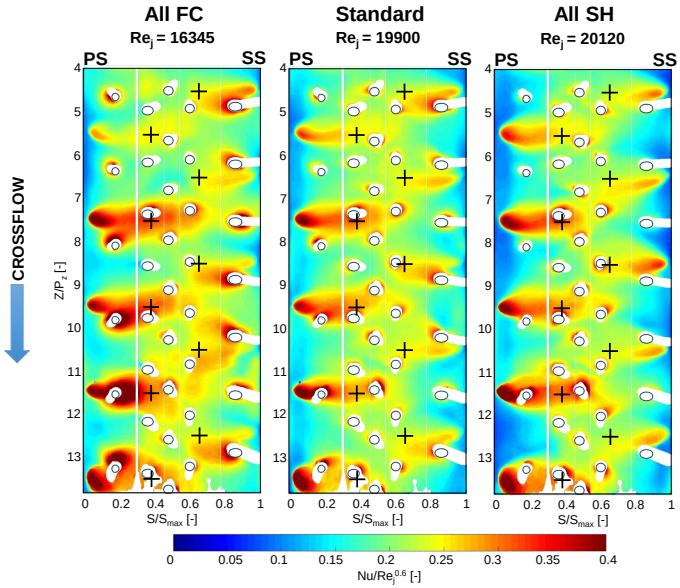


*Figure 5.39: $Nu/Re_j^{0.6}$ distributions for GTE-C geometry for different extraction conditions ($Cr = 40\%$, $Ro_j = 0$, $Re_j \simeq 20000$).*

distributions, together with the outcome of the standard extraction test, are presented in Figure 5.39. These results reveal that, passing from All FC to All SH, the maximum heat transfer values are very similar in the peak locations, but a strong heat transfer reduction is recorded in all of the remaining locations. Despite this, heat transfer pattern shape seems similar in all the investigated conditions. This phenomenon seems to confirm that heat transfer in the peak locations is dominated by jet impingement, but also suggests that the extraction holes are mostly able to affect the low momentum flow (e.g. the wall jet flow): in fact, outside of the peaks heat transfer seems to increase where mass flow extraction is present.

The heat transfer distributions already suggest that, in this case, the best cooling performance is obtained for the All FC case. This evidenced is confirmed by the line averaged heat transfer distributions for the three tests, reported in Figure 5.40. While in the central region ($0.3 < S/S_{max} < 0.7$) the cooling performance seems unaffected by the extraction condition,

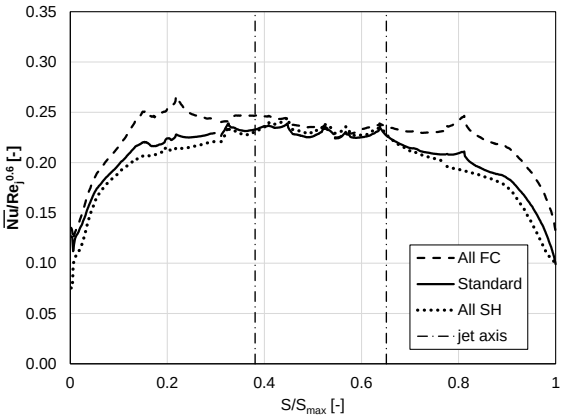


*Figure 5.40: Line averaged $Nu/Re_j^{0.6}$ distributions for GTE-C geometry for different extraction conditions ($Cr = 40\%$, $Ro_j = 0$, $Re_j \simeq 20000$).*

on the side walls a clear trend is present, with heat transfer increasing as the amount of mass flow rate extracted by the FC holes increases. Such trend is clearly different from the results obtained with both GTE-A and GTE-B, and provides a 10% increase in area average heat transfer passing from All SH to All FC condition.

### 5.3.5 Flow check results

The discharge coefficient values obtained for the tests of Figures 5.30 and 5.31 are reported in Figure 5.41. Also in this case similar dependencies with respect to GTE-A and GTE-B geometries are recorded: $Cd$ values decrease as crossflow ratio increases, with a 30% difference between $Cr = 10\%$ and $Cr = 70\%$ conditions. In this case, however, slightly higher $Cd$ values are recorded in every condition with respect to the geometries with larger holes diameters: as a consequence, lower pressure drops can be expected for this kind of geometry with respect to the previous ones. Once again, neither jet Reynolds number nor rotation seem to be able to influence the discharge coefficient values in a significant way.

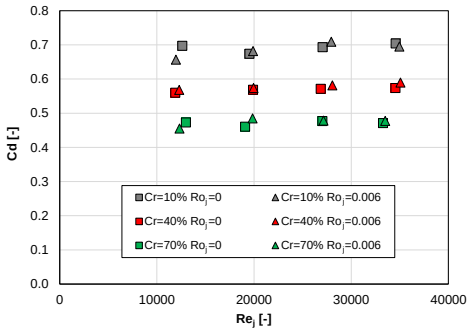


*Figure 5.41: Impingement holes discharge coefficient for GTE-C geometry.*

## 5.4 Comparison between impingement geometries

The three investigated impingement geometries present different features in terms of holes number, diameter and arrangement. Even so, as already reported in Section 3.1 they were designed in order to provide the same overall passage area for the flow: as a consequence, for a given coolant mass flow rate the same average jet velocities are obtained. The three geometries can thus be interpreted as different ways of distributing the coolant inside the leading edge cavity, and a direct comparison of their performance allows to highlight the effect of the different arrangements. To provide a significant comparison, in this section test conditions are reformulated using the width of an equivalent two-dimensional slot $b$ (defined in Equation 3.2) as characteristic length, obtaining parameters which are representative of the actual coolant consumption: the presented values of Reynolds and Rotation numbers are thus defined according to Equations 3.3 and 3.5. This provides $Re_b$ values ranging from 5400 to 13800 and a $Ro_b$ value of 0.002 for rotating tests. In order to be coherent with these definitions, Nusselt number is also recast with respect to $b$:

$$Nu_b = \frac{hb}{\lambda} \tag{5.3}$$

An example of heat transfer distributions obtained with the three geometries in similar conditions is reported in Figure 5.42, while the corresponding line averaged streamwise heat transfer distributions are presented in Figure 5.43. As already done in the previous sections, Nusselt number values are scaled with respect to the corresponding Reynolds value to the power of 0.6 to remove the effects of slight differences in this parameter. On the other hand, in Figure 5.44 area averaged $Nu_b$ values are presented as a function of $Re_b$ for each combination of crossflow ratio and rotation condition. Finally, Figure 5.45 presents area averaged $Nu_b/Re_b^{0.6}$ values as a function of the crossflow ratio for the three geometries. The data presented in the aforementioned figures allows to highlight the effects of the different features of the investigated geometries, which will be performed in the following sections.

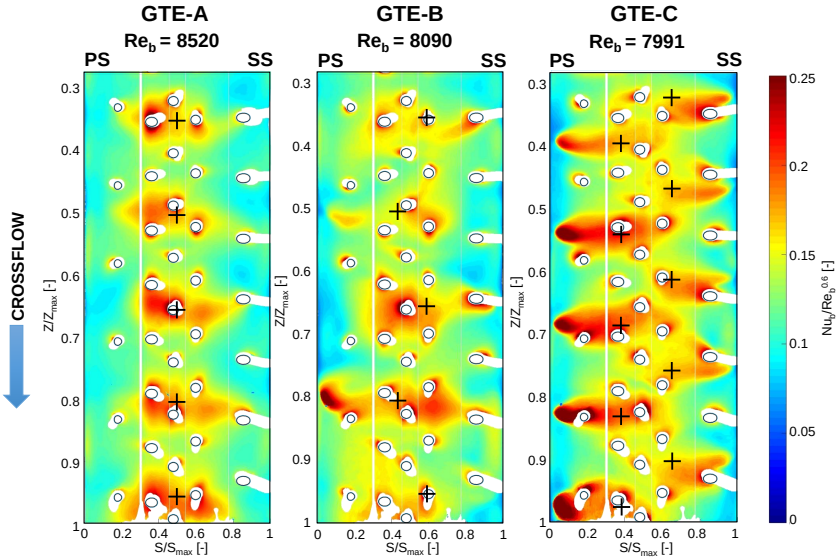


*Figure 5.42: $Nu_b/Re_b^{0.6}$ distributions for the three geometries in similar test conditions ($Cr = 40\%$, $Ro_b = 0$, $Re_b \simeq 8200$).*

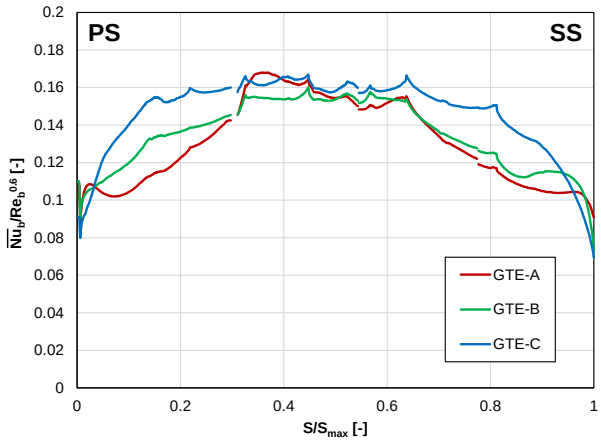


*Figure 5.43: Line averaged $Nu_b/Re_b^{0.6}$ distributions for the three geometries in similar test conditions ($Cr = 40\%$, $Ro_b = 0$, $Re_b \simeq 8200$).*

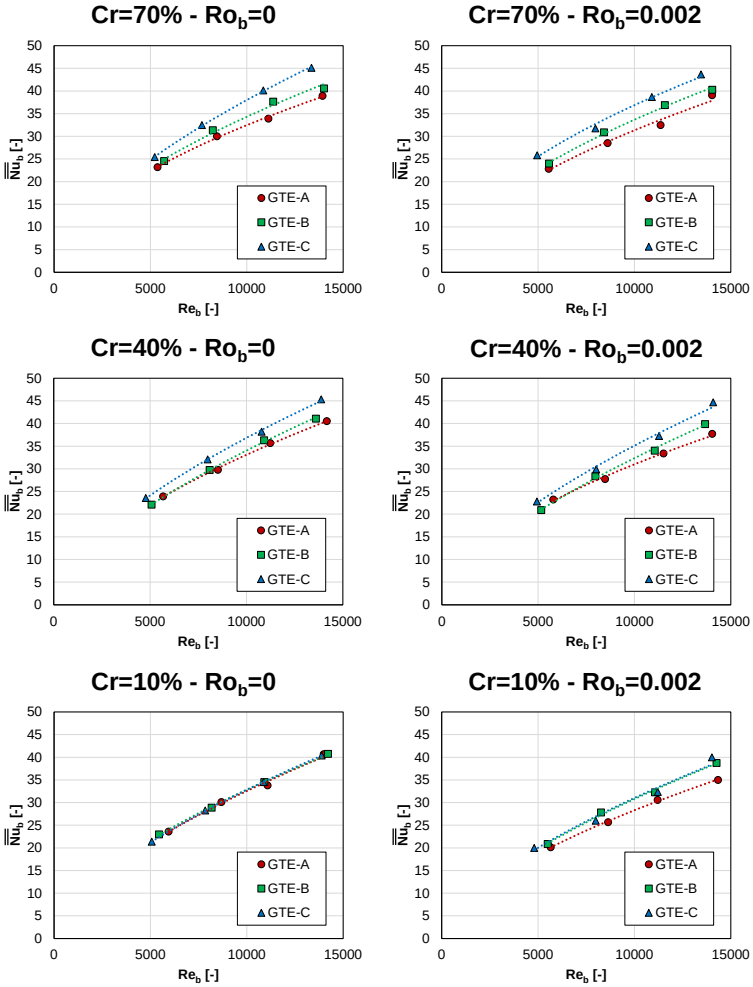


*Figure 5.44: Area averaged $Nu_b$ values as a function of $Re_b$ for the three geometries for different crossflow and rotation condition.*

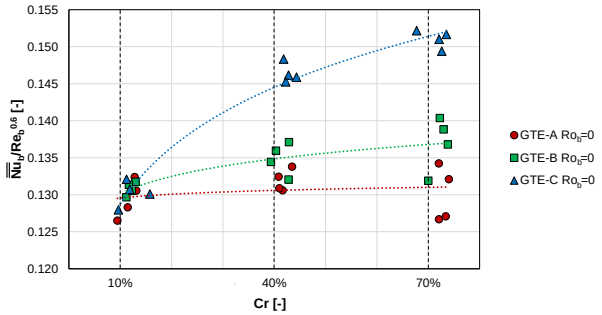


*Figure 5.45: Area averaged $Nu_b/Re_b^{0.6}$ values as a function of Cr for the three geometries in static conditions.*

### 5.4.1 Effect of holes arrangement

The effect of different holes locations can be determined by comparing GTE-A and GTE-B geometries, whose only difference is the arrangement of impingement jets (inline for GTE-A and staggered for GTE-B). If the heat transfer maps corresponding to the two geometries are considered in Figure 5.42, it can be noticed that strongly different patterns are generated in the two cases: GTE-B provides a much wider lateral expansion of the primary peaks towards the outer sides of the target surface, which is due to the impingement holes being closer to the side walls in this case. A much more irregular and uneven pattern is also present for GTE-B, since the primary peaks are often fragmented into a series of small high heat transfer regions close either to the sides of the surface or to the extraction holes. This last fact seems to indicate that stronger jet-walls and jet-extraction holes interactions occur with the staggered hole arrangement. This also leads to a less uniform heat transfer distribution for GTE-B, with higher maximum and lower minimum values with respect to GTE-A. The quantitative outcome of these effects can be appreciated considering the spanwise trends of Figure 5.43: according to the holes location, GTE-A is able to provide slightly higher heat transfer values in the LE central region, while on the side walls GTE-B geometry clearly prevails. In average terms, the combination of these differences usually provides a higher a heat transfer performance for GTE-B geometry.

This can be appreciated considering the area averaged $Nu_b$ values presented in Figure 5.44, which also reveal the different sensitivities of two geometries to supply conditions and rotation. In particular, no influence of holes arrangement seems to occur for $Cr = 10\%$ and $Ro_b = 0$, i.e. when the supply condition is similar to a plenum and no rotation is present. On the other hand, when the mass flow rate inside the supply channel is increased (i.e. passing to $Cr = 40\%$ and $Cr = 70\%$) GTE-B starts to provide better cooling performances with respect to GTE-A (with up to 5% higher heat transfer at maximum crossflow), namely due to the increased jet-wall interaction. This fact is also highlighted by Figure 5.45: while GTE-A performance appears almost insensitive to crossflow condition, for GTE-B a clear increasing trend can be identified. GTE-B also seems less sensitive to negative rotational effects than GTE-A: in fact, while for the latter heat transfer decreases from 13% to 4% for different $Cr$ values, for the former the maximum decrease at $Cr = 10\%$ is around 7%. As a general consideration, it can be stated that GTE-B provides better overall cooling performance than GTE-A, since it appears more sensitive to the positive effects of crossflow and less sensitive to the negative effects of rotation.

### 5.4.2 Effect of holes diameter

In order to define the effect of holes diameter on heat transfer, GTE-B and GTE-C geometries can be compared, which both have staggered holes arrangements but the second has twice the number of holes with a smaller diameter (14.14 $mm$ instead of 20 $mm$). Referring to the distributions of Figure 5.42, it can be noticed that GTE-C provides a much more regular heat transfer pattern than GTE-B, with an almost oval and non segmented peak for each impingement jet. This fact may be attributed to a lower interaction between the impingement jets and the extraction holes pattern: in fact, using smaller diameter holes allows to set the jet axis, and thus the peak velocity, closer to the side walls, where a lower number of extraction holes are present with respect to the central region. As a consequence, extraction holes are likely to have a smaller influence on jet

flow field and heat transfer pattern. The more coherent flow structure also seems to provide advantages in the central part of the profile, where the denser hole array seems to be able to perform a more uniform coverage of such region.
The two-dimensional distributions already suggest that higher cooling performance are obtained by GTE-C geometry, which is also confirmed by the line averaged values of Figure 5.43: GTE-C prevails over GTE-B in every location, and particularly on the side walls ($S/S_{max} < 0.3$ and $S/S_{max} > 0.7$). This improvement is verified in almost every condition, as shown by the charts of Figure 5.44. In particular, the two staggered geometries seem to provide very similar average $Nu_b$ values in the lowest crossflow condition ($Cr = 10\%$), both in static and rotating cases. Even so, when the crossflow grows GTE-C starts to overperform GTE-B: 8% higher heat transfer is recorded for $Cr = 40\%$ and 10% for $Cr = 70\%$, independently of the rotation condition. This is also demonstrated by the values of Figure 5.45: even if both GTE-B and GTE-C behave similarly at the lowest crossflow value and their performance increases with $Cr$, a much stronger sensitivity to the latter parameter is obtained with GTE-C.

### 5.4.3 Analysis of overall cooling performance

The analysis performed in Sections 5.4.1 and 5.4.2 reveals that, as regards the overall heat transfer performance, GTE-C prevails over both GTE-A and GTE-B, in particular when a strong crossflow is present upstream the holes and rotational effects are considered. However, in order to determine if GTE-C actually overperforms the other geometries a complete analysis of both heat transfer and flow performance of the system needs to be carried out. In particular, a complete and reliable comparison needs to take into account the amount of energy which is necessary to provide the fluid to obtain the measured heat transfer values. For internal flows, this parameter is directly related to the pressure losses across the investigated feature: in fact, it is possible to define the *pumping power* $W$ required to overcome a given pressure loss $\Delta p$ with a mass flow

rate $\dot{m}$ as:

$$W = \dot{m}\frac{\Delta p}{\rho} \tag{5.4}$$

Since in the present case pressure measurements are available both upstream and downstream the impingement holes, it is possible to evaluate the pumping power required in every condition for the different geometries, as well as to relate it to the heat transfer performance. This operation

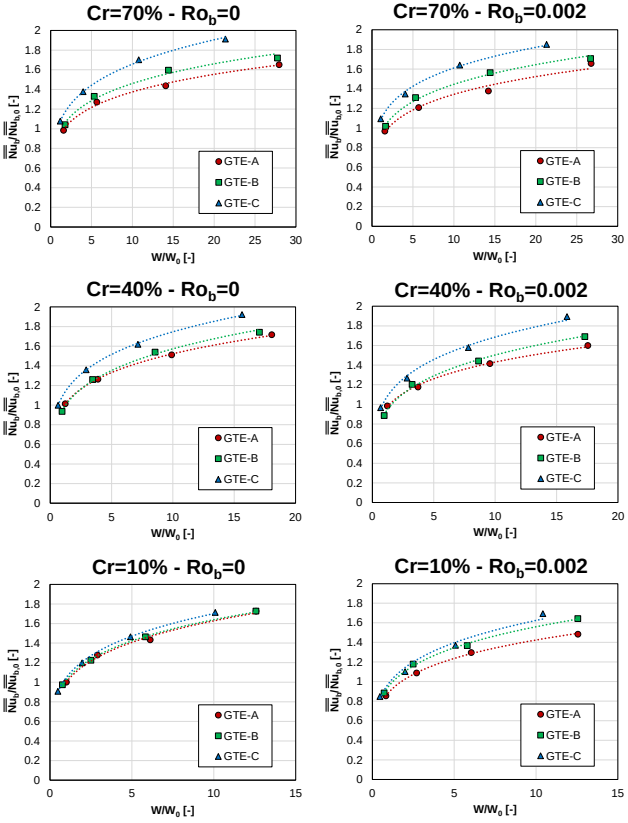


*Figure 5.46: Relative $Nu_b$ values as a function of relative pumping power for the three geometries for different crossflow and rotation conditions.*

is carried out in the charts of Figure 5.46. In order to provide a more significant comparison, the GTE-A test performed in static conditions with minimum $Cr$ and $Re_b$ values is chosen as a reference case, and the corresponding area averaged heat transfer $\overline{\overline{Nu}}_{b,0}$ and pumping power $W_0$ are employed to scale the values obtained for all the other tests.
The charts reveal that, for every geometry and in every condition, heat transfer increases with the employed pumping power with a trend very close to a power law, which is thus employed to fit the data. It can be noticed that for all the investigated conditions GTE-C geometry provides the highest heat transfer at a given value of pumping power, while GTE-A provides the lowest performance. Following the trends of area averaged heat transfer presented in Figure 5.44, the difference between the three geometries is minimum for $Cr = 10\%$ static tests and maximum for $Cr = 70\%$ tests. The advantage of GTE-C with respect to GTE-A and GTE-B is due both to the higher heat transfer values obtained for a given coolant consumption (i.e. at a given $Re_b$ value, as shown by Figure 5.44) and to the lower pressure losses, as indicated by the larger discharge coefficient values recorded for this geometry. As a consequence, it can be stated that the best overall cooling performance in the investigated range of parameters is provided by GTE-C geometry.

## 5.5 Concluding remarks

The results presented in this chapter allowed to perform a detailed study of each of the three geometries, observing the corresponding thermal phenomena and discussing the main effects of the various parameters on heat transfer. Moreover, a direct comparison also permitted to compare such geometries in terms of overall heat transfer performance, which revealed that in the investigated parameter range the baseline geometry (GTE-A) provides the worst cooling performance, while the best ones are obtained by staggering the impingement holes and reducing their diameter (GTE-C). The relevant performance gap in between GTE-A and GTE-C geometries is bound to the strongly different flow structures which are

created inside each of them: as a consequence, it is worth to perform a direct comparison between such geometries in terms of flow field, in order to identify the causes of the different cooling characteristics as well as to relate the flow structures to the corresponding heat transfer pattern. This operation was performed exploiting the numerical simulations presented in Chapter 4, whose outcomes will be presented in the following chapter.

# Chapter 6

# Numerical results

In this chapter, the outcomes of the numerical activity performed in the framework of the present study will be presented. Such analysis was performed in order to understand the flow phenomena generating the heat transfer distribution, which in this case are not provided by the experimental activity. In the first section, the employed numerical setup will be validated through a direct comparison with experimental results in terms of heat transfer distributions for both GTE-A and GTE-C geometries. Subsequently, the numerical outcomes will be exploited to perform a detailed analysis of the experimental data and to provide a reliable interpretation of the different effects, including rotational ones.

## 6.1 Numerical setup validation

In order to reliably employ the outcomes of the numerical analysis, such data need to be validated, thus assessing the suitability of the employed computational setup for the replication of the investigated phenomena. In the present case, this can be achieved by comparing the computed heat transfer distributions with the ones obtained from experiments in corresponding conditions, since heat transfer data is the main goal and the most reliable information which can be obtained from the experimental campaign.

Before actually presenting the results, it must be reported that the outcomes presented for the RANS model are obtained from a sampling operation, which was necessary due to the difficult convergence of the calculations in the present case. Such difficulty arises from the high turbulence levels and complex flow structures occurring in the present case, and already hint the higher suitability of a scale resolving approach for the present investigation.

A first quantitative comparison can be performed by taking into account area averaged $Nu_b$ values, which are reported in Table 6.1 for experiments, RANS ans SAS simulations performed on both GTE-A and GTE-C geometries in static conditions. Data of Table 6.1 show that numerical simulations overestimate average values on the target surface for both geometries. In particular, for GTE-A geometry a reasonable agreement is achieved using SAS approach (+18% with respect to experimental measurements), while RANS model provides an excessive over-prediction (+36.1%). On the other hand, a significantly better agreement is obtained in the case of GTE-C geometry: overestimation is around 16.8% for RANS results, while dropping to 2.3% considering the outcome of SAS model.

Given the aim of the present investigation, a more significant validation can be perfomed if the actual shape of the heat transfer distribution is compared, in order to show the capability of the numerical approaches of actually replicating the flow phenomena causing the obtained thermal pattern. Such comparison is performed in Figure 6.1 for GTE-A geometry, where the actual $Nu_b$ distributions are scaled with respect to the

*Table 6.1: Area averaged $Nu_b$ values for GTE-A and GTE-C geometries.*

| **Geometry** | **Case** | $Re_b$ | $\overline{\overline{Nu}}_b$ | $\overline{\overline{Nu}}_b/Re_b^{0.6}$ |
|---|---|---|---|---|
| **GTE-A** $Ro_b = 0$ | **EXP** | 8520 | 29.80 | 0.1306 |
| | **RANS** | 8580 | 40.72 | 0.1777 |
| | **SAS** | 8365 | 34.76 | 0.1540 |
| **GTE-C** $Ro_b = 0$ | **EXP** | 7991 | 32.10 | 0.1462 |
| | **RANS** | 8519 | 38.96 | 0.1708 |
| | **SAS** | 8609 | 34.18 | 0.1496 |

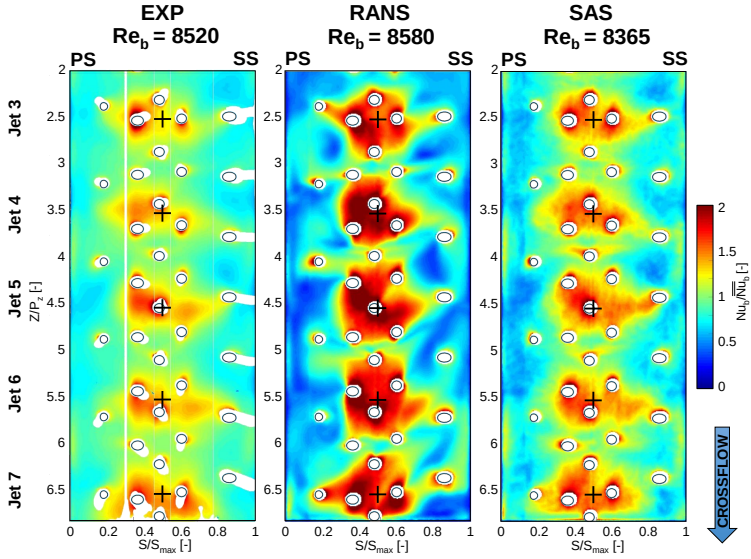


*Figure 6.1: $Nu_b/\overline{\overline{Nu}}_b$ distributions for $Ro_b = 0$ for GTE-A geometry.*

corresponding area averaged value $\overline{\overline{Nu}}_b$ in order to highlight the shape of the heat transfer pattern. It can be observed that both numerical simulations tend to overpredict the cooling effect in the central region with a lower diffusion of fresh air towards the pressure and the suction side. Such overestimation can be related to an improper description of turbulent mixing around the injection region, leading to a greater penetration of the impingement jets. In RANS results, this overprediction is particularly intense, and is combined with an approximate reproduction of heat transfer pattern shape. On the other hand, a much better qualitative agreement is achieved by SAS approach both in terms of gradients intensity and heat transfer pattern shape: this method seems capable of replicating even the slighter secondary peaks and the smaller heat transfer structures, demonstrating the reliability of the obtained results as well as the importance of actually resolving the turbulent structures in a similar case.

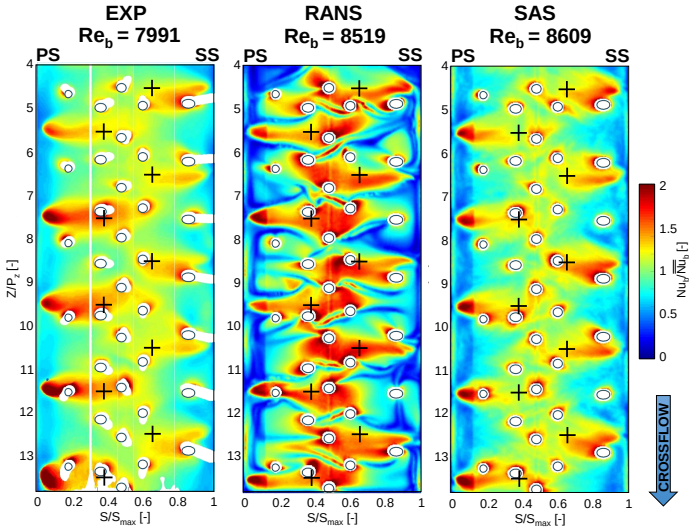


*Figure 6.2: $Nu_b/\overline{\overline{Nu}}_b$ distributions for $Ro_b = 0$ for GTE-C geometry.*

An analogous comparison is presented for GTE-C experimental and numerical outcomes in Figure 6.2. Also in this case SAS approach is capable of better predicting the experimental pattern, despite providing slightly higher heat transfer gradients. On the other hand, the disagreement is emphasized in RANS results, where the impingement jets remain more coherent due to underestimated turbulent mixing, leading to the appearance of high heat transfer peaks also in central region. Also in this case the SAS simulation is capable of replicating the smaller heat transfer structures and the local phenomena, like the higher intensity of heat transfer peaks on the pressure side. It should be clarified that the discontinuity in the heat transfer pattern along the streamwise direction on the PS in the numerical results is due to the presence of an edge in the computational domain, which is smoothed in the actual test article due to its manufacturing.
Similar considerations can be performed through a quantitative comparison, where experimental and numerical results are line-averaged to obtain $\overline{Nu}_b$ profiles along spanwise ($S$) direction, as shown in Figure 6.3. In the case of GTE-A geometry, a general agreement between experimental

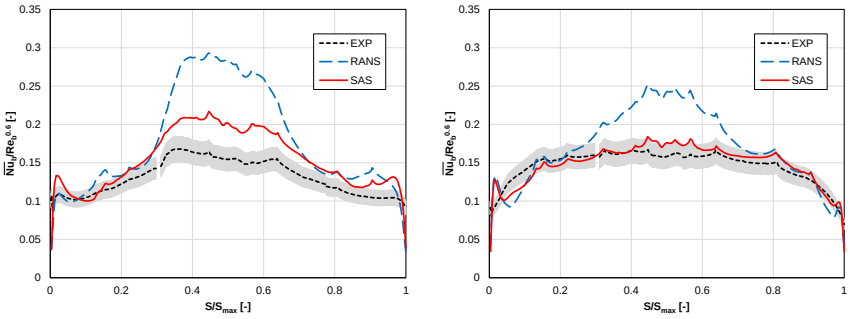


(a) (b)

*Figure 6.3: Spanwise $\overline{Nu}_b/Re_b^{0.6}$ distributions at $Re_b = 8200$ for GTE-A (a) and GTE-C (b) geometries.*

measurements and numerical results can be observed in the zones closer to the lateral surfaces, according to the experimental uncertainty (gray band). The main discrepancies arise when the regions characterized by the $Nu_b$ peaks are considered, with an evident overestimation by RANS results (+62% with respect to experimental data). On the other hand, a much better prediction is obtained with SAS approach (maximum discrepancy +25%). The same trends are highlighted by GTE-C profiles, but with a lower disagreement for both numerical approaches. Particularly, a good agreement can be noted for SAS results with a maximum relative difference of +10% in the central region. The computed differences between the two geometries can be ascribed to a different coupling between impingement jets and extraction holes, which is more pronounced for GTE-A case, as it will be shown in the following sections.

As a consequence of the previous analysis, the SAS approach can be considered a valuable model to provide a detailed explanation of the flow physics, and thus all the analyses presented in the following sections will be performed on the results of this model. The better prediction of the Nusselt number distribution compared to RANS results justifies the higher computational cost (960 CPU hours for RANS simulations and 21300 CPU hours for SAS simulations).

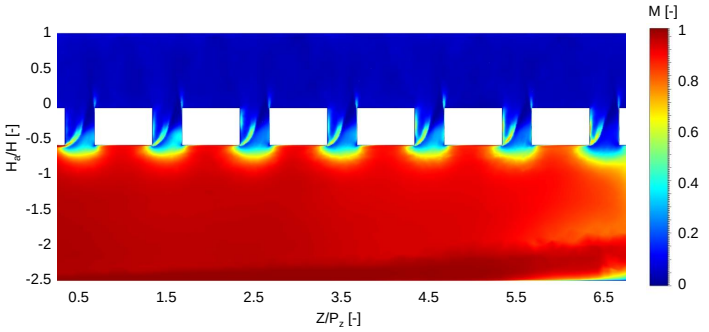


*Figure 6.4: $M$ distribution within the LE cavity for GTE-A geometry.*

With the aim to exploit the turbulence resolution capability of the SAS approach, such feature has also been validated in order to assess whether the employed computational setup is capable of properly compute the turbulent scales of interest. To do so, the $M$ criterion proposed by Pope [122] was exploited, according to which in a proper LES simulation at least 80% of the turbulent kinetic energy shall be resolved. For the present case, Figure 6.4 presents the $M$ distribution on a plane passing through GTE-A geometry jet axes, where $M$ is the ratio between the modelled and resolved turbulent kinetic energy. The vertical coordinate $H$ of Figure 6.4 presents the distance evaluated along the jet axis, which is scaled with respect to the extension $H_a$ of the impingement cavity along this direction. It can be noticed that inside the leading edge cavity ($0 < H/H_a < 1$) $M$ is lower than 0.1 in every point, which means that over 90% of the total turbulent kinetic energy is actually resolved in this region: as a consequence, the criterion is fully satisfied, and a proper turbulence resolution can be expected where jet impingement occurs. On the other hand, $M$ values close to 1 are recorded inside the feeding channel, which shows that a RANS approach is retrieved in this region as desired. The contour also reveals that a reasonable turbulence resolution is already obtained inside the impingement holes: this indicates that the scale resolution

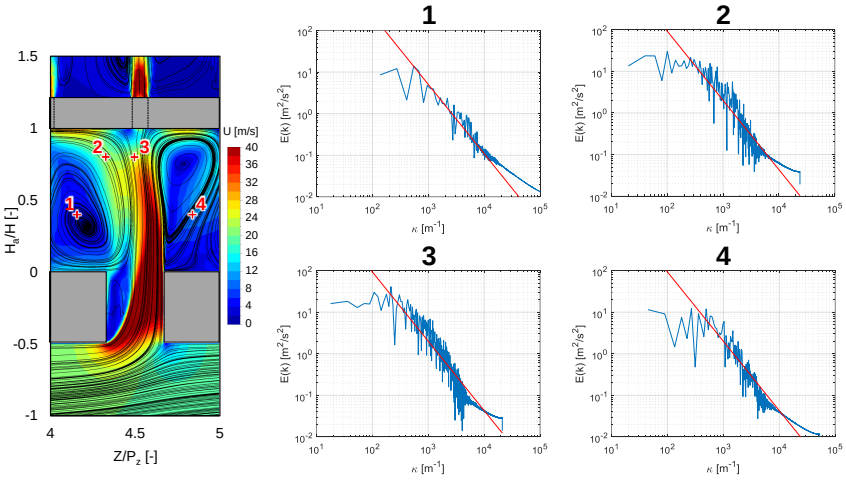


*Figure 6.5: Turbulence kinetic energy spectra in different points of the LE cavity for GTE-A jet 5 region (red lines identify -5/3 power law).*

actually begins in the jet formation region, and so that the development of turbulent structures along the whole jet is provided by the simulation. An additional check on turbulence resolution has also been performed by obtaining the turbulence kinetic energy spectrum in a number of notable points on the jets centerline plane for GTE-A jet 5 region ($4 < Z/P_z < 5$). In particular, points both inside the jet shear layer and stagnation region have been selected, as well as in the recirculation regions. Figure 6.5 presents the energy spectra obtained in all of these points as a function of the wavenumber $\kappa$. According to Kolmogorov's law, the inertial subrange of turbulence shall be identified in log-log scale by a linear region with -5/3 slope: since a similar region can be identified for every point, it can be stated that the chosen computational setup is able to properly solve the inertial subrange, and thus that a correct turbulence simulation is achieved inside the leading edge cavity.

## 6.2 GTE-A analysis

In this section, the flow phenomena occurring inside the GTE-A geometry will be presented, which will allow to relate them to the corresponding heat transfer structures an thus to provide an interpretation of the experimental results.
Figure 6.6 reports the flow field on a plane passing through the axes of impingement holes, presented in terms of time averaged velocity magnitude together with streamline trajectories. Vertical coordinate $H_a$ represents the distance along the axis of impingement hole and is scaled with respect to the jet-to-target distance $H$, while the horizontal coordinate is the same employed as vertical coordinate for Figures 6.1 and 6.2. Considering the flow within the hole, it is worth to note how the crossflow effect tends to move the flow on the downstream side of the hole, generating of a separation region due to the no fillet edge [120]. As a consequence of

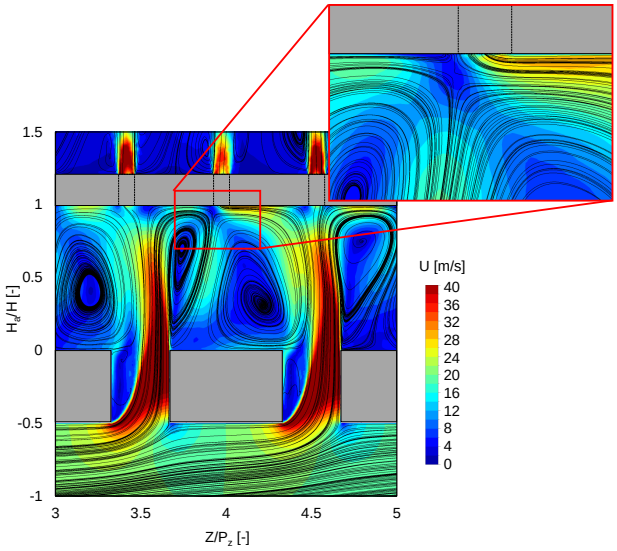


*Figure 6.6: Streamwise velocity distribution for GTE-A geometry.*

the residual momentum, the jet tends to concentrate and to increase its velocity. Even so, the impingement hole is able to drive the core jet normally to the target surface, where the velocity is reduced entering the stagnation region.

In the region between two adjacent jets, the wall jets create an intense fountain flow in the opposite direction with respect to the impinging jets [35], generating two large vortex structures. The fountain flow is inclined towards the upstream jet, forming a highly unsteady free shear zone where the two flows interact. The downward fountain then impacts on the impingement plate, forming a flow parallel to the wall, which interacts with the jets at the outlet section, representing a relevant source of instabilities. From the detailed view, it can be noted that the combination of the fountain effect together with the presence of the extraction hole drives the flow to a local impingement, which gives rise to secondary heat transfer peaks at $Z/P_z = 3, 4, 5$ and $S/S_{max} = 0.4 - 0.6$ (see heat transfer maps provided by experiments and SAS simulation in Figure 6.1).

An additional representation of the flow field is provided in Figure 6.7,

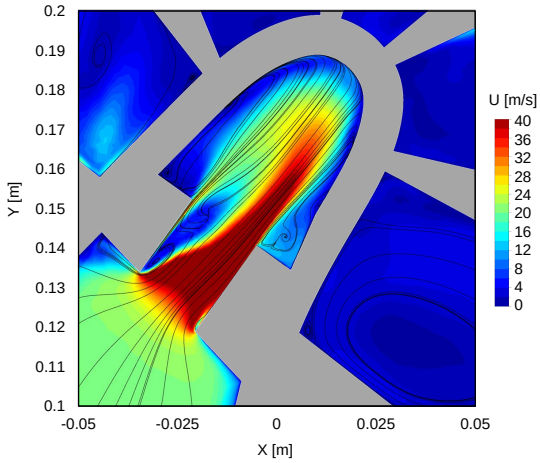


*Figure 6.7: Streamwise velocity distribution for GTE-A geometry.*

where the time averaged velocity magnitude and streamlines are presented on a tangential plane passing through the axis of jet 4 ($Z/P_z = 3.5$). A clear jet displacement towards the pressure side can be observed, which can be attributed to the jet supply condition. In fact, the impingement plate upstream side is inclined of 11° in the tangential direction with respect to the hole axis, which is also visible by the figure: as a consequence, flow turning at the inlet section is lower on the PS with respect to the SS, and the associated lower pressure losses may actually lead the coolant to flow preferably along this side. Even so, it must be noted that this phenomenon is overestimated by Figure 6.7, since the 2D velocity distribution is not able to show the actual 3D shape of the jet: in fact, the uneven inlet condition actually causes a sort of jet rotation around its axis towards the PS, as will be better visible from Figure 6.13. The streamlines highlight how the jet core is not deflected and impacts on the central region of the target surface.

The good agreement between the measured and the computed heat transfer pattern, presented in Figure 6.1, allows to identify the underlying flow phenomena generating the obtained distribution. In particular, Figure 6.1 reveals that extraction holes are able to strongly influence heat transfer pattern shape. In order to investigate this phenomenon, time averaged distributions of heat transfer related parameters are presented in Figure 6.8 for the region corresponding to jets 4 and 5. In particular, Nusselt number and total pressure were directly sampled on the jet target surface, while turbulent kinetic energy and velocity magnitude were sampled at a distance of 0.2 $mm$ from the target surface since their value at the wall is zero due to no slip condition. The choice of such distance allows to retrieve velocity parameter values in a flow region that directly influences heat transfer, since the boundary layer thickness at the jet stagnation is expected to be around 1% of the hole diameter [25]. The analysis of Nusselt number distribution (Figure 6.8a) reveals that different phenomena craft the pattern depending on the zones. In the LE central region ($0.4 < S/S_{max} < 0.6$) high heat transfer values occur where the actual jet impingement takes place, which is highlighted by the total pressure

peaks of Figure 6.8b. The smaller total pressure peak located at $Z/P_z = 4$ also identifies the location where the secondary impingement related to fountain effect and coolant extraction occurs (Figure 6.1). Higher total pressure values are also present on the side areas ($S/S_{max} < 0.1$ and $S/S_{max} > 0.9$) where thin, vertically elongated heat transfer peaks are found. These are related to the fountain flow, which impacts into the impingement plate and is then driven along the plate towards the sides of the target surface, where a secondary impingement occurs. The impingement regions are also highlighted by the velocity contour (Figure

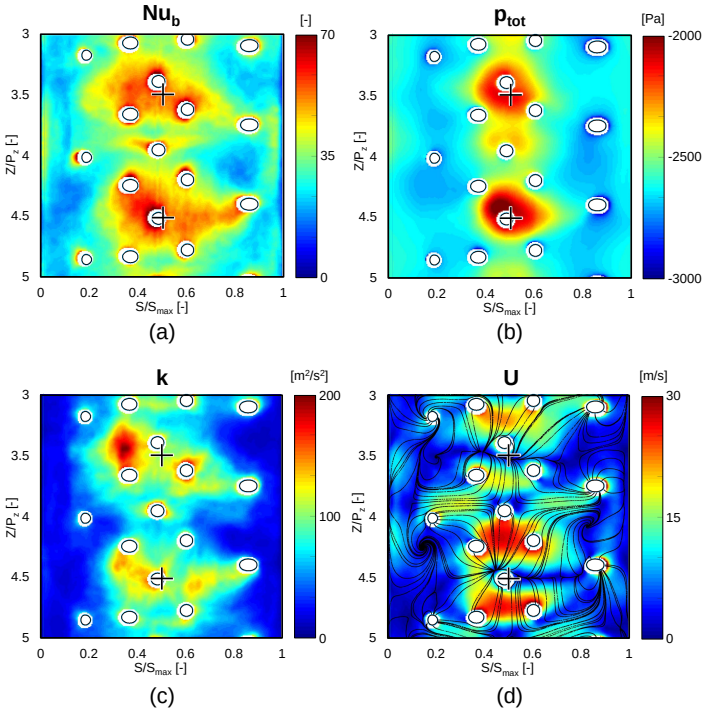


*Figure 6.8: Time averaged distributions for jet 4 and 5 region of GTE-A geometry: (a) Nusselt number, (b) total pressure (c), turbulent kinetic energy, (d) velocity magnitude.*

6.8d), where the streamlines leave the impact zones and move towards the fountains or the extraction holes. High local velocities seem not to have any relevant effect on heat transfer. Clear accelerations are present surrounding the extraction holes, which however are related to $Nu_b$ peak only in the very proximity of a limited number of holes (namely the SS holes, due to the higher mass flow rate). In particular, on the side walls ($0.1 < S/S_{max} < 0.4$ and $0.6 < S/S_{max} < 0.9$) heat transfer pattern seems not to be related neither to total pressure nor to flow velocity, while a clear correspondence can be identified with the turbulent kinetic energy profile (Figure 6.8c). This evidence reveals the main phenomenon driving heat transfer in these regions. In fact, the turbulent eddies generated in the jet shear layer are carried by the average flow field towards the extraction holes: this path brings the coherent turbulent structures along to the solid walls, thus increasing local mixing close to the surface and eventually heat transfer.

The latter consideration can be better appreciated if the actual turbulent flow structures and their path are taken into account. This can be performed thanks to Figure 6.9, where the eddies inside the impingement cavity for the jet 5 region ($4 < Z/P_z < 5$) are represented as isosurfaces of $Q = \Omega^2 - S^2$, where $\Omega$ is the absolute value of vorticity and $S$ is the absolute value of strain rate. Considering the region directly downstream the impingement hole, the typical structures associated with a turbulent jet can be observed, including vortex rings along the shear layer (one of which is highlighted in red) and a series of streamwise structures developing between consecutive vortex rings [123]. Following the evolution of the vortex highlighted in red, it is possible to observe how the initially almost undisturbed shape ($t = 0\ s$) gets progressively distorted and disrupted as the vortex travels along the jet. In particular, the left leg is clearly attracted by the suction side film cooling hole which causes the vortex to unroll towards this side of the geometry ($t = 0.0008\ s$). This motion drives the vortex core close to the heat transfer surface, transferring high momentum flow in this region and thus increasing heat transfer on jet 5 suction side area (see Figure 6.8a at $4 < Z/P_z < 5$ and $0.5 < S/S_{max} < 0.8$). As

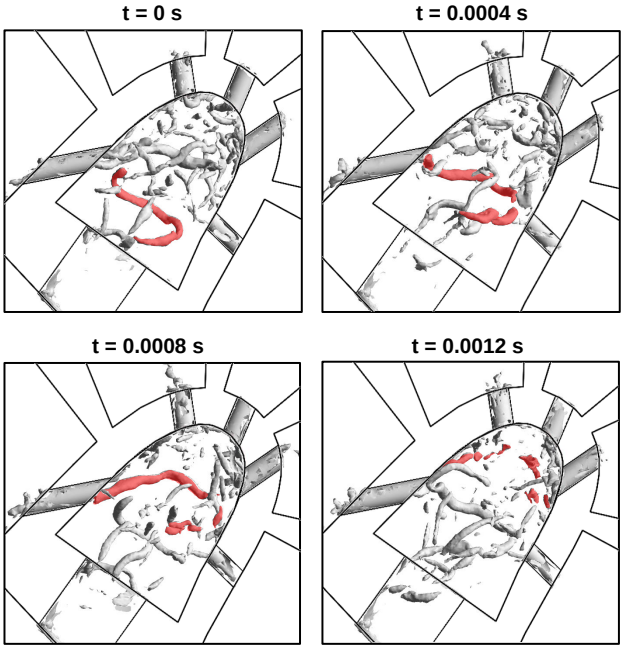


*Figure 6.9: Isosurfaces of $Q = 2.5 \cdot 10^7 s^{-2}$ for jet 5 region at different time steps.*

the vortex ring approaches the target surface it breaks down into smaller structures ($t = 0.0012\ s$) which then get driven towards the extraction holes, increasing heat transfer in their surroundings.

An additional visualization of the phenomena driving heat transfer is also provided by Figure 6.10, where the representation provided in Figure 6.9 is combined with the visualization of high heat transfer regions. It can be noticed that the high heat transfer regions are often associated both in location and shape with coherent eddies located close to the surface. Moreover, if the highlighted area is considered for the different time steps, it is possible to observe how the local heat transfer peaks, which are formed where the big shear layer eddies impinge onto the surface, break down together with the eddies themselves. The smaller peaks which get

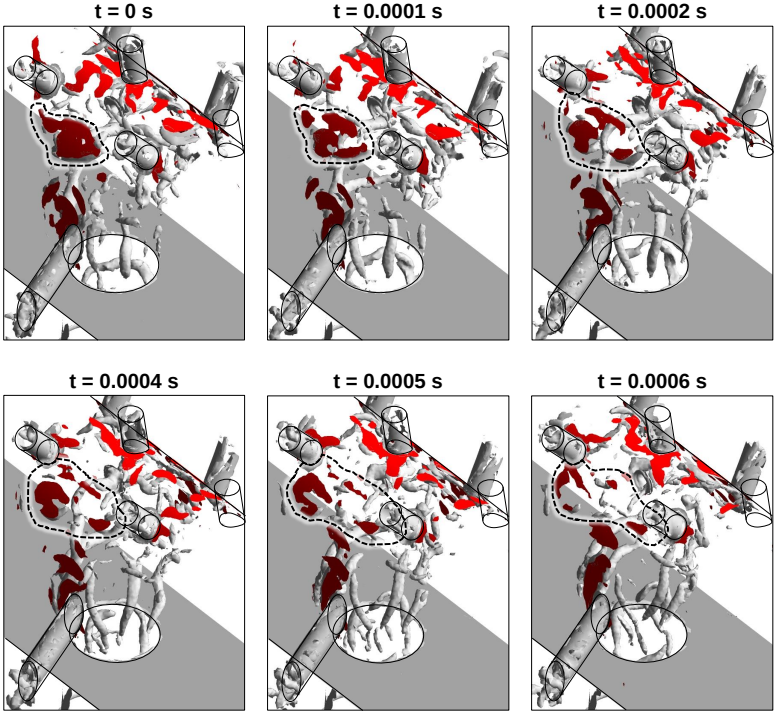


*Figure 6.10: Isosurfaces of $Q = 2.5 \cdot 10^7 s^{-2}$ for jet 5 region at different time steps (gray) and surface regions with h>300 $W/m^2K$ (red).*

formed in this way then move towards the closer extraction holes, together with the eddies they are related to.

### 6.2.1 Effect of rotation

In order to highlight the rotational effects on heat transfer, $\overline{Nu}_b/Re_b^{0.6}$ distributions in static and rotating conditions are reported in Figure 6.11, obtained from experiments and simulations. As already shown in Section 5.1.3, the experimental distributions reveal that rotation seems to reduce the jet lateral spreading: both size and magnitude of high heat transfer

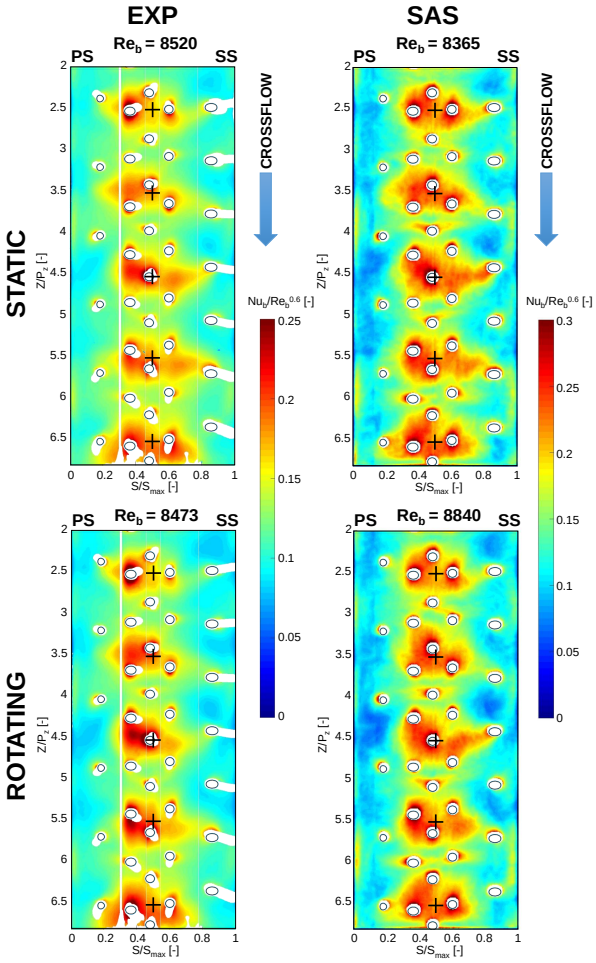


*Figure 6.11: Time averaged $Nu_b/Re_b^{0.6}$ distributions obtained for GTE-A geometry in static and rotating conditions.*

regions decrease on the side walls ($S/S_{max} < 0.3$ and $S/S_{max} > 0.7$), while in the central region the entity of the peaks increases. These phenomena appear to be replicated by the scale adaptive simulation,

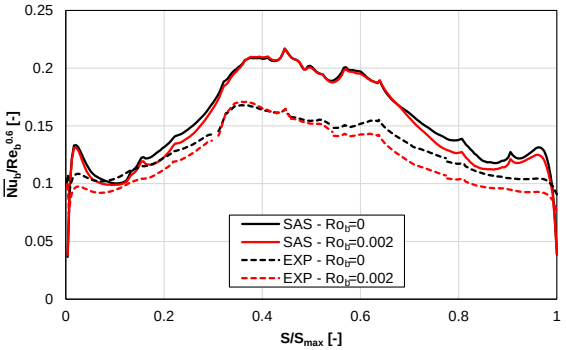


*Figure 6.12: Spanwise $\overline{Nu}_b/Re_b^{0.6}$ distributions obtained for GTE-A geometry in static and rotating conditions.*

which provides a shape for the heat transfer peaks more circular and concentrated towards the jet stagnation point in rotating conditions. Even so, the simulation seems to slightly underestimate the magnitude of rotational effects. Similar considerations can be drawn from the spanwise trends reported in Figure 6.12, obtained by averaging the distributions of Figure 6.11 along the $Z$ direction. Coherent outcomes are provided by the experimental and numerical investigations: in quantitative terms, little effects occur in the LE central region, while on the side walls rotation leads to a clear decrease in heat transfer, whose magnitude is however slightly underestimated by the simulation (10% difference from experiments and 6% from simulations).

Experimental results suggest that this phenomenon can be attributed to the interaction between the crossflow residual radial momentum and the Coriolis force, which is directed in the inward radial direction. Numerical outcomes actually confirm this supposition, as shown by Figure 6.13 where velocity profiles normal to the jet axis (scaled with respect to average jet velocity $U_{IMP}$) are reported for jet 4 at different distances from the orifice. In such distributions, horizontal coordinate $s$ represents the lateral distance from PS along the impingement plate, scaled with respect to the plate width $s_{max}$. In static conditions, the jet expands in the lateral

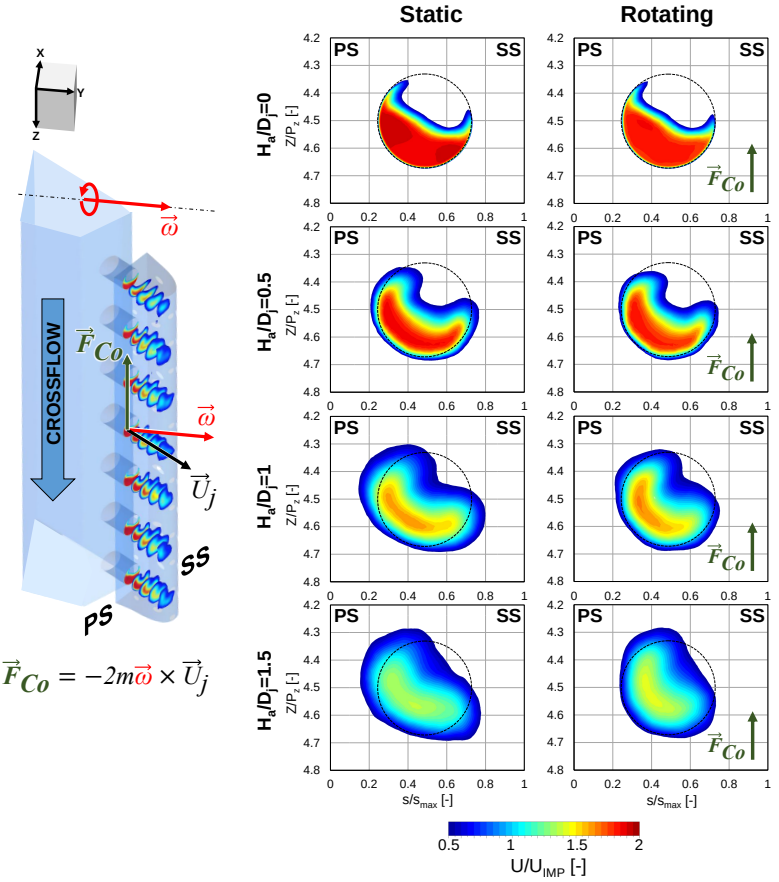


*Figure 6.13: Velocity distributions for jet 4 on planes normal to the jet axis for different $H/D_j$ values.*

direction as $H_a/D_j$ increases, which is due to the upstream crossflow concentrating the flow along the hole downstream side and thus providing a laterally elongated apparent passage section. On the other hand, in rotating conditions the jet core, where the highest velocities and thus the highest $\vec{F}_{Co}$ magnitudes occur, gets attracted towards the inner radii (i.e.

lower $Z/P_z$ values), driving the flow in the same direction and providing a less flattened and rounder shape of the jet profile (particularly evident for $H_a/D_j$ equal to 1 and 1.5). The lower jet lateral expansion leads to a lower interaction between the shear layer turbulent structures and the side walls, causing heat transfer to decrease in such regions.

## 6.3 GTE-C analysis

Regarding the GTE-C geometry, XY velocity distributions are reported in Figure 6.14 for jets 10 and 11 ($Z/P_z$ equal to 9.5 and 10.5), and reveal that in this case a strongly different flow field is present with respect to GTE-A (presented in Figure 6.7). In particular, for GTE-C geometry the impingement jets tend to move along the LE with a high velocity next to the surface, leading to the heat transfer peaks in the lateral regions of the heat transfer pattern, as shown before in Figure 6.2. As in GTE-A geometry, the jets are shifted towards the PS due to the feeding condition, causing a lower $H/D_j$ apparent distance for PS holes compared to the one of SS holes. This leads to higher flow velocities along the pressure side, which may actually justify higher values of $Nu_b$ recorded in this region. Moreover, the flow that is not intercepted by the extraction holes reaches

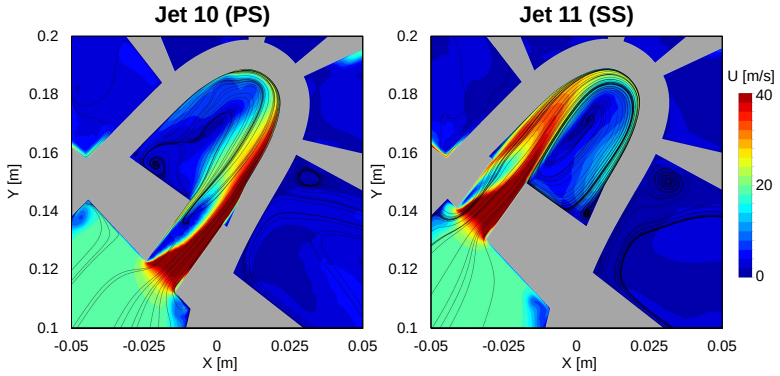


*Figure 6.14: Spanwise velocity distributions for GTE-C geometry.*

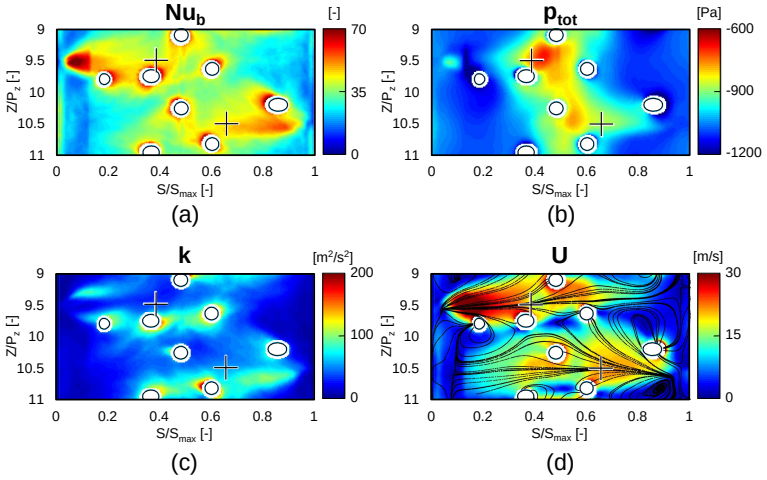


*Figure 6.15: Time averaged distributions for jet 10 and 11 region of GTE-C geometry: (a) Nusselt number, (b) total pressure (c), turbulent kinetic energy, (d) velocity magnitude.*

the opposite side of the LE surface: this motion generates a swirling effect which gives a positive contribution to the heat transfer. In fact, this phenomenon allows to maintain high velocities next to the surface and at the same time to drive colder flow towards the wall, as a result of the centrifugal force that is higher on the more dense flow [14].

As already performed for GTE-A geometry, the availability of detailed numerical data provides a deeper interpretation of the heat transfer pattern. This analysis is illustrated in Figure 6.15, which presents the values of heat transfer related parameters for the region corresponding to jets 10 and 11. Apart from the radial extension of the investigated area, the parameters definition and the sampling locations are the same as Figure 6.8. In this case, a clear correlation between $Nu_b$ and total pressure distributions (Figures 6.15a and 6.15b) is not present: jets impinge partly on the side surfaces (which is identified by the high $p_{tot}$ values for $S/S_{max} < 0.3$ and $S/S_{max} > 0.7$), but the actual stagnation

still occurs in the central part of the LE close to the ideal stagnation points (cross symbols), where high heat transfer values but no peaks are present. Considering the turbulent kinetic energy distribution (Figure 6.15c), as observed for the GTE-A case local heat transfer peaks immediately surrounding the extraction holes correspond to similar patterns for the $k$ distribution: as a consequence, a relevant turbulent contribution to heat transfer is present in the central region, given the high number of extraction holes. A partial correspondence is also present on the SS ($S/S_{max} > 0.7$), where the horizontal $k$ peak corresponds to an analogous heat transfer structure, even if a slight vertical misalignment is present between the two peaks. On the other hand, little correlation between $Nu_b$ and $k$ maps can be identified on PS ($S/S_{max} < 0.3$): two horizontally elongated peaks surround a low turbulence region, which identifies the zone where the jet potential core actually interacts with the surface (and where the heat transfer peak occurs). This difference of SS behaviour with respect to PS may be attributed to the higher apparent $H/D_j$ value, which leaves more room for the turbulent structures to develop and to interact with the surface. Finally, if near-wall velocity is considered (Figure 6.15d) a clear correspondence can be identified between the distributions of such parameter and $Nu_b$, especially on the side walls: heat transfer peaks occur where the highest velocities are present, and the shape of the high heat transfer regions is also similar.

This analysis revealed that for GTE-C geometry heat transfer is mainly driven by high flow velocities on the side walls and by extraction-driven turbulence in the central region: as a consequence, unlike GTE-A geometry, a weaker coupling between impingement (i.e. jet-wall interaction) and extraction phenomena seems to be present. This consideration may also explain the periodic heat transfer pattern provided by GTE-C, given the lower influence of extraction holes on impingement.

# Conclusions

The aim of this work is to study the heat transfer characteristics of an impingement cooling system for a gas turbine blade leading edge. The interest in such investigation is justified by the complexity of the cooling geometries, which are based upon the combination of different techniques whose mutual interaction can strongly affect the heat transfer performance. Moreover, inherent forces arising in rotating conditions (namely Coriolis and buoyancy forces) are able to alter flow field at different levels of the system, further increasing the complexity of the aforementioned interactions. To stress these effects, in this study a full cold bridge type cooling system was investigated, including the radial supply channel, the impingement plate, the leading edge inner cavity and a set of extraction holes including both showerhead and film cooling systems. The geometry is designed to replicate most of the features of a real device, which is fundamental since the interactions between the different systems may be strongly different with respect to the idealized cases usually found in the open literature. In order to perform a complete analysis, most of the effects which may actually influence heat transfer were investigated, including coolant mass flow rate, coolant supply and extraction conditions and, above all, rotation. Moreover, different hole diameters and arrangements were analysed by comparing three impingement geometries (named GTE-A, GTE-B and GTE-C), which share the same overall passage area and thus allow to isolate the effect of different coolant distributions inside the leading edge cavity.

The main part of the investigation was carried out through an experimental

analysis, which was performed on a dedicated rotating test rig. To allow heat transfer measurement for such a complex geometry, transient technique using TLC was selected. The implementation developed for this work allows to create a quasi ideal cold temperature step by using a low power mesh heater to preheat the model and a fast actuation bypass valve at the rig outlet to raise the mass flow rate at the beginning of the test. In this way, it is possible to replicate the correct sign of buoyancy forces while using simple devices and taking advantage of the high spatial resolution and results quality of the transient technique. Specific design solutions were developed for the test article and other components of the rig in order to support this technique, which also allows to control the buoyancy parameter by regulating air and model temperatures.

The experimental activity was supported by numerical investigations, which provided a detailed and complete comprehension of the phenomena generating the heat transfer distribution. The comparison of steady RANS and unsteady scale resolving SAS models revealed that solving at least a part of the turbulent spectrum is essential in order to obtain a proper reconstruction of the phenomena. According to such conclusion, SAS approach was employed to simulate a limited number of relevant test conditions, namely a single test point for GTE-A (in static and rotating conditions) and for GTE-C (in static only conditions) geometries.

The results obtained from this activity provided the full heat transfer distribution on the leading edge inner side, and the detailed resolution of the data allows to clearly identify the features of the main phenomena as well as to highlight even second order effects. In particular, it was shown that for a single row of inline holes (GTE-A geometry) a single heat transfer peak is obtained for each jet, whose shape is however strongly influenced by the presence and location of extraction holes. Simulations revealed that this pattern is generated by the combination of actual jet stagnation in the center of the surface and of high turbulent mixing on the sides, bound to the jet shear layer structures being driven towards the film cooling holes by the average flow motion. A strongly different pattern is obtained by staggering the holes (GTE-B geometry), with heat transfer

peaks strongly oriented towards the sides according to the jet location and an even higher influence of extraction holes. On the other hand, using smaller impingement holes (GTE-C geometry) allows to have higher flow velocities close to the side walls, which actually dominate heat transfer in this case and provide a lower interaction between impingement and extraction flow fields. This also justifies the better agreement between experimental and numerical results obtained in this case with respect to GTE-A geometry.

As regards the effect of coolant mass flow rate, it was found that a higher jet Reynolds number $Re_j$ causes heat transfer to increase, with area averaged Nusselt number $Nu$ being proportional to $Re_j^{0.6}$ for every geometry. On the other hand, a negligible influence on the heat transfer pattern shape was recorded.

A more complex effect was found for the jet upstream condition. A higher crossflow, i.e. moving from the tip to the hub of the blade, causes the flow to separate on the upstream side of the impingement hole and to concentrate along the downstream side: this provides a laterally elongated shape for the jet, which actually enhances its lateral spreading towards the side walls. This effect has a small influence on the overall cooling performance of the inline geometry (GTE-A), while the increased wall-jet interaction leads to a significant heat transfer increase for the staggered ones (up to 18% for GTE-C).

Extraction condition effect is also strongly dependent upon the geometry. For geometries where the heat transfer pattern is strongly influenced by the turbulent mixing (i.e. GTE-A and GTE-B) an intense effect on the pattern shape is recorded, while average heat transfer is less influenced. On the other hand, for GTE-C geometry increasing the extraction through film cooling holes seems to improve the interaction between the turbulent structures and the side walls, with little effect on heat transfer pattern shape but positive influence on average Nusselt value.

The obtained results show that rotation can significantly alter flow field and heat transfer pattern, acting both on the supply channel flow and on the impingement jets. In particular, since the leading edge and thus

the jets are oriented towards the pressure side, in rotating conditions a Coriolis force is generated on the jets themselves. Such force is oriented towards the inward radial direction, and thus tends to counterbalance the effect of the outward crossflow: as a result, in rotating conditions the jet lateral spreading decreases, and so does the jet-wall interaction. This causes heat transfer to decrease on the side walls, with a slightly negative effect on the cooling performance. Since this effect is given by the interaction between rotation and crossflow effects, its entity decreases as crossflow increases. A Coriolis force is also generated in the feeding channel, driving the flow along the pressure side and causing uneven supply conditions for the jets to occur. While this may lead to a heat transfer decrease with inline impingement holes (GTE-A geometry) in low crossflow conditions, for staggered holes this phenomenon promotes the feeding of the pressure side holes with respect to the suction side ones: as a consequence, rotation negative effect on heat transfer is weakened on the pressure side.

Finally, the direct comparison of the impingement geometries also revealed the effect of different holes arrangements and diameters. This analysis revealed that employing staggered holes increases the positive crossflow effects and reduces the sensitivity to negative rotational influence. The first phenomenon is even more emphasized by reducing the holes diameter, which allows to reduce the distance between the jet core and the side walls. As a consequence, the best cooling performance is obtained by GTE-C geometry, which also presents slightly lower pressure losses with respect to GTE-A and GTE-B.

This brief summary of the obtained results shows how the present work allowed to investigate the majority of the effects actually conditioning heat transfer in a cold bridge type impingement system. Most of these effects, despite having been considered in the open literature, are rarely investigated together, which was demonstrated to be a fundamental requirement in order to correctly evaluate their interactions. Moreover, most of the phenomena recorded in the present realistic system are different from the ones usually reported in literature for simple and

idealized geometries, despite the underlying physics is the same in all cases. Finally, this work showed that the combination of numerical and experimental analysis is a viable way to retrieve complete and reliable information even for complex geometries like the investigated ones.

# Appendix A

# Uncertainty evaluation for transient technique

In order to obtain uncertainty values associated with $h$ calculation using Equation 3.13, the following operations are carried out starting from the equation itself. By defining the parameters $\theta$ and $\beta$ as:

$$\theta = \frac{T_w(t) - T_i}{T_{ref} - T_i} \tag{A.1}$$

$$\beta = h\sqrt{\frac{t}{\rho_s c_s \lambda_s}} \tag{A.2}$$

Equation 2.7 can be recast as:

$$\theta = 1 - e^{\beta^2} \cdot erfc(\beta) \tag{A.3}$$

According to Kline and McClintock approach the absolute error on a quantity $G$ expressed as a function $f$ of some primary quantities $g_1, g_2, ..., g_n$ is given by (Equation 4.6):

$$\Delta G = \sqrt{\left(\Delta g_1 \frac{\partial f}{\partial g_1}\right)^2 + \left(\Delta g_2 \frac{\partial f}{\partial g_2}\right)^2 + ... + \left(\Delta g_n \frac{\partial f}{\partial g_n}\right)^2} \tag{A.4}$$

An even simpler expression can be derived if $G$ can be expressed as:

$$G = g_1^{a_1} \cdot g_2^{a_2} \cdot ... \cdot g_n^{a_n} \tag{A.5}$$

In this case, the relative uncertainty of $G$ can be obtained from the expression:

$$\frac{\Delta G}{G} = \sqrt{\left(a_1 \frac{\Delta g_1}{g_1}\right)^2 + \left(a_2 \frac{\Delta g_2}{g_2}\right)^2 + ... + \left(a_n \frac{\Delta g_n}{g_n}\right)^2} \tag{A.6}$$

Recasting Equation A.2 as a function of $h$ and applying Equation A.6 to retrieve the relative uncertainty of $h$ leads to:

$$\frac{\Delta h}{h} = \sqrt{\left(\frac{\Delta \beta}{\beta}\right)^2 + \frac{1}{4}\left(\frac{\Delta(\rho_s c_s \lambda_s)}{(\rho_s c_s \lambda_s)}\right)^2 + \frac{1}{4}\left(\frac{\Delta t}{t}\right)^2} \tag{A.7}$$

The absolute uncertainty of $\beta$ can be related to the uncertainty of $\theta$ by exploiting Equation A.3. First, the partial derivative of $\theta$ with respect to $\beta$ can be retrieved:

$$\begin{aligned}
\frac{\partial \theta}{\partial \beta} &= \frac{\partial\left(1 - e^{\beta^2} \cdot erfc(\beta)\right)}{\partial \beta} = \\
&= -e^{\beta^2} \cdot 2\beta \cdot erfc(\beta) - e^{\beta^2} \cdot \left(-\frac{2}{\sqrt{\pi}} e^{-\beta^2}\right) = \\
&= \frac{2}{\sqrt{\pi}} - e^{\beta^2} \cdot 2\beta \cdot erfc(\beta) = \\
&= \frac{2}{\sqrt{\pi}} + 2\beta(\theta - 1)
\end{aligned}$$

Where the last simplification is obtained thanks to Equation A.3, from which it follows that $-e^{\beta^2} \cdot erfc(\beta) = \theta - 1$. The application of Equation A.4 to Equation A.3 provides:

$$\Delta\theta = \sqrt{\left(\Delta\beta \frac{\partial\theta}{\partial\beta}\right)^2} = \Delta\beta \frac{\partial\theta}{\partial\beta} = \Delta\beta\left(\frac{2}{\sqrt{\pi}} + 2\beta(\theta - 1)\right) \tag{A.8}$$

From which an expression for the term $\Delta\beta$ appearing in Equation A.7 can be obtained:

$$\Delta\beta = \frac{\Delta\theta}{\frac{2}{\sqrt{\pi}} + 2\beta(\theta - 1)} \tag{A.9}$$

To retrieve the value of $\Delta\beta$, the absolute uncertainty on $\theta$ needs to be evaluated. This value can be retrieved by applying again Equation A.4 to Equation A.1 which defines $\theta$:

$$\Delta\theta = \sqrt{\left(\Delta T_w \frac{\partial\theta}{\partial T_w}\right)^2 + \left(\Delta T_i \frac{\partial\theta}{\partial T_i}\right)^2 + \left(\Delta T_{ref} \frac{\partial\theta}{\partial T_{ref}}\right)^2} \tag{A.10}$$

Developing the partial derivatives the equation reduces to:

$$\Delta\theta = \frac{1}{(T_{ref} - T_i)^2} \sqrt{\Delta T_w^2 (T_{ref} - T_i)^2 + \Delta T_i^2 (T_w - T_{ref})^2 + \Delta T_{ref}^2 (T_i - T_w)^2} \tag{A.11}$$

Which provides the uncertainty associated to $\theta$ given the temperature values and their uncertainties, which are known in the present case. By combining Equations A.7, A.9 and A.11 it is thus possible to evaluate the relative uncertainty of $h$ in a transient test from the quantities employed for the calculation (temperatures, time, material properties) and their uncertainties. A similar procedure is applied if the non ideal temperature step is taken into account by decomposing it into a series of smaller ideal steps.

# List of Figures

# List of Tables

# Bibliography


[1] Grand view research, gas turbine market size, share and trends analysis report by capacity ($< 200mw$, $> 200mw$), by technology (open cycle, combined cycle), by application (power generation, industrial, aviation), and segment forecasts, 2018-2025, Jul 2018.

[2] Hitchin, P. "Complementing renewable energy with gas turbines." *GE Power Transform*, 2017.

[3] ICAO. Long-term traffic forecasts - passenger and cargo, Jul 2016.

[4] ACARE. Strategic research & innovation agenda, 2017.

[5] EASA, EUROCONTROL EEA. European aviation environmental report 2016.

[6] Giampaolo, T. *Gas turbine handbook: principles and practice.* Fairmont Press, 2002.

[7] Han, J.C., Dutta, S., and Ekkad, S. *Gas turbine heat transfer and cooling technology.* CRC Press, 2012.

[8] Ballal, D.R. and Zelina, J. "Progress in aeroengine technology (1939–2003)." *Journal of aircraft*, 41(1):43–50, 2004.

[9] Giuntini, S. *Transient modelling of whole gas turbine engine: an aero-thermo-mechanical approach.* PhD thesis, Università degli Studi di Firenze, 2018.

[10] Pievaroli, M. *Matrix Cooling Systems for Gas Turbine Nozzles and Blades: Experimental Investigations and Design Correlations.* PhD thesis, Università degli Studi di Firenze, 2014.

[11] Winchler, L. *Design tools and innovative concepts for gas turbine cooling applications.* PhD thesis, Università degli Studi di Firenze, 2016.

[12] Simpson, T.W. "Am needs mes." *ASME Mechanical Engineering*, 137:30–35, 2015.

[13] Amano, R.S. "Advances in gas turbine blade cooling technology." *Advanced Computational Methods and Experiments in Heat Transfer X, B. Sunden, and CA Brebbia, eds., WIT Press, Southampton, UK*, 2008.

[14] Bunker, R.S. *Innovative gas turbine cooling techniques.* WIT Press, Southampton, UK, 2008.

[15] Han, J.C. "Recent studies in turbine blade cooling." *International Journal of Rotating Machinery*, 10(6):443–457, 2004.

[16] Gupta, S., Chaube, A., and Verma, P. "Review on heat transfer augmentation techniques: Application in gas turbine blade internal cooling." *Journal of Engineering Science & Technology Review*, 5 (1), 2012.

[17] Wagner, J.H., Johnson, B.V., and Kopper, F.C. "Heat transfer in rotating serpentine passages with smooth walls." *Journal of Turbomachinery*, 113(3):321–330, 1991.

[18] Han, J.C., Zhang, Y.M., and Kalkuehler, K. "Uneven wall temperature effect on local heat transfer in a rotating two-pass square channel with smooth walls." *Journal of heat transfer*, 115(4):912–920, 1993.

[19] Fu, W.L., Wright, L.M., and Han, J.C. "Rotational buoyancy effects on heat transfer in five different aspect-ratio rectangular channels with smooth walls and 45degree ribbed walls." *Journal of Heat Transfer*, 128(11):1130–1141, 2006.

[20] Von Wolfersdorf, J. and Weigand, B. Turbine blade internal cooling - selected experimental approaches, May 2010.

[21] Bons, J.P. and Kerrebrock, J.L. Complementary velocity and heat transfer measurements in a rotating cooling passage with smooth walls. In *ASME 1998 international gas turbine and aeroengine congress and exhibition*, pages V004T09A080–V004T09A080. American Society of Mechanical Engineers, 1998.

[22] Zuckerman, N. and Lior, N. "Jet impingement heat transfer: physics, correlations, and numerical modeling." *Advances in heat transfer*, 39:565–631, 2006.

[23] Spring, S. and Weigand, B. Jet impingement heat transfer, May 2010.

[24] Viskanta, R. "Heat transfer to impinging isothermal gas and flame jets." *Experimental thermal and fluid science*, 6(2):111–134, 1993.

[25] Martin, H. Heat and mass transfer between impinging gas jets and solid surfaces. In *Advances in heat transfer*, volume 13, pages 1–60. Elsevier, 1977.

[26] Surace, M. *Investigation of impingement systems for gas turbine combustor cooling.* PhD thesis, Università degli Studi di Firenze, 2018.

[27] Abramovich, G.N., Girshovich, T.A., Krasheninnikov, S.I., Sekundov, A.N., and Smirnova, I.P. "The theory of turbulent jets." *Moscow Izdatel Nauka*, 1984.

[28] Deng, H., Gu, Z., Zhu, J., and Tao, Z. "Experiments on impingement heat transfer with film extraction flow on the leading edge of rotating blades." *International Journal of Heat and Mass Transfer*, 55(21-22): 5425–5435, 2012.

[29] Jung, E.Y., Park, C.U., Lee, D.H., Park, J.S., Park, S., and Cho, H.H. Effect of rotation on heat transfer of a concave surface with array impingement jet. In *ASME Turbo Expo 2013: Turbine Technical Conference and Exposition*, pages V03AT12A042–V03AT12A042. American Society of Mechanical Engineers, 2013.

[30] Kercher, D.M. and Tabakoff, W. "Heat transfer by a square array of round air jets impinging perpendicular to a flat surface including the effect of spent air." *Journal of Engineering for power*, 92(1): 73–82, 1970.

[31] Florschuetz, L.W., Truman, C.R., and Metzger, D.E. Streamwise flow and heat transfer distributions for jet array impingement with crossflow. In *ASME 1981 International Gas Turbine Conference and Products Show*, pages V003T09A005–V003T09A005. American Society of Mechanical Engineers, 1981.

[32] Florschuetz, L.W., Metzger, D.E., and Su, C.C. Heat transfer characteristics for jet array impingement with initial crossflow. In *ASME 1983 International Gas Turbine Conference and Exhibit*, pages V004T09A001–V004T09A001. American Society of Mechanical Engineers, 1983.

[33] Behbahani, A.I. and Goldstein, R.J. "Local heat transfer to staggered arrays of impinging circular air jets." *Journal of engineering for power*, 105(2):354–360, 1983.

[34] Jordan, C.N. *Experimental investigation of leading edge jet impingement with varying jet geometries and inlet supply conditions for turbine cooling applications.* PhD thesis, 2012.

[35] Cho, H.H. and Rhee, D.H. Local heat/mass transfer measurement on the effusion plate in impingment/effusion cooling system. In *ASME Turbo Expo 2000: Power for Land, Sea, and Air*, pages V003T01A058–V003T01A058. American Society of Mechanical Engineers, 2000.

[36] Andreini, A., Cocchi, L., Facchini, B., Mazzei, L., and Picchi, A. "Experimental and numerical investigation on the role of holes arrangement on the heat transfer in impingement/effusion cooling schemes." *International Journal of Heat and Mass Transfer*, 127: 645–659, 2018.

[37] Brevet, P., Dorignac, E., and Vullierme, J.J. "Mach number effect on jet impingement heat transfer." *Annals of the New York Academy of Sciences*, 934(1):409–416, 2001.

[38] Goodro, M., Ligrani, P., Fox, M., and Moon, H.K. "Mach number, reynolds number, jet spacing variations: Full array of impinging jets." *Journal of Thermophysics and Heat Transfer*, 24(1):133–144, 2010.

[39] Goodro, M., Park, J., Ligrani, P., Fox, M., and Moon, H.K. "Effect of temperature ratio on jet array impingement heat transfer." *Journal of Heat Transfer*, 131(1):012201, 2009.

[40] Cocchi, L., Facchini, B., Giuntini, S., Winchler, L., Tarchi, L., Innocenti, L., Andrei, L., and Bonini, A. Experimental investigation on impingement array cooling systems through ir thermography. In *ASME Turbo Expo 2016: Turbomachinery Technical Conference and Exposition*, pages V05BT16A014–V05BT16A014. American Society of Mechanical Engineers, 2016.

[41] Metzger, D.E., Baltzer, R.T., and Jenkins, C.W. "Impingement cooling performance in gas turbine airfoils including effects of leading edge sharpness." *Journal of Engineering for Power*, 94(3):219–225, 1972.

[42] Gau, C. and Chung, C.M. "Surface curvature effect on slot-air-jet impingement cooling flow and heat transfer process." *Journal of Heat Transfer*, 113(4):858–864, 1991.

[43] Chupp, R.E., Helms, H.E., and McFadden, P.W. "Evaluation of internal heat-transfer coefficients for impingement-cooled turbine airfoils." *Journal of Aircraft*, 6(3):203–208, 1969.

[44] Hrycak, P. "Heat transfer from a row of impinging jets to concave cylindrical surfaces." *International Journal of Heat and Mass Transfer*, 24(3):407–419, 1981.

[45] Bunker, R.S. and Metzger, D.E. "Local heat transfer in internally cooled turbine airfoil leading edge regions: Part i—impingement cooling without film coolant extraction." *Journal of Turbomachinery*, 112(3):451–458, 1990.

[46] Facchini, B., Maiuolo, F., Tarchi, L., and Ohlendorf, N. Experimental investigation on the heat transfer in a turbine airfoil leading edge region: Effects of the wedge angle and jet impingement geometries. In *European Turbomachinery Conference (ETC2013), Lappeenranta Finland, Apr*, pages 15–19, 2013.

[47] Jordan, C.N., Wright, L.M., and Crites, D.C. Effect of impingement supply condition on leading edge heat transfer with rounded impinging jets. In *ASME 2012 Heat Transfer Summer Conference collocated with the ASME 2012 Fluids Engineering Division Summer Meeting and the ASME 2012 10th International Conference on Nanochannels, Microchannels, and Minichannels*, pages 841–850. American Society of Mechanical Engineers, 2012.

[48] Taslim, M.E., Setayeshgar, L., and Spring, S.D. An experimental evaluation of advanced leading edge impingement cooling concepts. In *ASME Turbo Expo 2000: Power for Land, Sea, and Air*, pages V003T01A030–V003T01A030. American Society of Mechanical Engineers, 2000.

[49] Metzger, D.E. and Bunker, R.S. "Local heat transfer in internally cooled turbine airfoil leading edge regions: Part ii—impingement cooling with film coolant extraction." *Journal of Turbomachinery*, 112(3):459–466, 1990.

[50] Taslim, M.E., Pan, Y., and Spring, S.D. An experimental study of impingement on roughened airfoil leading-edge walls with film holes. In *ASME Turbo Expo 2001: Power for Land, Sea, and Air*, pages V003T01A035–V003T01A035. American Society of Mechanical Engineers, 2001.

[51] Facchini, B., Maiuolo, F., Tarchi, L., and Ohlendorf, N. Experimental investigation on the heat transfer of a leading edge cooling system: effects of jet-to-jet spacing and showerhead extraction. In *ASME Turbo Expo 2013: Turbine Technical Conference and Exposition*, pages V03AT12A026–V03AT12A026. American Society of Mechanical Engineers, 2013.

[52] Taslim, M.E. and Setayeshgar, L. Experimental leading-edge impingement cooling through racetrack crossover holes. In *ASME Turbo Expo 2001: Power for Land, Sea, and Air*, pages V003T01A036–V003T01A036. American Society of Mechanical Engineers, 2001.

[53] Taslim, M.E., Bakhtari, K., and Liu, H. Experimental and numerical investigation of impingement on a rib-roughened leading-edge wall. In *ASME Turbo Expo 2003, collocated with the 2003 International Joint Power Generation Conference*, pages 31–41. American Society of Mechanical Engineers, 2003.

[54] Taslim, M.E. and Khanicheh, A. "Experimental and numerical study of impingement on an airfoil leading edge with and without showerhead and gill film holes." *Journal of turbomachinery*, 128(2): 310–320, 2006.

[55] Jordan, C.N., Elston, C.A., Wright, L.M., and Crites, D.C. Leading edge impingement with racetrack shaped jets and varying inlet supply conditions. In *ASME Turbo Expo 2013: Turbine Technical Conference and Exposition*, pages V03AT12A020–V03AT12A020. American Society of Mechanical Engineers, 2013.

[56] Harmon, W.V., Wright, L.M., Crites, D.C., Morris, M.C., and Riahi, A. Combined effects of jet plate thickness and fillet radius on leading edge jet impingement with round and racetrack shaped jets. In *ASME Turbo Expo 2015: Turbine Technical Conference and Exposition*, pages V05AT11A032–V05AT11A032. American Society of Mechanical Engineers, 2015.

[57] Andrei, L., Carcasci, C., Da Soghe, R., Facchini, B., Maiuolo, F., Tarchi, L., and Zecchi, S. "Heat transfer measurements in a leading edge geometry with racetrack holes and film cooling extraction." *Journal of Turbomachinery*, 135(3):031020, 2013.

[58] Massini, D., Burberi, E., Carcasci, C., Cocchi, L., Facchini, B., Armellini, A., Casarsa, L., and Furlani, L. "Effect of rotation on a gas turbine blade internal cooling system: experimental investigation." *Journal of Engineering for Gas Turbines and Power*, 139(10):101902, 2017.

[59] Taslim, M.E., Pan, Y., and Bakhtari, K. Experimental racetrack shaped jet impingement on a roughened leading-edge wall with film holes. In *ASME Turbo Expo 2002: Power for Land, Sea, and Air*, pages 897–906. American Society of Mechanical Engineers, 2002.

[60] Harmon, W.V., Elston, C.A., and Wright, L.M. Experimental investigation of leading edge impingement under high rotation numbers with racetrack shaped jets. In *ASME Turbo Expo 2014: Turbine Technical Conference and Exposition*, pages V05AT12A031–V05AT12A031. American Society of Mechanical Engineers, 2014.

[61] Epstein, A.H., Kerrebrock, J.L., Koo, J.J., and Preiser, U.Z. Rotational effects on impingement cooling. In *Heat Transfer and Fluid Flow in Rotating Machinery*, pages 86–102, 1987.

[62] Mattern, C. and Hennecke, D.K. The influence of rotation on impingement cooling. In *ASME 1996 International Gas Turbine and Aeroengine Congress and Exhibition*, pages V004T09A003–V004T09A003. American Society of Mechanical Engineers, 1996.

[63] Iacovides, H., Kounadis, D., Launder, B. E, Li, J., and Xu, Z. Experimental study of the flow and thermal development of a row of cooling jets impinging on a rotating concave surface. In *ASME Turbo Expo 2004: Power for Land, Sea, and Air*, pages 213–222. American Society of Mechanical Engineers, 2004.

[64] Hong, S.K., Lee, D.H., and Cho, H.H. "Heat/mass transfer measurement on concave surface in rotating jet impingement." *Journal of mechanical science and technology*, 22(10):1952–1958, 2008.

[65] Hong, S.K., Lee, D.H., and Cho, H.H. "Effect of jet direction on heat/mass transfer of rotating impingement jet." *Applied Thermal Engineering*, 29(14-15):2914–2920, 2009.

[66] Hong, S.K., Lee, D.H., and Cho, H.H. "Heat/mass transfer in rotating impingement/effusion cooling with rib turbulators." *International Journal of Heat and Mass Transfer*, 52(13-14):3109–3117, 2009.

[67] Elston, C.A. and Wright, L.M. Leading edge jet impingement under high rotation numbers. In *ASME 2012 International Mechanical Engineering Congress and Exposition*, pages 1963–1976. American Society of Mechanical Engineers, 2012.

[68] Polat, S., Mujumdar, A.S., and Douglas, W.J.M. "Heat transfer distribution under a turbulent impinging jet–a numerical study." *Drying Technology*, 3(1):15–38, 1985.

[69] Ashforth-Frost, S. and Jambunathan, K. "Numerical prediction of semi-confined jet impingement and comparison with experimental data." *International Journal for Numerical methods in fluids*, 23 (3):295–306, 1996.

[70] Coussirat, M., Van Beeck, J., Mestres, M., Egusquiza, E., Buchlin, J.M., and Valero, C. "Computational fluid dynamics modeling of impinging gas-jet systems: Ii. application to an industrial cooling system device." *Journal of fluids engineering*, 127(4):704–713, 2005.

[71] Morris, G.K., Garimella, S.V., and Fitzgerald, J.A. "Flow-field prediction in submerged and confined jet impingement using the reynolds stress model." *Journal of Electronic Packaging*, 121(4): 255–262, 1999.

[72] Souris, N., Liakos, H., and Founti, M. "Impinging jet cooling on concave surfaces." *AIChE Journal*, 50(8):1672–1683, 2004.

[73] Kumar, B.V.N.R. and Prasad, B.V.S.S.S. "Computational flow and heat transfer of a row of circular jets impinging on a concave surface." *Heat and Mass Transfer*, 44(6):667–678, 2008.

[74] Taslim, ME and Bethka, D. "Experimental and numerical impingement heat transfer in an airfoil leading-edge cooling channel with cross-flow." *Journal of Turbomachinery*, 131(1):011021, 2009.

[75] Bianchini, C., Burberi, E., Cocchi, L., Facchini, B., Massini, D., and Pievaroli, M. Numerical analysis and preliminary experimental heat transfer measurements on a novel rotating leading edge model. In *12th International Symposium on Experimental Computational Aerothermodynamics of Internal Flows, Genova, Italy, July*, pages 13–16, 2015.

[76] Andreini, A., Burberi, E., Cocchi, L., Facchini, B., Massini, D., and Pievaroli, M. "Heat transfer investigation on an internal cooling system of a gas turbine leading edge model." *Energy Procedia*, 82: 222–229, 2015.

[77] Burberi, E., Massini, D., Cocchi, L., Mazzei, L., Andreini, A., and Facchini, B. "Effect of rotation on a gas turbine blade internal cooling system: numerical investigation." *Journal of Turbomachinery*, 139(3):031005, 2017.

[78] Pagnacco, F., Furlani, L., Armellini, A., Casarsa, L., and Davis, A. Rotating heat transfer measurements on a multi-pass internal cooling channel: I—rig development. In *ASME Turbo Expo 2016: Turbomachinery Technical Conference and Exposition*, pages V05BT16A005–V05BT16A005. American Society of Mechanical Engineers, 2016.

[79] Pagnacco, F., Furlani, L., Armellini, A., Casarsa, L., and Davis, A. Rotating heat transfer measurements on a multi-pass internal cooling channel: Ii—experimental tests. In *ASME Turbo Expo 2016: Turbomachinery Technical Conference and Exposition*, pages V05BT16A004–V05BT16A004. American Society of Mechanical Engineers, 2016.

[80] Thurman, D. and Poinsatte, P. Experimental heat transfer and bulk air temperature measurements for a multipass internal cooling model with ribs and bleed. In *ASME Turbo Expo 2000: Power for Land, Sea, and Air*, pages V003T01A041–V003T01A041. American Society of Mechanical Engineers, 2000.

[81] Wang, Z., Gillespie, D., and Ireland, P. Advances in heat transfer measurements using liquid crystals. In *Proceedings of the Turbulent Heat Transfer Conference, 10-15*, 1996.

[82] Facchini, B., Innocenti, L., and Tarchi, L. Pedestal and endwall contribution in heat transfer in thin wedge shaped trailing edge. In *ASME Turbo Expo 2004: Power for Land, Sea, and Air*, pages 101–111. American Society of Mechanical Engineers, 2004.

[83] Schultz, D.L. and Jones, T.V. Heat-transfer measurements in short-duration hypersonic facilities. Technical report, ADVISORY

GROUP FOR AEROSPACE RESEARCH AND DEVELOPMENT PARIS (FRANCE), 1973.

[84] Metzger, D.E. and Larson, D.E. "Use of melting point surface coatings for local convection heat transfer measurements in rectangular channel flows with 90-deg turns." *Journal of Heat Transfer*, 108(1): 48–54, 1986.

[85] Vogel, G. and Weigand, B. A new evaluation method for transient liquid crystal experiments. Technical report, 2001.

[86] Buttsworth, D.R. and Jones, T.V. "Radial conduction effects in transient heat transfer experiments." *The Aeronautical Journal*, 101 (1005):209–212, 1997.

[87] Wagner, G., Kotulla, M., Ott, P., Weigand, B., and Von Wolfersdorf, J. The transient liquid crystal technique: influence of surface curvature and finite wall thickness. In *ASME Turbo Expo 2004: Power for Land, Sea, and Air*, pages 521–531. American Society of Mechanical Engineers, 2004.

[88] Maiuolo, F. *Experimental Analysis of Gas Turbine Airfoil Leading Edge Cooling Systems.* PhD thesis, Università degli Studi di Firenze, 2012.

[89] Li, Y., Xu, G., Deng, H., and Tian, S. "Buoyancy effect on heat transfer in rotating smooth square u-duct at high rotation number." *Propulsion and Power Research*, 3(3):107–120, 2014.

[90] Abdullah, N., Talib, A.R.A., Jaafar, A.A., Salleh, M.A.M., and Chong, W.T. "The basics and issues of thermochromic liquid crystal calibrations." *Experimental Thermal and Fluid Science*, 34 (8):1089–1121, 2010.

[91] Hallcrest, LCR. Handbook of thermochromic liquid crystal technology, 2017.

[92] Sage, I. "Thermochromic liquid crystals." *Liquid crystals*, 38(11-12): 1551–1561, 2011.

[93] Kakade, V.U., Lock, G.D., Wilson, M., Owen, J.M., and Mayhew, J.E. "Accurate heat transfer measurements using thermochromic liquid crystal. part 1: Calibration and characteristics of crystals." *International Journal of Heat and Fluid Flow*, 30(5): 939–949, 2009.

[94] Talib, A.R.A., Neely, A.J., Ireland, P.T., and Mullender, A.J. "A novel liquid crystal image processing technique using multiple gas temperature steps to determine heat transfer coefficient distribution and adiabatic wall temperature." *Journal of Turbomachinery*, 126 (4):587–596, 2004.

[95] Ireland, P.T. and Jones, T.V. "The response time of a surface thermometer employing encapsulated thermochromic liquid crystals." *Journal of Physics E: Scientific Instruments*, 20(10):1195, 1987.

[96] Wang, Z., Ireland, P.T., Jones, T.V., and Davenport, R. A colour image processing system for transient liquid crystal heat transfer experiments. In *ASME 1994 International Gas Turbine and Aeroengine Congress and Exposition*, pages V004T09A044–V004T09A044. American Society of Mechanical Engineers, 1994.

[97] Wiberg, R. and Lior, N. "Errors in thermochromic liquid crystal thermometry." *Review of scientific instruments*, 75(9):2985–2994, 2004.

[98] Chan, T.L., Ashforth-Frost, S., and Jambunathan, K. "Calibrating for viewing angle effect during heat transfer measurements on a curved surface." *International Journal of Heat and Mass Transfer*, 44(12):2209–2223, 2001.

[99] Bakrania, S. and Anderson, A.M. A transient technique for calibrating thermochromic liquid crystals: the effects of surface preparation,

lighting and overheat. In *ASME 2002 International Mechanical Engineering Congress and Exposition*, pages 445–451. American Society of Mechanical Engineers, 2002.

[100] Anderson, M.R. and Baughn, J.W. "Hysteresis in liquid crystal thermography." *Journal of heat transfer*, 126(3):339–346, 2004.

[101] Smith, L., Karim, H., Etemad, S., Pfefferle, W.C., et al. "The gas turbine handbook." 2006.

[102] Gillespie, D.R.H., Wang, Z., and Ireland, P.T. "Heating element." *British Patent Application PCT/GB96*, 2017.

[103] Bonanni, L., Carcasci, C., Facchini, B., and Tarchi, L. Experimental survey on heat transfer in a trailing edge cooling system: effects of rotation in internal cooling ducts. In *ASME turbo expo 2012: turbine technical conference and exposition*, pages 633–644. American Society of Mechanical Engineers, 2012.

[104] ASME. "Measurement uncertainty." *In Instrument and apparatus*, vol. ANSI/ASME PTC 19.1-1985 of *Performance Test Code*, 1985.

[105] Kline, S.J. and McClintock, F.A. "Describing uncertainties in single sample experiments." *Mechanical Engineering*, 75: 3–8, 1953.

[106] Camci, C. Liquid crystal thermography, July 1995.

[107] Mangani, L. *Development and validation of an Object Oriented CFD Solver for Heat Transfer and Combustion Modeling in Turbomachinery Applications.* PhD thesis, Università degli Studi di Firenze, 2012.

[108] Menter, F.R. "Best practice: scale-resolving simulations in ansys cfd." *ANSYS Germany GmbH*, pages 1–70, 2012.

[109] Mazzei, L., Andreini, A., Facchini, B., and Turrini, F. "Impact of swirl flow on combustor liner heat transfer and cooling: a numerical investigation with hybrid reynolds-averaged navier–stokes large eddy

simulation models." *Journal of Engineering for Gas Turbines and Power*, 138(5):051504, 2016.

[110] Spalart, P.R. Comments on the feasibility of les for wings, and on a hybrid rans/les approach. In *Proceedings of first AFOSR international conference on DNS/LES*. Greyden Press, 1997.

[111] Menter, F. and Egorov, Y. A scale adaptive simulation model using two-equation models. In *43rd AIAA Aerospace Sciences Meeting and Exhibit*, page 1095, 2005.

[112] Rotta, JC. "Über eine methode zur berechnung turbulenter scherströmungen." *Aerodynamische Versuchsanstalt Rep*, 69:A14, 1968.

[113] Rotta, JC. Turbulente strömumgen. bg teubner stuttgart; 1972.

[114] Menter, F.R. and Egorov, Y. "The scale-adaptive simulation method for unsteady turbulent flow predictions. part 1: theory and model description." *Flow, Turbulence and Combustion*, 85(1):113–138, 2010.

[115] Menter, F.R. and Egorov, Y. Revisiting the turbulent scale equation. In *IUTAM Symposium on One Hundred Years of Boundary Layer Research*, pages 279–290. Springer, 2006.

[116] Davidson, L. Evaluation of the sst-sas model: channel flow, asymmetric diffuser and axi-symmetric hill. In *European Conference on Computational Dynamics, ECCOMAS CFD*. Citeseer, 2006.

[117] Celik, I.B., Cehreli, Z.N., and Yavuz, I. "Index of resolution quality for large eddy simulations." *Journal of fluids engineering*, 127(5): 949–958, 2005.

[118] Poser, R. and Von Wolfersdorf, J. Transient liquid crystal thermography in complex internal cooling systems, May 2010.

[119] Sundberg, J. Heat transfer correlations for gas turbine cooling, 2006.

[120] Gritsch, M., Schulz, A., and Wittig, S. Effect of crossflows on the discharge coefficient of film cooling holes with varying angles of inclination and orientation. In *ASME Turbo Expo 2001: Power for Land, Sea, and Air*, pages V003T01A020–V003T01A020. American Society of Mechanical Engineers, 2001.

[121] Thole, K.A., Gritsch, M., Schulz, A., and Wittig, S. "Effect of a crossflow at the entrance to a film-cooling hole." *Journal of Fluids Engineering*, 119(3):533–540, 1997.

[122] Pope, S.B. "Ten questions concerning the large-eddy simulation of turbulent flows." *New journal of Physics*, 6(1):35, 2004.

[123] Liepmann, Dorian and Gharib, Morteza. "The role of streamwise vorticity in the near-field entrainment of round jets." *Journal of Fluid Mechanics*, 245:643–668, 1992.